Defence Research and Development Canada   Recherche et développement pour la défense Canada

DEFENCE **R&D** DÉFENSE

Experimental investigation of the strength of damaged pressure hulls – Phase 1

J. R. MacKay

Defence R&D Canada – Atlantic

Technical Memorandum
DRDC Atlantic TM 2006-304
February 2007

Canada

This page intentionally left blank.

Experimental investigation of the strength of damaged pressure hulls – Phase 1

J. R. MacKay

Defence R&D Canada – Atlantic

Technical Memorandum

DRDC Atlantic TM 2006-304

February 2007

Author
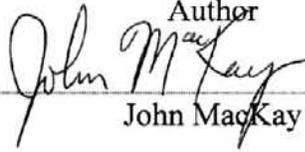
John MacKay

Approved by
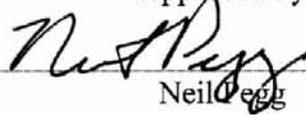
Neil Pegg

Head, Warship Performance

Approved for release by
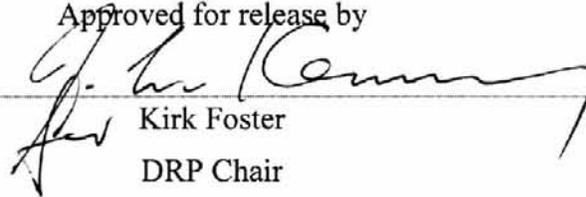
Kirk Foster

DRP Chair

Abstract

This document presents the results of Phase 1 of an experimental program to determine the collapse pressures of small-scale pressure hulls (ring-stiffened cylinders) with various amounts and patterns of simulated material loss due to corrosion. Six ring-stiffened aluminium cylinders have been tested as part of Phase 1: two undamaged specimens, three specimens with simulated localized corrosion, and one specimen with reinforced hull penetrations. Material loss was found to decrease the collapse pressure of each of the corroded specimens relative to similar undamaged cylinders. This loss of strength was attributed to reduced structural stiffness in the corroded regions, and was typically associated with an early onset of material yield. In two cases, yielding occurred at the corrosion well before the ultimate collapse load, and would thus further decrease the allowable working load. The results of the entire experimental program, which will include upwards of 40 cylinders, will be used to develop guidelines for corrosion tolerance, and to validate analytical and numerical methods.

Résumé

Le présent document présente les résultats de la phase 1 d'un programme expérimental visant à déterminer les pressions d'écrasement des coques épaisses à petite échelle (cylindres renforcés à l'aide d'anneaux) avec diverses quantités et configurations de perte de matériau simulée causée par la corrosion. Six cylindres d'aluminium renforcés à l'aide d'anneaux ont été testés dans le cadre de la phase 1 : deux éprouvettes non endommagés, trois éprouvettes avec de la corrosion localisée simulée et une éprouvette avec des pénétrations de coque de type renforcé. On a découvert que la perte de matériau diminue la pression d'écrasement de chacune des éprouvettes corrodées par rapport à des cylindres non endommagés semblables. Cette perte de résistance a été attribuée à une rigidité de structure réduite dans les régions corrodées et elle était typiquement associée à un début précoce de fléchissement de matériau. Dans deux cas, le fléchissement s'est produit au niveau de la corrosion bien avant la charge d'écrasement ultime et il diminuerait ainsi davantage la charge d'utilisation permissible. Les résultats de tout le programme expérimental, qui comprendront plus de 40 cylindres, seront utilisés pour développer des lignes directrices en matière de tolérance de corrosion et pour valider les méthodes analytiques et numériques.

This page intentionally left blank.

Executive summary

Background

Pressure hulls are structures that are designed to withstand hydrostatic pressure, so that stability or collapse is the major structural design consideration. As they typically operate in seawater, pressure hulls are susceptible to corrosion damage. Corrosion that results in a loss of structural material can significantly reduce the collapse strength, and thus operational capabilities, of pressure hulls. DRDC Atlantic and the Netherlands Ministry of Defence have begun a collaborative project to study the structural behaviour of corroded pressure hulls.

Principal Results

This document presents the results of Phase 1 of an experimental program to determine the collapse pressures of model pressure hulls (ring-stiffened cylinders) with various amounts and patterns of simulated material loss due to corrosion. Six aluminium cylinders were pressurized to collapse at DRDC Atlantic: two undamaged specimens, three specimens with simulated localized corrosion, and one specimen with reinforced hull penetrations. Material loss was found to decrease the collapse pressure of the corroded specimens relative to similar undamaged cylinders. This was associated with reduced structural stiffness and early onset of yielding in the corroded regions.

Significance of Results

Corrosion, even in a very discrete and localized form, was found to significantly reduce the ultimate strength of the ring-stiffened cylinders tested to collapse. This was true for simulated corrosion of either the stiffener flanges or the shell. In two cases with local shell corrosion, yielding and then local buckling occurred at the corrosion well before the ultimate collapse load of the specimen. In a real pressure hull, this would further decrease the allowable working load and operational capability, as material yielding during normal operations is not acceptable.

Future Work

These tests are part of a larger experimental program that will be used to develop guidelines for in-service pressure hull corrosion tolerances. The overall program will include the testing of approximately 40 cylinders, with different structural configurations and patterns of corrosion. Nonlinear finite element analyses will be undertaken for each of the specimens, which will allow the validation of the analytical method for assessing corrosion scenarios not studied experimentally.

Sommaire

Introduction

Les coques épaisses sont des structures conçues pour supporter la pression hydrostatique, de sorte que la stabilité ou l'écrasement est la considération principale de conception de structure. Comme elles sont habituellement utilisées dans l'eau salée, les coques épaisses sont susceptibles d'être endommagées par la corrosion. La corrosion qui résulte en une perte de matériau de structure peut diminuer de façon importante la résistance à l'écrasement, et, donc, les capacités opérationnelles, des coques épaisses. RDDC Atlantique et le ministère de la Défense des Pays-Bas ont entrepris un projet de collaboration visant à étudier le comportement de la structure de coques épaisses corrodées.

Résultats

Le présent document présente les résultats de la phase 1 d'un programme expérimental visant à déterminer les pressions d'écrasement des coques épaisses modèles (cylindres renforcés à l'aide d'anneaux) avec diverses quantités et configurations de perte de matériau simulée causée par la corrosion. Six cylindres d'aluminium ont été pressurisés pour s'effondrer à RDDC Atlantique : deux éprouvettes non endommagés, trois éprouvettes avec de la corrosion localisée simulée et une éprouvette avec des pénétrations de coque de type renforcé. On a découvert que la perte de matériau diminue la pression d'écrasement des éprouvettes corrodées par rapport à des cylindres non endommagés semblables. Cela était associé à une rigidité de structure réduite et à un début précoce de fléchissement dans les régions corrodées.

Portée

On a découvert que la corrosion, même d'une forme très discrète et localisée, diminue de façon importante la résistance à l'écrasement ultime des cylindres renforcés à l'aide d'anneaux. Cela était vrai pour la corrosion simulée de la coquille ou des rebords raidisseurs. Dans deux cas avec la corrosion de coque locale, du fléchissement, puis un devers local, se sont produits au niveau de la corrosion bien avant la charge d'écrasement ultime de l'éprouvette. Dans une vraie coque épaisse, cela diminuerait davantage la charge d'utilisation permissible et la capacité opérationnelle, car les fléchissements de matériau pendant les opérations normales ne sont pas acceptables.

Recherches futures

Ces essais font partie d'un programme expérimental plus vaste qui sera utilisé pour développer des lignes directrices pour les tolérances à la corrosion des coques épaisses en service. Le programme global comprendra l'essai d'environ 40 cylindres, avec des configurations de structure et de corrosion différentes. Des analyses par éléments finis de type non linéaire seront entreprises pour chacune des éprouvettes, ce qui per-

mettra la validation de la méthode analytique permettant d'évaluer les scénarios de corrosion non étudiés expérimentalement.

MacKay, J. R. (2007). Experimental investigation of the strength of damaged pressure hulls – Phase 1. DRDC Atlantic TM 2006-304. DRDC Atlantic.

Table of contents

List of figures

List of tables

Acknowledgements

1. Introduction

Pressure hulls, the main load-bearing structures in naval submarines, commercial submersibles, and many offshore structures, operate in a salt-water environment, and are therefore susceptible to corrosion damage. Ingress of seawater can occur at pressure hull penetrations and at the acoustic tiles in submarines due to de-bonding, resulting in corrosion of the pressure hull material.

The effects of corrosion on the pressure hull can be divided into two categories: 1) degradation of the material properties in the corroded region, and 2) loss of structural mass due to removal of the corroded material. The latter effect is the focus of the current study.

Corrective measures, which can be taken if the corrosion is significant, include:

- complete replacement of the corroded region, which is costly and typically a last resort;

- grinding of the corroded region followed by clad welding to replace the removed material, which can have potentially serious material considerations, such as parent-weld material mismatch; and

- grinding of the corroded region, with no subsequent replacement of the removed material.

The latter method of repair results in a locally thin region of the structure. Numerical investigations undertaken by DRDC Atlantic [1] have indicated that the role of this local thinning due to corrosion, as an initiator of structural failure in pressure hulls, needs to be understood more thoroughly. Therefore, a series of cylinder collapse tests has been initiated to determine the effects of corrosion damage (thinning) on the structural performance of pressure hulls.

The experimental program aims to increase the understanding of pressure hull thinning due to corrosion, with regards to structural integrity. The end goal of the overall study is twofold: 1) to establish tolerances for corrosion damage whereby the requirement for corrective action or operational restrictions will be eliminated, and 2) to validate appropriate analysis techniques for assessing the operational implications of corrosion when the damage exceeds the established tolerance.

The Phase 1 work reported here aims to study the effect of corrosion damage, in combination with different types of collapse, on pressure hull strength. This includes the effects of local shell thinning due to corrosion on interframe collapse and local stiffener corrosion on overall collapse. The effect of reinforced penetrations on overall collapse strength is also considered.

The experimental research program, which is a collaboration of DRDC Atlantic and the Ministry of Defence of the Netherlands, falls under a long-standing Memorandum of Understanding (MOU) between these countries [2] that allows for cooperation in the fields of naval ship and submarine design. The project involves the fabrication, destructive testing, and analysis of approximately 40 small-scale aluminium ring-stiffened cylinders with various levels and patterns of simulated corrosion scarring. The small-scale cylinders were designed to behave in a similar fashion to a pressure hull, and the structural effect of corrosion was simulated by machining out material in various patterns.

Phase 1 of this experimental program has been completed. Five newly fabricated cylinders, stiffened with external T-section rings, have been pressurized to collapse at the DRDC Atlantic pressure testing facility in the spring and summer of 2005. A rectangular section ring-stiffened aluminium cylinder with penetrations, which is a specimen remaining from a previous Canada-Netherlands research project [3], was also tested during this period. This document describes the test specimens (Section 2), experimental apparatus and procedures (Section 3), and experimental results (Section 4) for the initial phase of testing, and also presents suggestions for future work (Section 6).

2. Test Specimens

Phase 1 of the experimental program included five cylinders with external T-section ring-stiffeners, as well as a single rectangular section ring-stiffened cylinder with penetrations. The T-section stiffened cylinders, manufactured by Gizom b.v. in Veendam, the Netherlands, in 2004, were lumped into two groups: short cylinders, which were designed to fail locally in the pressure hull shell, and long cylinders, which were designed to fail globally. The cylinder with penetrations was fabricated at the Naval Shipyard in Den Helder, the Netherlands, in 1989-90. All cylinders were machined from extruded aluminium alloy tubing.

The cylinder specimens tested were as follows.

- one short cylinder without corrosion (L300-No2)

- two short cylinders with simulated corrosion on the shell (L300-No3 and L300-No4)

- one long cylinder without corrosion (L510-No1)

- one long cylinder with 'dog-bone' corrosion on the central flanges (L510-No2)

- one rectangular section ring-stiffened cylinder with reinforced penetrations

The T-section stiffened specimens were measured for geometric imperfections by Duiker Mechanical b.v. in Zoetermeer, the Netherlands, in December 2004. Schielab b.v. of Rotterdam, the Netherlands, performed coupon tests for determining material properties in November 2005. Selected specimens were instrumented with strain gauges by the Netherlands Organisation for Applied Scientific Research (TNO) in Delft, the Netherlands, in 2005. Corrosion was simulated by removing material from either the shell or stiffeners, and thus the effect of reduced shell thickness or stiffener area was studied in isolation from any possible material degradation due to corrosion.

The following sections describe the general specimen construction (Section 2.1), the nominal design geometry (Section 2.2), geometric imperfections (Section 2.3), shell thickness (Section 2.4), material properties (Section 2.5) and instrumentation (Section 2.6).

2.1 Specimen Construction

Pressure hulls are primarily designed to withstand hydrostatic pressure through compressive stressing of the structure. Circular geometries are best suited to efficiently resist pressure hull design loads. Consequently, pressure hulls are typically composed of a continuous series of ring-stiffened cylinders and cones. These are separated into compartments by load-bearing watertight bulkheads, and terminated on either end by hemi- or toro-spherical domes (Figure 1).

Structural design calculations are carried out for each pressure hull compartment in isolation [4]. A compartment is treated as an idealized ring-stiffened cylinder, even if it has tapered conical sections. This study is solely concerned with the basic structural element of a pressure hull: the ring-stiffened cylinder.
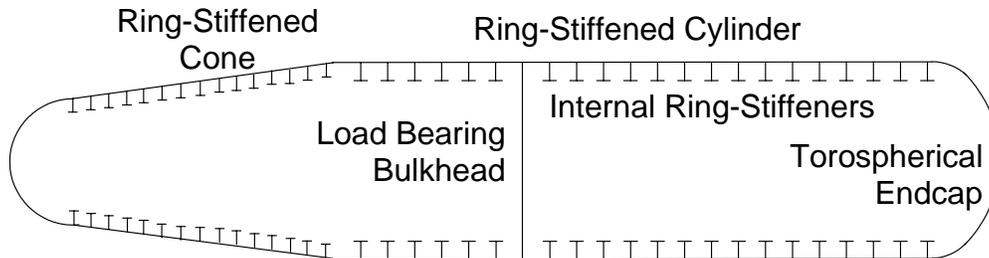
Figure 1. *Typical pressure hull structure*

Pressure hulls are usually constructed of high-strength steel, which is cold bent into a circular shape to form the pressure hull. The ring-stiffeners are typically either cold-bent T-sections, or built up T-sections composed of cold bent flanges and cut webs. Significant residual stresses are formed during the cold bending process, especially in the flanges of cold bent T-sections, which can have a detrimental impact on the strength of the pressure hull [5]. Welding of the structure induces additional residual stresses that could have a negative impact on structural strength [6].

Typical pressure hulls fail via an elasto-plastic collapse mechanism, whereby the strength of the structure is limited by material plasticity, nonlinear geometric behaviour, and instability associated with elastic buckling. This type of failure is characterized by: 1) an increasingly nonlinear strain-pressure relationship as the applied load is increased, 2) the onset of yield in critical areas of the structure, 3) ultimate collapse at a load only slightly greater than the load causing first yield, and 4) a collapse shape associated with a critical elastic buckling mode. Of course, these criteria do not hold true for all pressure hulls, but may serve as a general guideline.

The ring-stiffened cylinders examined in this project were constructed by machining extruded aluminium tubing. The choice of material and fabrication method results in three significant differences between real pressure hulls and the experimental specimens. Real pressure hulls: 1) are constructed of material that is approximately twice as strong and twice as stiff as the experimental specimen material, 2) have strength-reducing residual stresses, while the specimens are almost free of residual stress, and 3) have significant strength-reducing geometric imperfections due to the fabrication process, while the specimens were manufactured to a small tolerance resulting in very small imperfections. These differences are acceptable, however, on the following bases.

Despite the differences in yield stress (e.g. 550 vs. 250 MPa) and elastic modulus (e.g. 207 vs. 70 GPa), high-strength steel and aluminium exhibit qualitatively similar behaviour. Both materials have: 1) a large linear-elastic region, 2) a relatively abrupt yield point followed by strain-hardening behaviour, and 3) a similar yield strength to elastic modulus ratio (approximately 0.27 and 0.42% for high-strength steel and alu-

minium, respectively). Consequently they behave similarly in elasto-plastic collapse failures, as is the case for pressure hulls.

It is important to study the effect of material loss due to corrosion in isolation from secondary strength-reducing factors that may vary over a range of specimens and thereby skew the results in an unpredictable manner. However, future specimens will have both residual stresses and larger geometric imperfections, both in isolation and in combination with corrosion damage. This will allow the isolated and combined effect of the strength-reducing factors to be determined, and will better represent a real pressure hull.

2.2 Nominal Geometry

2.2.1 Short Cylinders

The short cylinders were designed to fail locally in an interframe collapse mechanism. The design geometry for the undamaged (i.e. no simulated corrosion) short cylinders is shown in Figure 2. The short cylinders were stiffened with external T-section rings, which were proportioned to be relatively stiff compared with the shell in order to force failure to occur in the shell through a combination of material yielding and lobar buckling (Figure 3). The stiffener spacing was specified to be greatest in the central bay to encourage failure at this location. The cylinders had thick end rings that tapered gradually to the mean shell thickness to prevent end-bay failure.
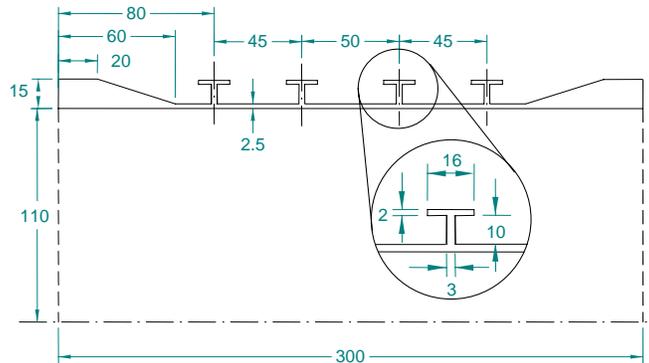
Figure 2. *Basic geometry of short cylinder (mm)*

Elastic interframe (lobar) buckling (*n*=6)   Elasto-plastic interframe collapse
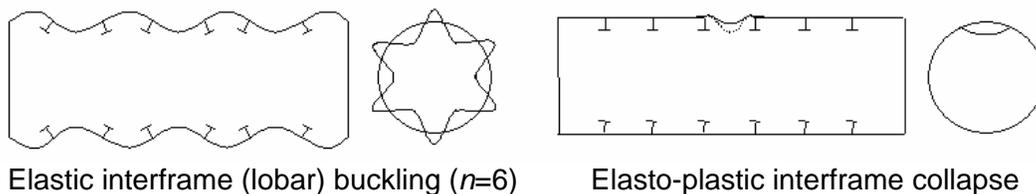
Figure 3. *Interframe collapse modes*

Two undamaged short cylinders were manufactured: the first (L300-No1) was instrumented with strain gauges, but was not tested during Phase 1; the second (L300-No2) had no instrumentation and served to validate the collapse pressure of the first cylinder.

Corrosion damage in real pressure hull structures, if not repaired by clad welding or replacement, is treated by grinding away the corroded material. The net effect of corrosion damage followed by grinding was simulated by machining away the shell material to produce a square area of uniformly reduced thickness on the outside of the middle bay of a short cylinder (Figure 4 and Figure 5). The region of corrosion was nominally 34 x 34 mm in area and 0.625 mm in depth (approximately 25% of the shell thickness). Two short cylinders with simulated corrosion were manufactured: the first (L300-No3) was instrumented with strain gauges, and the second (L300-No4) was not instrumented.
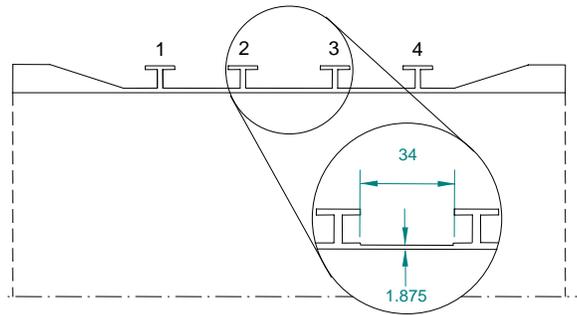
Figure 4. *Short cylinder with uniform shell corrosion at mid bay (with frame numbers)*
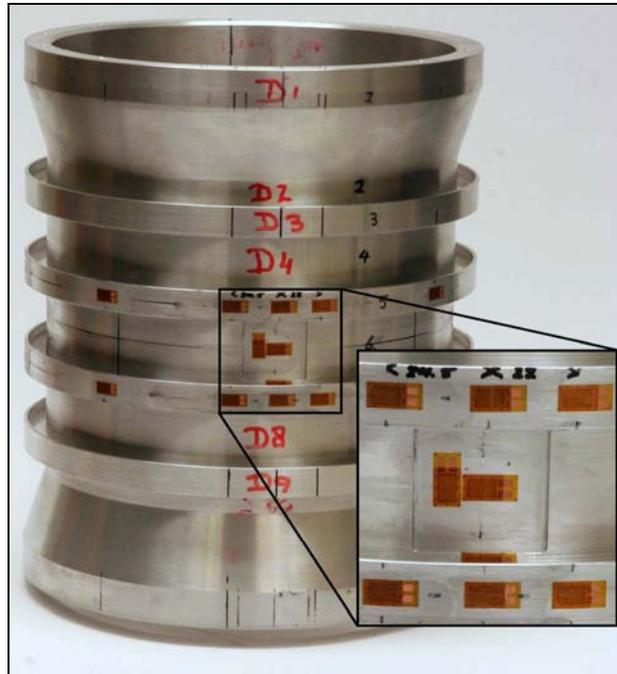
Figure 5. *Photograph of short cylinder (L300-No3) with shell corrosion at mid bay*

2.2.2 Long Cylinders

The long cylinders were designed to fail globally by an overall collapse mechanism. Overall collapse is typified by yielding of the stiffener flange, or shell plating at the toe of the stiffener, which initiates a global buckling of the combined stiffener-shell section (Figure 6).
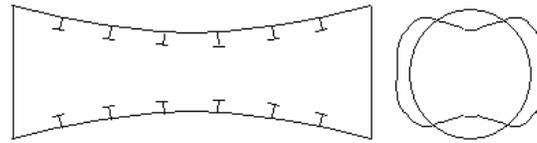
Elastic overall collapse (n=2)

Figure 6. *Overall collapse mode*

The design geometry for the undamaged long cylinders is shown in Figure 7. The long cylinders were also stiffened with external T-section rings, which were proportioned to be relatively weak compared with the shell in order to favour overall collapse. The stiffener spacing was uniform over the length of the cylinder. These cylinders also had thick end rings to prevent end-bay failure. A single undamaged long cylinder (L510-No1) was manufactured and instrumented with strain gauges (Section 2.6.2).
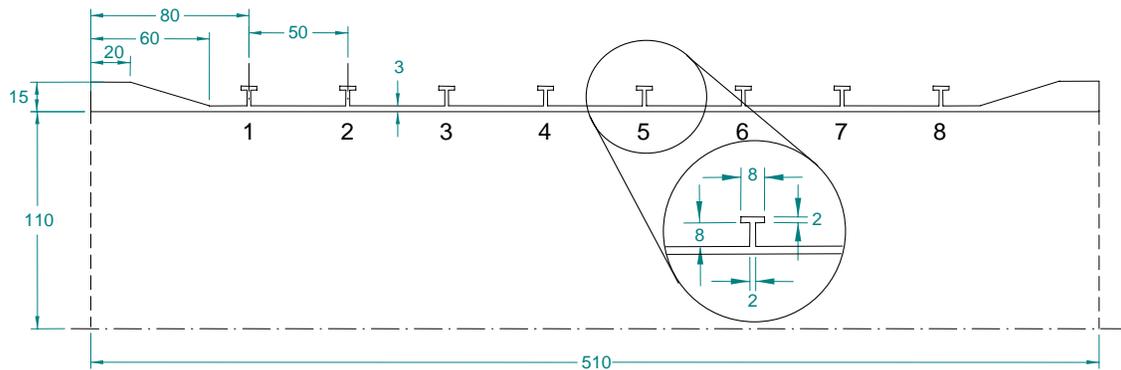
Figure 7. *Basic geometry of long cylinder (mm) with stiffener numbers*

Corrosion was simulated in two long cylinders by machining away material from the two central stiffener flanges to produce a 'dog-bone' type pattern (Figure 8 and Figure 9). The corrosion was located at a single circumferential location, and was intended to induce overall collapse by instigating an early onset of yield in the corroded region of the stiffener flange due to the reduced section area.

Two long cylinders with simulated corrosion were manufactured: the first (L510-No2) had no instrumentation, and the second (L510-No3), which was not tested during Phase 1 of the experimental program, will be instrumented and tested in Phase 2.
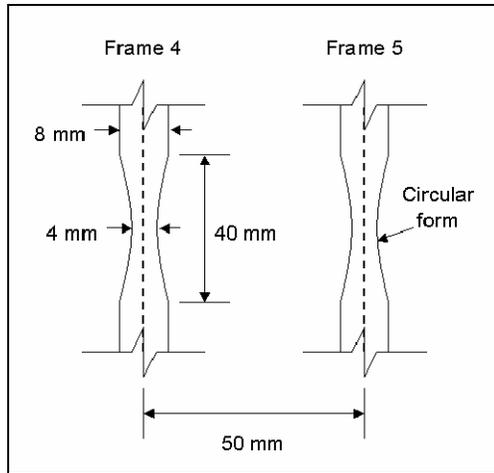
Figure 8. *'Dog-bone' flange corrosion on long cylinder*
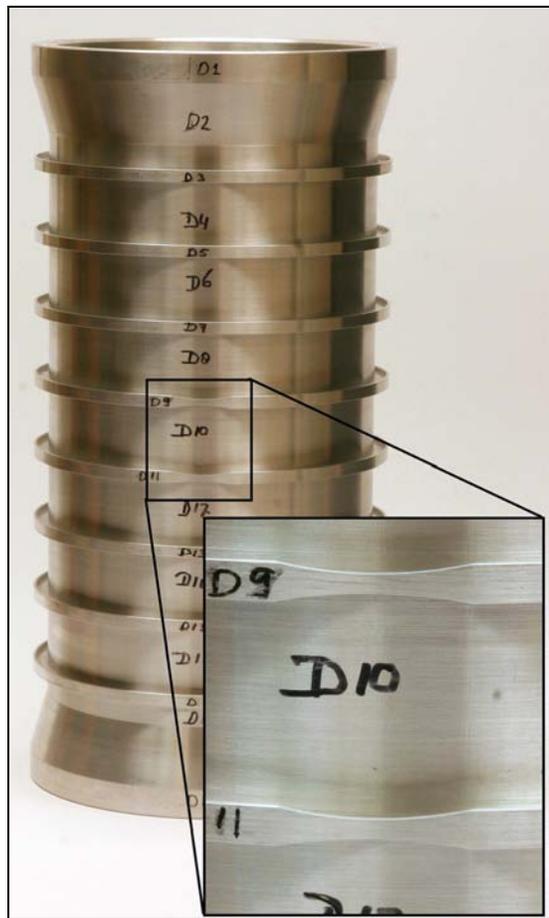
Figure 9. *Photograph of long cylinder with 'dog-bone' flange corrosion*

2.2.3 Cylinder with Penetrations

The cylinder with penetrations was designed to fail by overall collapse. The design geometry for this cylinder is shown in Figure 10. The cylinder was approximately the same length and radius as the long cylinders described in Section 2.2.2, with two important differences: 1) the cylinder was stiffened with external rectangular section rings rather than T-sections, and 2) the cylinder had two stiffened penetrations instead of simulated corrosion.
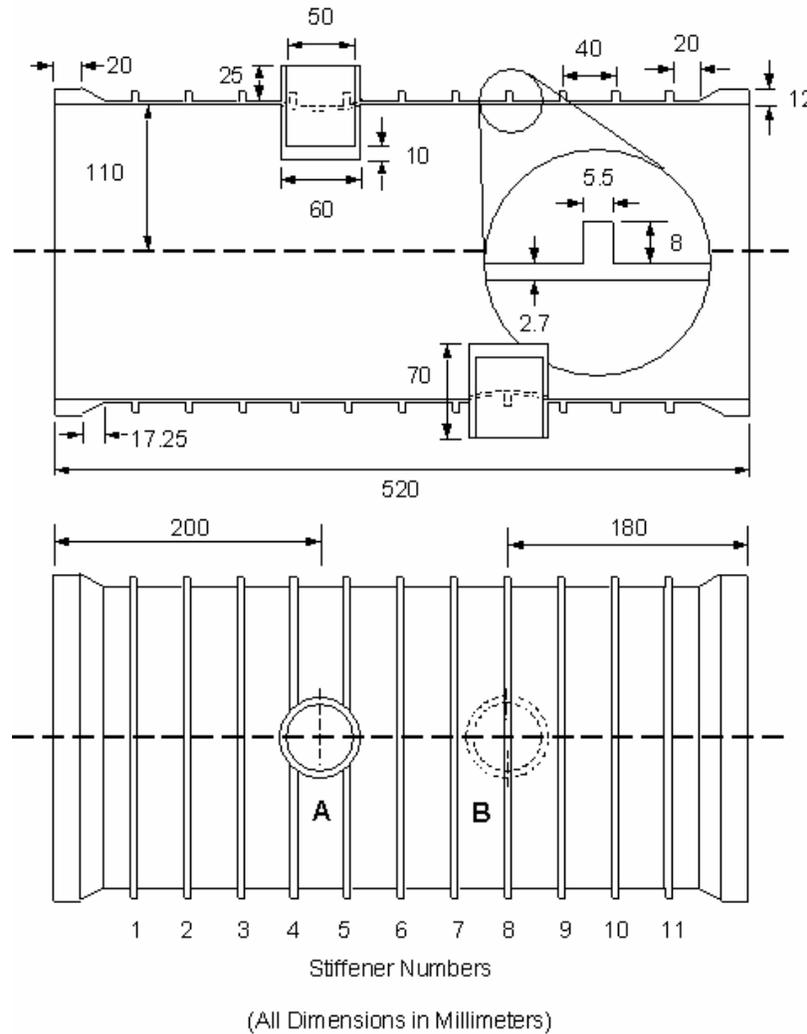
Figure 10. *Geometry of cylinder with penetrations*

The uniformly spaced bar-stiffeners of this cylinder were proportioned to be relatively weak compared with the shell in order to promote a global failure. The stiffener spacing is uniform over the length of the cylinder. This cylinder also had thick end rings to prevent end-bay failure. The strain gauge layout of the cylinder with penetrations is described in Section 2.6.3.

One penetration (A) was located at the crown ($0°$) and intersects stiffeners S4 and S5, and the other penetration (B) was at the keel ($180°$), intersecting stiffener S8 only (see Figure 10). The penetrations were reinforced by relatively stiff conning-tower-like structures (Figure 11), which were soldered to the cylinder shell. The conning towers were meant to simulate the behaviour of reinforced penetration structures in real pressure hulls, as well as to keep the penetrations sealed under external hydrostatic pressure.

Figure 11. *Photograph of cylinder with penetrations and close-up of crown penetration (A)*

2.3   Geometric Imperfections

Geometric imperfections are known to significantly reduce the strength of buckling-critical shell structures [7]. Geometric imperfections in pressure hulls are an inevitable result of the fabrication process. The deviation of a section from a perfect circle, referred to as out-of-circularity (OOC), is the most significant form of geometric imperfection for pressure hulls, and is typically measured at the stiffeners. An additional form of geometric imperfections in real pressure hulls is the dishing and bulging of the shell between stiffeners, often in the form of dimples distributed about the circumference. These dimples are referred to as interframe nucleators due to their tendency to initiate interframe collapse of the shell.

2.3.1 Methodology

Geometric imperfections in the specimens were determined by measuring the radius of the cylinders about the circumference at the stiffeners and at the shell at mid-bay. The raw OOC data (i.e. radius or eccentricity values at equal circumferential intervals) can be found in Annex A. The maximum eccentricity and Fourier amplitudes were calculated for each axial measurement location of each cylinder.

Maximum eccentricity refers to the maximum absolute value of the deviation from the mean radius, reported in units of distance or as a percentage of the mean radius at that axial location. Maximum eccentricity is a good indicator of the general level of imperfection in the specimen. Pressure hulls are typically designed to accommodate a maximum eccentricity of 0.5% of the mean shell radius and are built to a tolerance of one-third of this value [4].

The measured radii were converted into a quantifiable and easily understood measure of imperfection by means of Fourier series expansion. The radius, $R(\theta)$, at a particular angle, θ, is defined by the Fourier series expression [8]:

$$R(\theta) = b_0 + a_1 \sin\theta + b_1 \cos\theta + \sum_{n=2}^{\infty} \left(a_n \sin n\theta + b_n \cos n\theta \right) \tag{1}$$

where b_0 is the average radius, a_1 and b_1 represent the offset from the true centre of the data, and a_n and b_n are the Fourier coefficients for a particular wave number, n. The Fourier amplitude, A_n, is taken as:

$$A_n = \sqrt{a_n{}^2 + b_n{}^2} \tag{2}$$

and is an indication of the contribution to OOC by the mode, n, which refers to the number of complete waves about the circumference.

The Fourier coefficients can be calculated from evenly spaced discrete data using the following expressions:

$$b_0 = \frac{1}{N} \sum_{i=0}^{N-1} R(\theta_i) \tag{3}$$

$$a_1 = \frac{2}{N} \sum_{i=0}^{N-1} R(\theta_i) \sin\theta_i \,, \; a_n = \frac{2}{N} \sum_{i=0}^{N-1} R(\theta_i) \sin n\theta_i \tag{4}$$

$$b_1 = \frac{2}{N} \sum_{i=0}^{N-1} R(\theta_i) \cos\theta_i \,, \; b_n = \frac{2}{N} \sum_{i=0}^{N-1} R(\theta_i) \cos n\theta_i \tag{5}$$

where $\theta_i = \left(2\pi i / N \right)$. Practical and theoretical considerations limit the calculation of Fourier coefficients to values of $n < N/2$ [8].

2.3.2 Short Cylinders

For the short cylinders, OOC was quantified by taking radial measurements at eleven axial locations (Figure 12). At each axial location, 36 equally spaced measurements were taken about the circumference (10° increments). Exclusively outer radii were measured for all axial locations except the central bay (R6), where inner radii were also determined to allow the shell thickness to be estimated (see Section 2.4). Radial measurements were taken using the Zeiss UMM550 coordinate-measuring machine, which had a precision of 0.001 mm. Maximum eccentricity at each axial measurement location is reported for each specimen, as well as Fourier amplitudes up to and including wave number n=18 ($N/2$).
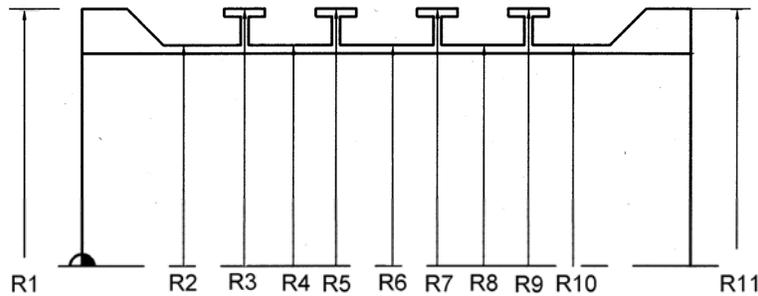
Figure 12. *Schematic drawing of OOC measurement locations for short cylinders*

The simulated corrosion damage in specimens L300-No3 and L300-No4 would add a component to the geometric imperfection (if the measured outer radii at the corrosion were used in calculations directly). To avoid this, the maximum eccentricities and Fourier amplitudes at axial locations with corrosion were determined using a radius value at the shell corrosion equal to the average value of radius at adjacent measurement points on the shell.

In general, OOC of the short cylinder specimens was greatest at the end locations, with the maximum eccentricity and Fourier amplitudes tending to diminish towards the central bay. Average values for radii differed from the nominal value, with some axial locations showing exact agreement. For a typical short cylinder, the n=2 mode dominated the OOC, especially at the end locations, while the n=3 mode became increasingly significant towards the centre of the specimen.

Maximum measured eccentricities for specimens L300-No2, L300-No3, and L300-No4 are summarized in Table 1, Table 3, and Table 5, respectively. Calculated Fourier amplitudes for the respective specimens can be found in Table 2, Table 4, and Table 6. Fourier amplitudes have only been reported for values of $n \leq 6$, as amplitudes corresponding to great n-values are negligible.

Table 1. *Maximum eccentricity relative to mean radius (mm) – L300-No2*

Location	Maximum eccentricity (mm)	Maximum eccentricity (%)
R1	0.091	0.073
R2	0.089	0.079
R3	0.081	0.065
R4	0.085	0.076
R5	0.074	0.060
R6 (in)	0.069	0.062
R6 (out)	0.084	0.075
R7	0.076	0.061
R8	0.087	0.077
R9	0.084	0.068
R10	0.074	0.066
R11	0.086	0.069
MEAN	0.082	0.069
ST. DEV.	0.007	0.007

Table 2. *Fourier amplitude (mm) for a given wave number (L300-No2)*

n	R1	R2	R3	R4	R5	R6 (In)	R6 (Out)	R7	R8	R9	R10	R11
0	124.98	112.51	124.50	112.50	124.50	110.00	112.50	124.50	112.49	124.51	112.49	124.98
1	0.039	0.039	0.039	0.038	0.039	0.002	0.041	0.039	0.039	0.039	0.039	0.044
2	0.049	0.055	0.049	0.054	0.043	0.052	0.045	0.036	0.033	0.030	0.025	0.041
3	0.008	0.000	0.005	0.011	0.009	0.017	0.019	0.016	0.015	0.012	0.006	0.027
4	0.002	0.005	0.002	0.006	0.002	0.001	0.004	0.002	0.006	0.004	0.002	0.007
5	0.001	0.005	0.003	0.002	0.001	0.001	0.001	0.001	0.006	0.002	0.002	0.006
6	0.001	0.003	0.001	0.004	0.001	0.001	0.002	0.001	0.002	0.002	0.002	0.002

Table 3. *Maximum eccentricity relative to mean radius (mm) – L300-No3*

Location	Maximum eccentricity (mm)	Maximum eccentricity (%)
R1	0.034	0.027
R2	0.019	0.017
R3	0.016	0.013
R4	0.027	0.024
R5	0.016	0.013
R6 (in)	0.018	0.016
R6[1] (out)	0.035	0.031
R7	0.025	0.020
R8	0.040	0.036
R9	0.031	0.025
R10	0.034	0.030
R11	0.062	0.049
MEAN	0.030	0.025
ST. DEV.	0.013	0.011

1. Maximum eccentricities were determined using a radius value at the shell corrosion equal to the average value of radius at the adjacent measurement points on the shell.

Table 4. *Fourier amplitude (mm) for a given wave number (L300-No3)*

n	R1	R2	R3	R4	R5	R6 (In)	R6[1] (Out)	R7	R8	R9	R10	R11
0	124.96	112.48	124.47	112.47	124.47	109.99	112.46	124.47	112.46	124.47	112.47	124.95
1	0.007	0.005	0.005	0.002	0.006	0.004	0.003	0.008	0.009	0.012	0.011	0.020
2	0.013	0.013	0.007	0.006	0.002	0.004	0.006	0.009	0.015	0.018	0.020	0.035
3	0.012	0.003	0.003	0.010	0.011	0.009	0.020	0.014	0.018	0.009	0.010	0.022
4	0.003	0.006	0.003	0.005	0.004	0.004	0.012	0.006	0.013	0.004	0.007	0.007
5	0.001	0.004	0.001	0.004	0.001	0.001	0.002	0.002	0.011	0.004	0.004	0.003
6	0.000	0.005	0.001	0.005	0.001	0.001	0.005	0.001	0.001	0.001	0.003	0.001

1. Fourier amplitudes were determined using a radius value at the shell corrosion equal to the average value of radius at the adjacent measurement points on the shell.

Table 5. *Maximum eccentricity relative to mean radius (mm) – L300-No4*

Location	Maximum eccentricity (mm)	Maximum eccentricity (%)
R1	0.074	0.059
R2	0.078	0.069
R3	0.057	0.046
R4	0.064	0.057
R5	0.057	0.046
R6 (in)	0.066	0.060
R6[1] (out)	0.071	0.063
R7	0.064	0.052
R8	0.073	0.065
R9	0.056	0.045
R10	0.056	0.050
R11	0.051	0.041
MEAN	0.064	0.054
ST. DEV.	0.009	0.009

1. Maximum eccentricities were determined using a radius value at the shell corrosion equal to the average value of radius at the adjacent measurement points on the shell.

Table 6. *Fourier amplitude (mm) for a given wave number (L300-No4)*

n	R1	R2	R3	R4	R5	R6 (In)	R6[1] (Out)	R7	R8	R9	R10	R11
0	124.99	112.52	124.50	112.52	124.51	109.98	112.52	124.50	112.52	124.50	112.52	124.97
1	0.023	0.026	0.024	0.024	0.024	0.001	0.026	0.025	0.028	0.026	0.030	0.031
2	0.041	0.040	0.039	0.045	0.038	0.045	0.042	0.030	0.026	0.017	0.009	0.013
3	0.010	0.004	0.004	0.018	0.015	0.023	0.025	0.022	0.032	0.021	0.020	0.007
4	0.002	0.003	0.002	0.006	0.002	0.004	0.003	0.003	0.008	0.004	0.009	0.010
5	0.001	0.006	0.001	0.002	0.001	0.001	0.005	0.002	0.008	0.005	0.010	0.006
6	0.001	0.003	0.001	0.004	0.001	0.001	0.003	0.001	0.004	0.001	0.005	0.002

1. Fourier amplitudes were determined using a radius value at the shell corrosion equal to the average value of radius at the adjacent measurement points on the shell.

2.3.3 Long Cylinders

Out-of-circularity for the long cylinders was measured in a similar manner to that used for the short specimens. Radial measurements were taken at nineteen axial locations (Figure 13). Only outer radii were measured at all axial locations except the central bay (R10), where inner radii were also measured to allow the shell thickness to be estimated (see Section 2.4).
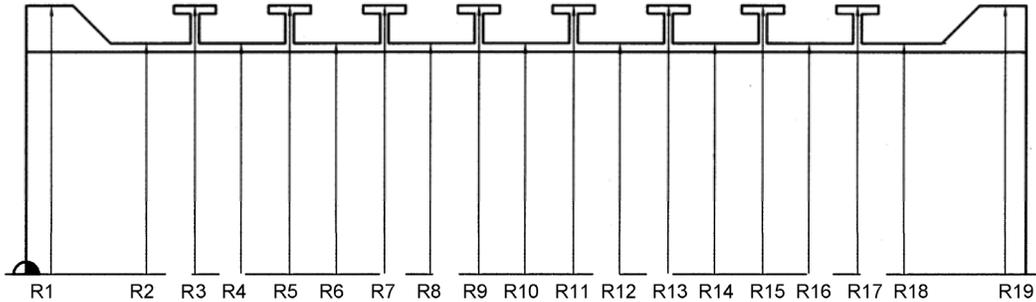
Figure 13. *Schematic drawing of OOC measurement locations for long cylinders*

Maximum measured eccentricities for specimens L510-No1 and L510-No2 are summarized in Table 7 and Table 9, respectively. Calculated Fourier amplitudes, for values of $n\leq6$, for the respective specimens can be found in Table 8 and Table 10.

Table 7. *Maximum eccentricity relative to mean radius (mm) – L510-No1*

Location	Maximum eccentricity (mm)	Maximum eccentricity (%)
R1	0.160	0.128
R2	0.107	0.095
R3	0.096	0.078
R4	0.088	0.078
R5	0.061	0.050
R6	0.071	0.063
R7	0.074	0.060
R8	0.075	0.066
R9	0.071	0.057
R10 (In)	0.068	0.061
R10 (Out)	0.081	0.071
R11	0.075	0.061
R12	0.078	0.069
R13	0.072	0.058
R14	0.080	0.071
R15	0.078	0.063
R16	0.074	0.065
R17	0.070	0.057
R18	0.070	0.062
R19	0.079	0.063
MEAN	0.081	0.069
ST. DEV.	0.021	0.017

Table 8. *Fourier amplitude (mm) for a given wave number (L510-No1)*

n	R1	R2	R3	R4	R5	R6	R7	R8	R9	R10 (in)
0	124.99	113.01	123.02	113.00	123.01	113.00	123.01	113.01	123.01	109.96
1	0.037	0.034	0.033	0.036	0.032	0.033	0.034	0.033	0.033	0.033
2	0.132	0.077	0.067	0.047	0.030	0.018	0.017	0.021	0.030	0.034
3	0.006	0.020	0.024	0.029	0.024	0.026	0.021	0.019	0.012	0.008
4	0.005	0.004	0.004	0.004	0.002	0.003	0.004	0.004	0.002	0.001
5	0.001	0.002	0.001	0.000	0.001	0.002	0.001	0.001	0.001	0.002
6	0.002	0.001	0.001	0.001	0.001	0.001	0.000	0.001	0.001	0.001

n	R10 (Out)	R11	R12	R13	R14	R15	R16	R17	R18	R19
0	113.01	123.01	113.00	123.01	113.01	123.00	113.00	123.00	113.00	124.98
1	0.036	0.037	0.042	0.042	0.049	0.050	0.052	0.058	0.062	0.056
2	0.036	0.040	0.043	0.041	0.039	0.034	0.029	0.024	0.015	0.032
3	0.013	0.009	0.011	0.009	0.009	0.006	0.003	0.003	0.002	0.012
4	0.001	0.001	0.001	0.002	0.001	0.003	0.006	0.006	0.007	0.006
5	0.001	0.001	0.001	0.001	0.003	0.002	0.006	0.004	0.005	0.001
6	0.001	0.001	0.001	0.001	0.001	0.001	0.002	0.001	0.003	0.006

Table 9. *Maximum eccentricity relative to mean radius (mm) – L510-No2*

Location	Maximum eccentricity (mm)	Maximum eccentricity (%)
R1	0.134	0.107
R2	0.060	0.053
R3	0.064	0.052
R4	0.052	0.046
R5	0.044	0.036
R6	0.047	0.041
R7	0.047	0.038
R8	0.059	0.052
R9	0.054	0.044
R10 (In)	0.057	0.052
R10 (Out)	0.064	0.057
R11	0.056	0.046
R12	0.056	0.049
R13	0.050	0.040
R14	0.054	0.047
R15	0.048	0.039
R16	0.056	0.049
R17	0.047	0.038
R18	0.049	0.043
R19	0.039	0.031
MEAN	0.057	0.048
ST. DEV.	0.019	0.015

In general, the magnitude of OOC for the long cylinders specimen was greatest at one or both ends, while the maximum eccentricity and Fourier amplitudes tended to be more uniform in the rest of the cylinder (L510-No1), or to diminish toward one end (L510-No2). Average values of radii differed from the nominal value, but some locations showed exact agreement. Typically, the *n*=2 mode shape dominated the OOC for most axial measurement locations. As with the short cylinders, the *n*=3 mode shape grew towards the centre of the specimen.

Table 10. Fourier amplitude (mm) for a given wave number (L510-No2)

n	R1	R2	R3	R4	R5	R6	R7	R8	R9	R10 (in)
0	124.98	113.01	123.00	113.01	122.99	113.01	123.00	113.01	123.00	110.04
1	0.004	0.016	0.011	0.011	0.012	0.010	0.011	0.009	0.010	0.003
2	0.096	0.041	0.036	0.017	0.011	0.018	0.025	0.037	0.039	0.044
3	0.040	0.013	0.022	0.031	0.028	0.029	0.022	0.023	0.016	0.012
4	0.004	0.002	0.003	0.006	0.004	0.005	0.005	0.005	0.002	0.003
5	0.004	0.001	0.002	0.004	0.003	0.003	0.001	0.002	0.000	0.003
6	0.004	0.004	0.002	0.001	0.000	0.001	0.001	0.001	0.001	0.002

n	R10 (Out)	R11	R12	R13	R14	R15	R16	R17	R18	R19
0	113.01	123.01	113.00	123.02	113.00	123.02	113.00	123.02	113.03	125.00
1	0.009	0.011	0.010	0.011	0.010	0.010	0.008	0.010	0.011	0.011
2	0.049	0.046	0.051	0.045	0.048	0.040	0.042	0.033	0.030	0.025
3	0.017	0.012	0.012	0.008	0.006	0.004	0.001	0.002	0.006	0.007
4	0.002	0.003	0.003	0.001	0.001	0.004	0.004	0.002	0.003	0.002
5	0.001	0.001	0.002	0.002	0.002	0.001	0.003	0.003	0.005	0.001
6	0.001	0.001	0.001	0.001	0.000	0.001	0.002	0.001	0.001	0.001

2.3.4 Cylinder with Penetrations

A different geometric measurement technique was used for the cylinder with penetrations. OOC was quantified by directly measuring the eccentricity at each stiffener (S1 through S9) and at end rings (E1 and E2). The cylinder was mounted on a lathe, which allowed it to be turned about the longitudinal axis. A displacement dial gauge was fixed, such that it was in contact with, and normal to, the stiffener being measured. The cylinder was manually turned and, at each axial location, 18 equally spaced measurements were taken about the circumference (20° increments). The data were eccentricities at each stiffener, which allowed the OOC shapes to be extracted, but not the mean radii.

The measured data was zeroed with respect to the first (0°) measurement location, and then the mean value was subtracted from each datum to give the radial eccentricity at that point (a negative value indicates an inward eccentricity). The penetrations prevented measurements from being taken at certain locations (0° at S4 and S5, and 160° and 180° at S8). Eccentricity data for these points were linearly interpolated from the adjacent locations in order to allow Fourier analyses to be undertaken.

Maximum eccentricity at each axial measurement location is reported, as well as Fourier amplitudes up to and including wave number $n=9$ ($N/2$). Wave number $n=0$ has not been reported, as it has been set to zero by subtracting the mean value of eccentricity as described above. Likewise, the $n=1$ amplitudes have not been reported.

Maximum eccentricity and Fourier amplitudes for the cylinder with penetrations are summarized in Table 11 and Table 12, respectively.

Table 11. Maximum eccentricities for the cylinder with penetrations

Location	Maximum eccentricity (mm)	Maximum eccentricity[1] (%)
E1	0.233	0.191
S1	0.180	0.149
S2	0.138	0.114
S3	0.135	0.112
S4	0.123	0.102
S5	0.114	0.094
S6	0.096	0.079
S7	0.102	0.085
S8	0.145	0.120
S9	0.176	0.146
S10	0.210	0.174
S11	0.213	0.177
E2	0.228	0.187
MEAN	0.161	0.133
ST. DEV.	0.048	0.040

1. Maximum eccentricities (%) were determined using the nominal radius value at the point of measurement, as measured values of radius were not available.

The magnitude of OOC for this specimen was greatest at the end locations and diminished towards the central bay. The $n=2$ mode shape dominated the OOC, except at a single stiffener (S8), where the $n=3$ amplitude was greater.

Table 12. Fourier amplitude (mm) for a given wave number (cylinder with penetrations)

n	E1	S1	S2	S3	S4	S5	S6	S7	S8	S9	S10	S11	E2
2	0.189	0.149	0.132	0.102	0.072	0.049	0.030	0.024	0.030	0.069	0.079	0.100	0.115
3	0.048	0.039	0.026	0.016	0.020	0.017	0.006	0.013	0.033	0.017	0.010	0.008	0.007
4	0.023	0.018	0.004	0.005	0.014	0.008	0.012	0.005	0.007	0.011	0.010	0.007	0.013
5	0.020	0.005	0.010	0.005	0.005	0.003	0.005	0.005	0.009	0.008	0.006	0.004	0.009
6	0.005	0.009	0.006	0.004	0.004	0.006	0.003	0.005	0.004	0.010	0.009	0.004	0.007
7	0.005	0.006	0.003	0.002	0.004	0.005	0.006	0.000	0.007	0.010	0.005	0.003	0.004
8	0.011	0.009	0.002	0.001	0.002	0.004	0.005	0.002	0.008	0.007	0.005	0.007	0.003
9	0.008	0.010	0.001	0.004	0.011	0.001	0.003	0.001	0.001	0.001	0.003	0.003	0.007

2.4 Shell Thickness

Internal radii were measured at mid-length for the short and long T-stiffened cylinders. Measurements were taken at circumferential locations coinciding with the external measurement locations, which allowed the shell thickness in the central bay of each specimen to be determined by subtracting the inner from the outer radii at each location. Shell thickness data for the penetration model was not available.

Average shell thicknesses in the central bay are reported in Table 13 for the short and long cylinders. For the short cylinders, the average shell thickness in the undamaged regions was found to be less than the design value (2.5 mm) for all but one specimen (L300-No4). The average measured shell thickness for each cylinder was found to be within ±2% of the specified value. Individual measured shell thicknesses were found to be within ±3.5% of the specified values.

Table 13. Measured shell thickness for short and long cylinders

SPECIMEN	MEAN SHELL THICKNESS IN CENTRAL BAY (mm)			
	Undamaged region		Corroded region	
	Design	*Measured*	*Design*	*Measured*
L300-No2	2.500	2.496	N/A	N/A
L300-No3	2.500	2.477	1.875	1.870
L300-No4	2.500	2.544	1.875	1.904
L510-No1	3.000	3.052	N/A	N/A
L510-No2	3.000	2.972	N/A	N/A

Shell thinning in the damaged short cylinders was specified to be 25% of the nominal shell thickness. The actual reduction in shell thickness in the corroded regions, relative to the average shell thickness in the central bay, was found to be 24.5% and 25.2% for specimen L300-No3 and L300-No4, respectively.

Complete thickness measurements about the circumference of the central bays of the short and long cylinders can be found in Annex B.

2.5 Material Properties

The T-stiffened cylinders were fabricated from 6082-T6 aluminium tubing, which has a nominal yield stress and tensile strength of 260 and 310 MPa, respectively [9]. Tensile coupon tests were undertaken by Schielab b.v. to validate the nominal material properties of the cylinder material. The value of Poisson's ratio was assumed to be 0.3.

A single set of tensile tests was performed on the base material for the T-stiffened cylinders. Tensile specimens had a circular cross-section, with a diameter of 14 mm. Six tensile specimens were tested to compute an average value of the yield stress and tensile strength of the material, which were found to be 302.4 and 373.7 MPa, respectively. Detailed elongation data from two of the tensile coupons was obtained in order to calculate Young's modulus, which was determined to be 71,350 MPa, and the strain hardening modulus, which was found to be approximately 1,400 MPa. Test results for individual tensile coupons can be found in Table 14. Figure 14 shows a typical stress-strain curve for the short and long cylinders.

Table 14. *Material properties for short and long cylinders*

TENSILE COUPON I.D.	YIELD STRESS (%0.2)	TENSILE STENGTH	YOUNG'S MODULUS
	(MPa)	*(MPa)*	*(MPa)*
1905-1	300.5	374.0	N/A
1905-2	293.7	374.9	N/A
1905-3	303.4	375.4	N/A
1966-1	300.3	373.9	N/A
1966-2	307.7	373.1	73,800
1966-3	308.8	371.0	68,900
Average	**302.4**	**373.7**	**71,350**
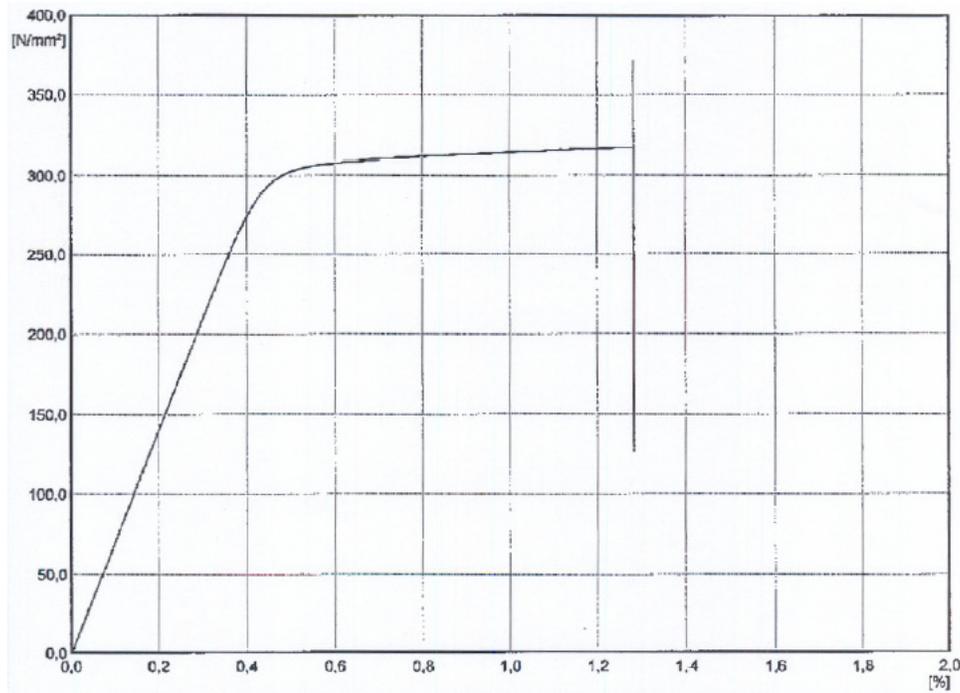
Figure 14. *Typical stress-strain relationship for T-stiffened cylinders (coupon No. 1966-3)*

Tensile coupon data for the aluminium alloy tubing (6061-T6) from which the penetration model was fabricated indicated a yield stress between 240 and 260 MPa, Young's modulus equal to 71,000 MPa, and Poisson's ratio equal to 0.32 [3]. The strain hardening modulus and tensile strength were found to be 7,000 and 270 MPa, respectively. Compared to the T-stiffened cylinder material, the penetration model material showed lower yield strength (250 MPa versus 300 MPa), but a higher degree of strain hardening (10% versus 2%).

2.6 Instrumentation

Strain gauges were attached to the specimens, using a general-purpose strain gauge adhesive, in order to allow strain, and therefore stress, to be monitored during testing. Where two nominally identical specimens were tested, only one was instrumented with strain gauges. Both uni-axial gauges (Micro-Measurements *CEA-13-250UW-350*) and rosettes (Micro-Measurements *WK-13-060WY-350*) were used.

The change in resistance of the strain gauges, and hence the strain, was measured using a Wheatstone bridge, whereby strain is determined using the following equation:

$$\varepsilon = 4\frac{V_{out}}{V_{in}k_g G}x10^6 \tag{6}$$

where ε is the strain (microstrain), V_{out} is the measured output voltage, V_{in} is the input excitation voltage to the Wheatstone bridge, k_g is the strain gauge factor as specified by the manufacturer, and G is the amplification gain for V_{out}. All tests used an input voltage of 10V and a gain of 100. Gauge factors were 2.11 and 2.10 for uni-axial and rosette gauges, respectively.

The following sections describe the locations of strain gauges for the instrumented cylinders (L300-No3, L510-No1, and the cylinder with penetrations).

2.6.1 Short Cylinders

L300-No3

Strain gauges were applied to the short cylinder with corrosion (L300-No3) as shown in Figure 15 and described as follows (note that 0° coincides with the centre of the corrosion patch):

- Outside gauges

  - 8 uni-axial gauges about the circumference (0°, 10°, 45°, 90°, 180°, 270°, 315°, and 350°), in the circumferential direction, on the two central frame flanges (2 x 8 = 16 gauges) – these gauges are intended to measure any overall component to the collapse mode shape

  - 4 gauge locations about the circumference (0°, 90°, 180°, and 270°), in both the axial and circumferential directions, on the outside of the shell at

the midpoint of the central bay (2 x 4 = 8 gauges) – these gauges are intended to allow verification of the design formulae stresses, provide information on the mode of failure, as well as show the stresses at the corrosion

- 4 gauge locations about the circumference (0°, 90°, 180°, and 270°), in the circumferential direction only, on the outside of the shell at the butt of the T-section stiffener (2 x 4 = 8 gauges) – these gauges are intended to allow verification of the design formulae stresses, as well as provide information on the mode of failure

- Total of 16 + 8 + 8 = 32 gauges on the outside of the cylinder

- Inside gauges

  - 8 gauge locations about the circumference (0°, 10°, 45°, 90°, 180°, 270°, 315°, and 350°), in both the axial and circumferential directions, on the inside of the shell at the midpoint of the central bay (2 x 8 = 16 gauges) – these gauges are intended to allow verification of the design formulae stresses, as well as provide information on the mode of failure

  - Total of 16 gauges on the inside of the cylinder

- Grand Total of 48 gauges
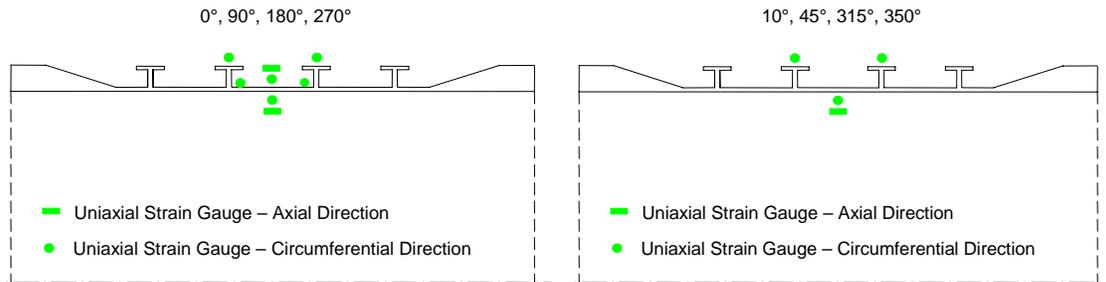
Figure 15. Strain gauge layout for short cylinder with simulated corrosion (L300-No3)

2.6.2 Long Cylinders

L510-No1

Strain gauges were applied to the undamaged long cylinder (L510-No1) as shown in Figure 16 and described as follows:

- Outside gauges

  - 12 uni-axial gauges about the circumference (30° increments), in the circumferential direction, on the two central frame flanges (2 x 12 = 24

gauges) – these gauges are intended to measure the overall collapse mode shape

- 6 uni-axial gauges about the circumference (60° increments), in both the axial and circumferential directions, on the outside of the shell at the midpoint of the central bay (2 x 6 = 12 gauges) – these gauges are intended to allow verification of the design formulae stresses, as well as provide information on the mode of failure

- 6 uni-axial gauges about the circumference (60° increments), in the axial direction only, on the outside of the shell in the outermost complete bays (2 x 6 = 12 gauges) – these gauges are intended to provide strain data in the case of an axisymmetric end bay failure (accordion-type collapse)

- Total of 24 + 12 + 12 = 48 gauges on the outside of the cylinder

- Inside gauges

  - 6 uni-axial gauges about the circumference (60° increments), in both the axial and circumferential directions, on the inside of the shell at the midpoint of the central bay (2 x 6 = 12 gauges) – these gauges are intended to allow verification of the design formulae stresses, as well as provide information on the mode of failure

  - Total of 12 gauges on the inside of the cylinder

- Grand Total of 60 gauges
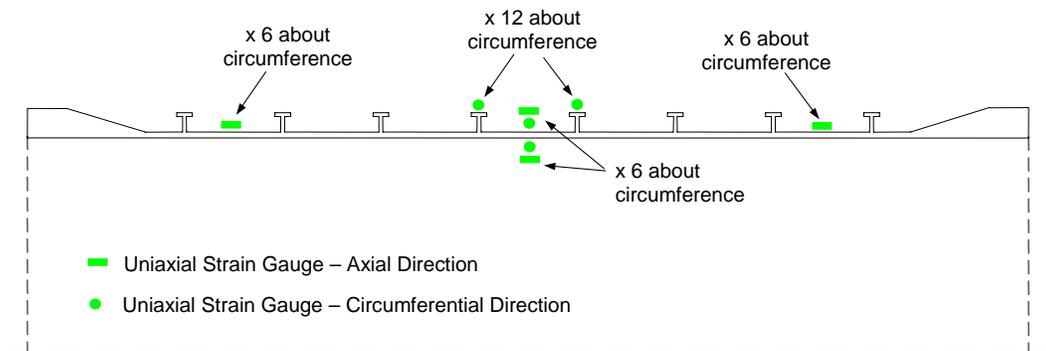
Figure 16. Strain gauge layout for undamaged long cylinder (L510-No1)

2.6.3 Cylinder with Penetrations

Strain gauges were applied to the cylinder with penetrations as shown in Figure 17 and Figure 18, and described as follows:

- Outside gauges

- 18 uni-axial gauges about the circumference (20° increments), in the circumferential direction, on the central bar stiffener (18 gauges) – these gauges are intended to measure any overall component to the collapse mode shape

- 2 uni-axial gauges in the circumferential direction (15° and 345°) near penetration A on stiffeners #4 and #5 (2 x 2 = 4 gauges) – these gauges are intended to provide information on the stresses around the penetration and for validation of numerical analyses

- 2 uni-axial gauges in the circumferential direction (165° and 195°) near penetration B on stiffener #8 (1 x 2 = 2 gauges) – these gauges are intended to provide information on the stresses around the penetration and for validation of numerical analyses

- 3 strain rosettes on the inner wall of each penetration, located at the level of the intersecting shell at 0°, 45° and 90° (2 x 3 x 3 = 18 gauges). The rosettes had a 60° incremental angle, with the middle gauge of each rosette aligned vertically. These gauges are intended to provide information on the principal stresses in the penetrations and for validation of numerical analyses.

- Total of 18 + 4 + 2 + 18 = 42 gauges on the outside of the cylinder

- Inside gauges

  - 18 uni-axial gauges about the circumference (20° increments), in the circumferential direction, on the shell opposite the central bar stiffener (18 gauges) – these gauges are intended to pick up any overall component to the collapse mode shape

  - Total of 18 gauges on the inside of the cylinder

- Grand Total of 60 gauges

Stiffener #4 & 5   Stiffener #6   Stiffener #8
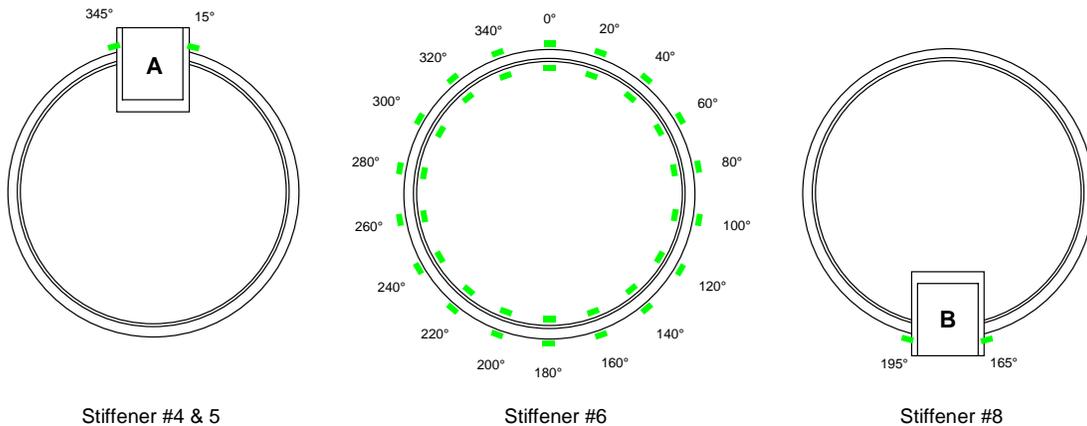
Figure 17. Uni-axial strain gauge layout for cylinder with penetrations
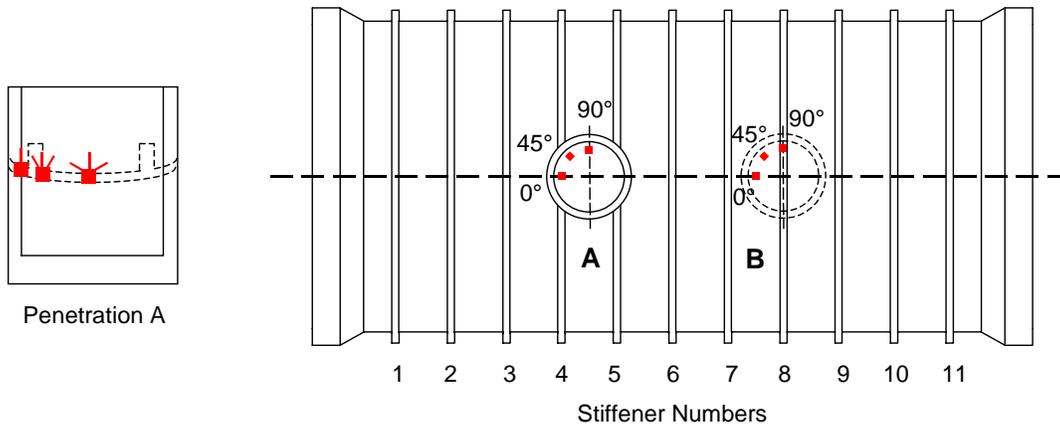
Figure 18. Rosette strain gauge layout for cylinder with penetrations

2.7 Analytical Calculations

Submarine design formulae (SDF) were used to determine nominal collapse pressures, collapse modes, and elastic stresses for the experimental specimens. The parameters that have been calculated are listed and described in Table 15, and, except where indicated, are based on formulations presented in Ref. [4].

Table 16 lists the SDF predictions for various modes of failure for the undamaged cylinders. The nominal geometry and measured material properties were used in these calculations. OOC amplitudes, which are required to calculate certain SDF parameters ($P_{y(n)}$, P_P, and P_{co}), were taken as 0.07 and 0.13% of the mean radius for the T-stiffened and rectangular section ring-stiffened cylinders, respectively. These values are associated with the maximum observed mean eccentricity as determined from measurements (see Section 2.3).

The design pressure was taken as the lowest of the interframe and overall collapse pressures, as defined by $P_{ci(mean)}$ and P_{co}, respectively. Based on these parameters, the SDF predicted that the short undamaged cylinder would fail by interframe collapse at 6.68 MPa. Interframe collapse modes are typically associated with the von Mises elastic buckling pressure (P_{m1}), which predicted an n=9 mode for the short cylinders.

The SDF predicted a similar interframe collapse for the long cylinders at 8.33 MPa, using the measurement-based value of OOC of 0.07%. The long cylinders, which were designed to fail in an overall mode, were proportioned assuming a larger degree of OOC than was found upon measurement. Furthermore, $P_{ci(mean)}$ is based on empirical data for cylinders with values of OOC up to 0.5% of the mean radius, and would therefore likely be conservative in this case. The use of the design value of OOC amplitude (0.3%) resulted in a design collapse pressure, governed by overall collapse (P_{co}), of 7.77 MPa.

The cylinder with penetrations had a predicted collapse pressure of 7.11 MPa in an overall collapse mode. Both of the basic cylinder geometries that were proportioned

to fail by overall collapse (long cylinders and the cylinder with penetrations) actually had similar design interframe and overall collapse pressures. This is due to the relatively small measured OOC amplitudes in the fabricated specimens.

Table 15. Description of calculated submarine design formulae parameters

P_{c3}	external pressure at which the circumferential stress at the outside of the plating midway between frames, σ_3, equals yield
P_{c5}	external pressure at which the mean circumferential stress in the plating midway between frames, σ_5, equals yield
P_{c6}	external pressure at which the mean stress in the plating reaches the Von Mises yield criterion
P_{c7}	external pressure at which the longitudinal stress on the inside of the plating, adjacent to the frame, σ_7, equals yield
P_{fy}	external pressure causing yield in the frame flange of an ideal circular ring-stiffened cylinder
P_{m1}	von Mises interframe elastic buckling pressure; iterated Kendrick solution
$P_{ci(lower)}$	interframe collapse pressure as determined from the BS5500 lower bound empirical curve [10]
$P_{ci(mean)}$	interframe collapse pressure as determined from the SSP 74 mean empirical curve [4]
P_N	Bryant overall buckling pressure
$P_{y(n)}$	external pressure causing overall collapse of a ring-stiffened cylinder, precipitated by frame yielding
P_P	external pressure causing overall collapse of a ring-stiffened cylinder, precipitated by shell yielding
P_{co}	external pressure causing overall elasto-plastic collapse of a ring-stiffened cylinder, as predicted by K79 [11]

The SDF predictions for the damaged specimens are reported in Table 17. These calculations were made using identical parameters as those used for the undamaged cylinders, except for the shell thickness in the short cylinders (1.875 mm) and the stiffener flange width in the long cylinders (4 mm).

The SDF calculations predicted an interframe failure at 4.28 MPa and an overall failure at 8.32 MPa for the short and long damaged cylinders, respectively. The use of the corroded geometry in the design calculations implies a uniform distribution of corrosion damage about the circumference, which is a conservative assumption.

The analytical calculations indicated a 36% decrease in the interframe collapse pressure for the short cylinder due to the corrosion damage. The ratio of elastic buckling pressure (P_{m1}) to the pressure causing shell yield (P_{c5}) in the short cylinders was relatively low (1.33). This indicates that shell failure is influenced by elastic buckling, and suggests that a decrease in shell thickness carries a greater penalty in collapse pressure than would be seen in yield-dominated failures.

Overall collapse (P_{co}) of the long cylinders was predicted to decrease by approximately 9% due to the reduced flange breadth. As mentioned above, the analytical calculations are restricted to modeling corrosion damage as a uniform material loss about the circumference. The damage would also be assumed, in this modeling approach, to be uniform over the length of the cylinder, which is a second source of conservativeness in this case.

Table 16. *SDF calculations for undamaged specimens*

PARAMETER	SHORT CYLINDER	LONG CYLINDER	CYLINDER WITH PENETRATIONS
Shell Yielding			
P_{c3}	6.87 MPa	8.31 MPa	6.83 MPa
P_{c5}	7.46 MPa	8.70 MPa	7.32 MPa
P_{c6}	8.60 MPa	10.04 MPa	8.39 MPa
P_{c7}	5.87 MPa	9.57 MPa	6.80 MPa
Stiffener Yielding			
P_{fy}	15.06 MPa	13.54 MPa	11.24 MPa
Interframe Collapse			
P_{m1}	15.06 MPa ($n = 9$)	23.61 MPa ($n = 8$)	28.00 MPa ($n = 9$)
$P_{ci(lower)}$	5.61 MPa	7.10 MPa	6.36 MPa
$P_{ci(mean)}$	6.68 MPa	8.33 MPa	7.47 MPa
Overall Collapse			
P_N	32.75 MPa ($n = 3$)	14.28 MPa ($n = 2$)	11.16 MPa ($n = 3$)
$P_{y(n)}$	13.91 MPa ($n = 3$)	10.39 MPa ($n = 3$)	7.23 MPa ($n = 3$)
P_P	8.46 MPa ($n = 6$)	8.70 MPa ($n = 3$)	6.69 MPa ($n = 3$)
P_{co}	8.77 MPa ($n = 4$)	9.13 MPa ($n = 3$)	7.11 MPa ($n = 3$)

Table 17. *SDF calculations for specimens with corrosion*

PARAMETER	SHORT CYLINDER	LONG CYLINDER
Shell Yielding		
P_{c3}	4.90 MPa	8.27 MPa
P_{c5}	5.33 MPa	8.58 MPa
P_{c6}	6.15 MPa	9.90 MPa
P_{c7}	3.80 MPa	10.41 MPa
Stiffener Yielding		
P_{fy}	13.85 MPa	12.83 MPa
Interframe Collapse		
P_{m1}	7.08 MPa ($n = 10$)	23.61 MPa ($n = 8$)
$P_{ci(lower)}$	3.33 MPa	7.02 MPa
$P_{ci(mean)}$	4.28 MPa	8.24 MPa
Overall Collapse		
P_N	25.58 MPa ($n = 3$)	10.74 MPa ($n = 3$)
$P_{y(n)}$	12.63 MPa ($n = 3$)	8.13 MPa ($n = 3$)
P_P	6.53 MPa ($n = 6$)	8.00 MPa ($n = 3$)
P_{co}	6.74 MPa ($n = 4$)	8.32 MPa ($n = 3$)

3.   Experimental Apparatus and Procedures

3.1   Specimen Preparation

Several steps were taken to prepare the cylinders before hydrostatic testing: 1) measurement of geometric imperfections (see Section 2.3), 2) application of strain gauges (see Section 2.6), and 3) connection of the strain gauges to the data acquisition system.

In addition, steel end-caps (Figure 19), manufactured at the DRDC Atlantic machine shop, were attached to the specimens before testing. These served several purposes: 1) to provide a watertight seal during the application of hydrostatic pressure, 2) to increase the weight of the specimens, thereby ensuring negative buoyancy in the testing tank, and 3) to provide additional stiffness to the cylinders at the boundaries. The end-caps were attached to the specimens using 12 equally spaced bolts. The end-caps also have a drain-hole at the centre, two threaded holes for attaching support cables, and four threaded holes for aiding in the removal of the end-caps after testing.
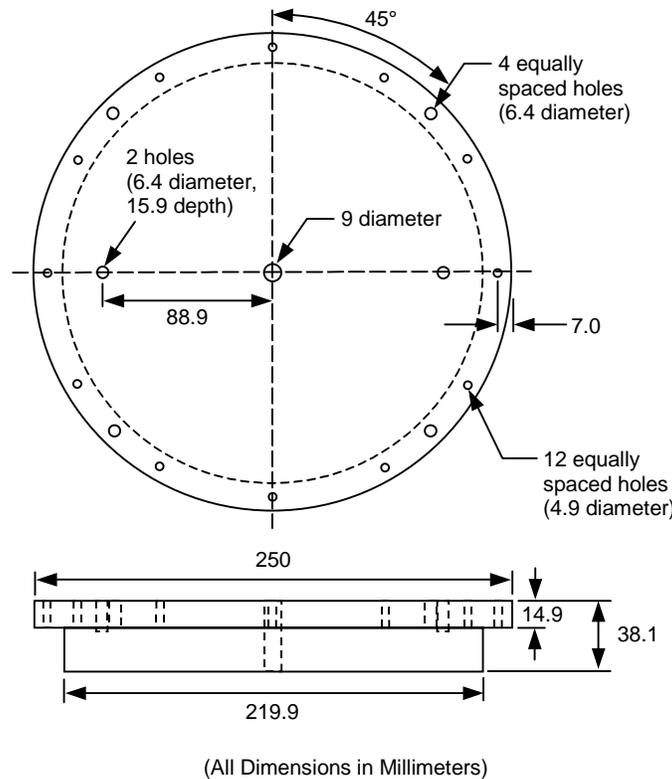
Figure 19. Schematic drawing of specimen end-cap (without hole for cables)

The cables attached to the strain gauges on the inside of the cylinder passed through a hole in one end-cap (Figure 20). A hardened resin (Scotchcast®, manufactured by

3M) was cast to fill the portion of the hole on the end-cap not taken up by these cables. The hole in the end-cap, as well as the end-cap-cylinder joint, was covered with fuel tank sealant (PR-1422, manufactured by PRC-Desoto International) to prevent leakage into the specimen during pressure testing.

Figure 20. Cylinder with instrumentation cables passing through end cap

3.2   Pressure Testing Apparatus

The cylinder specimens were tested to failure under hydrostatic pressure at the high-pressure testing facility at DRDC Atlantic. This pressure tank is capable of simulating depths of up to 7 km beneath the water surface. A schematic diagram of the pressure tank, which has a testing chamber approximately 2.5 m deep and 1 m in diameter, is shown in Figure 21.

All cables carrying signals from the strain gauges to the data acquisition system must pass through the tank without causing leakage or loss of pressure-tight integrity. This was accomplished by manufacturing aluminium cylinders to fit into existing holes in the tank bottom (see Figure 21). The cables were passed through these cylinders, which were fabricated at the DRDC Atlantic machine shop, the voids were filled using a hardened polymer resin, and the entire assembly was sealed with an adhesive polymer sealant.

Before testing, each specimen was placed in a porous canvas bag and mounted in a tripod test frame. The bag prevented any debris related to the collapse of the specimen to damage the mechanical pressurizing device in the tank. The entire assembly – specimen, bag, and test frame – were suspended from the lid of the pressure tank during testing.

Only the bottom portion of the tank was filled with water during testing. The top one-third of the tank (enough to cover the specimen) was filled with a non-conductive general-purpose mineral oil (Shell Vitrea® 22). This allowed the specimen to be pressurized with minimal risk of short-circuiting wires and cables.
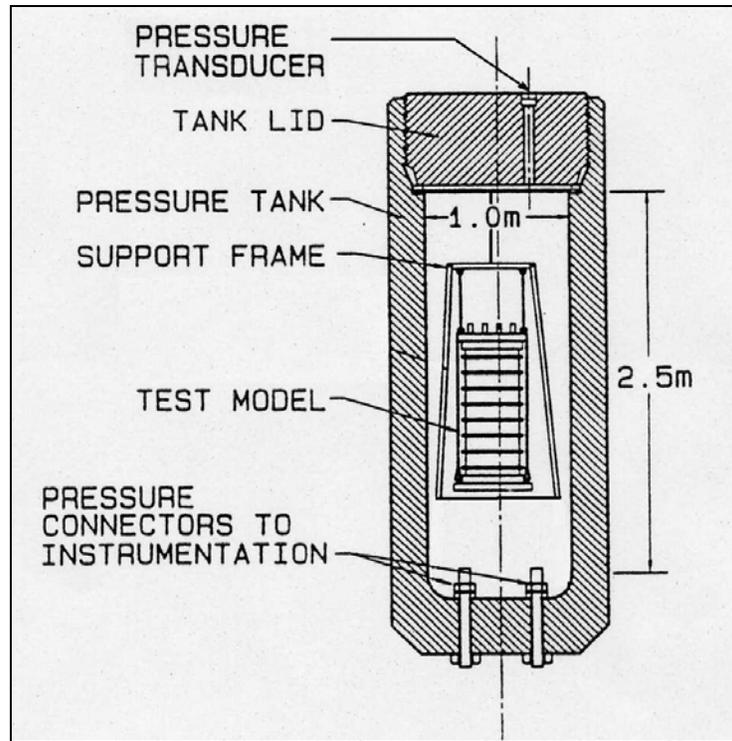
Figure 21. High-pressure tank at DRDC Atlantic

The tank was pressurized by pneumatically forcing small volumes of water into the filled and sealed tank. Hydrostatic pressure in the tank was measured using a pressure transducer, located on the lid of the tank. The transducer had a range of approximately 0 to 17.2 MPa and an accuracy of 0.25% over this range (0.043 MPa) for all errors. Pressures are reported to three significant figures, accurate to within ±0.04 MPa.

3.3   Testing Procedures

Table 18 describes the testing procedure for individual specimens. During a typical test, tank pressure was steadily increased, making occasional stops to check equipment and instrumentation, until collapse of the specimen occurred. The average loading rate was approximately 2.5 MPa/minute between instrumentation checks. The loading histories of the specimens can be seen in Figure 22, which plots the applied pressure against elapsed testing time for each specimen. Strain gauge and pressure data was recorded at 20 Hz for the duration of the test, both digitally (filtered) and in analog (unfiltered).

The testing of specimen L510-No1 was performed in two stages due to a shear failure of the resin in the instrumentation hole of the end-cap, which occurred before the peak load was reached. The resin failure can be seen to be developing when the load-time history is examined (Figure 22). The data for initial testing of this cylinder (L510-No1A) shows steady declines of pressure during the last few instrumentation checks. The resin failed shortly after this loss of pressure began, resulting in an immediate and complete loss of applied pressure (occurs at approximately 14.5 minutes in Figure 22) after which the test was stopped. The specimen was removed from the pressure tank and visual inspection revealed no signs of permanent deformation. However, analysis of strain data showed that certain regions of the specimen had yielded. The end-cap instrumentation hole was repaired using a stronger filler material (Epibond® multi-purpose epoxy adhesive, manufactured by Huntsman Advanced Materials), and the cylinder was tested to failure at a later date (L510-No1B).

Table 18. Testing procedure for individual specimens

SPECIMEN	DATE	NOTES
L300-No2	10 May 2005	External pressure was applied gradually until collapse of the specimen, holding briefly at approximately 3.4 MPa to check instrumentation. Collapse and rupture resulted in the loss of applied pressure immediately after peak load was reached.
L300-No3	26 Jul 2005	External pressure was applied gradually until collapse of the specimen, holding briefly at approximately 2.0 MPa to check instrumentation. Collapse and rupture resulted in the loss of applied pressure immediately after peak load was reached.
L300-No4	12 May 2005	External pressure was applied gradually until collapse of the specimen, holding briefly at approximately 2.7 MPa to check instrumentation. Collapse and rupture resulted in the loss of applied pressure immediately after peak load was reached.
L510-No1A	28 Apr 2005	External pressure was applied gradually, holding at 0.7 MPa increments to check instrumentation. Shear failure of the resin in the instrumentation hole of the end-cap occurred before specimen failure.
L510-No1B	6 Jul 2005	Second test of L510-No1. Same procedure as L300-No2.
L510-No2	16 May 2005	Same procedure as L300-No2.
Cylinder with penetrations	18 Jul 2005	Same procedure as L300-No3.
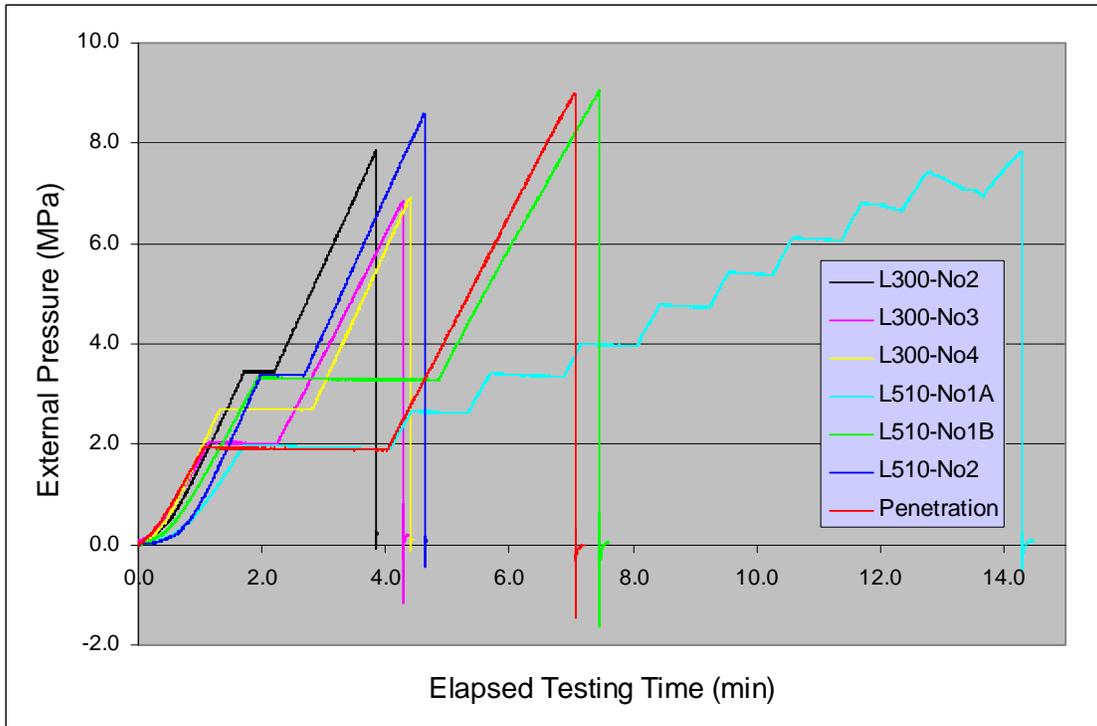
Figure 22. *Load-time histories for individual specimens*

3.4 Data Analysis Procedures

The following sections present the methodology of interpreting experimental results, including collapse pressures, strain data, and observed failure modes.

3.4.1 Determining Collapse Pressure

The collapse pressures reported in Section 4 were defined as the maximum external pressure resisted by each specimen, zeroed with respect to the initial pressure transducer reading. Thus, the collapse pressure is the ultimate load and does not indicate whether local instabilities occur prior to ultimate failure.

3.4.2 Determining Collapse Mode

For the experimental work described in this report, the collapse mode was determined using two methods: 1) analysis of the strain gauge data, when available, and 2) visual inspection of the specimen after testing. This is important for obtaining qualitative understanding of the collapse mechanism, as well as quantitative assessment of the collapse shape.

Strain gauges are used to directly determine the collapse mechanism, and indirectly to indicate the collapse shape, as well as to validate analytically calculated elastic

stresses. Since there is a practical limit to the number of strain gauges that can be applied to a specimen, gauges are placed in the most critical areas as determined by pretesting analysis. However, the location of the critical areas cannot always be predicted. Visual inspection of the cylinders after testing allows structural behaviour, which may not have been recorded by the strain gauges, to be observed.

Identification of the collapse mechanism

Collapse of pressure hulls can occur by elastic buckling, material yielding, or a combination of the two, and usually involves a high degree of nonlinear geometric behaviour.

Elastic buckling is indicated by linear behaviour of the strain-pressure curve, with failure occurring suddenly and with no material yielding before the ultimate load is reached. In practice, linear-elastic buckling is rarely observed because the presence of geometric imperfections leads to nonlinear structural behaviour, sometimes resulting in material yielding well before the ultimate load is reached. In addition, typical ring-stiffened pressure hulls are proportioned such that the elastic buckling load cannot be reached before the onset of material yielding, even in the absence of geometric imperfections.

Material yielding of the structure is indicated by strain gauges that have reached the 0.2% yield limit. Yielding in the shell will be governed by multi-dimensional stresses. Stresses in the ring-stiffeners were assumed to be uni-directional (circumferential), and a simple linear conversion of strain using Hooke's law was used to estimate stress. Yielding is said to occur whenever any of these uni-axial stresses have reached the yield stress.

The shell portions of the experimental specimens can be treated as ideal shell structures, and thus the in-plane stresses, rather than the through-thickness stresses, are of primary importance. Typically, a 3-gauge strain rosette is used to determine the principal stresses on a shell surface. For ring-stiffened cylinders under hydrostatic pressure, the stress regime is largely bi-directional. This allows the use of two uni-axial gauges, aligned in the circumferential and axial directions, to measure strain.

The experimental stresses are calculated assuming that axial strains (ε_{axial}) and circumferential strains (ε_{circ}) are approximately equivalent to the first (ε_1) and second (ε_2) principal strains, respectively (i.e. assuming zero membrane shear strain). Similarly, axial stress (σ_{axial}) and circumferential stress (σ_{circ}) are assumed to be equivalent to the first (σ_1) and second (σ_2) principal stresses, respectively. The conversion from strain to stress was undertaken using the following expressions:

$$\sigma_{axial} = \sigma_1 = \frac{E}{1-v^2}\left(\varepsilon_{axial} + v\varepsilon_{circ}\right)$$

$$\sigma_{circ} = \sigma_2 = \frac{E}{1-v^2}\left(\varepsilon_{circ} + v\varepsilon_{axial}\right)$$

(7)

where E is Young's modulus and v is Poisson's ratio.

Shell yielding can be determined using any of several yield criteria. For this study, yield was defined by the instance of the von Mises equivalent stress reaching the 0.2% yield stress of the material. For two-dimensional shell problems, the von Mises equivalent stress, σ_{eqv}, reduces to the form in Equation (8).

$$\sigma_{eqv} = \sigma_6 = \sqrt{\sigma_1^2 + \sigma_2^2 - \sigma_1\sigma_2} \qquad (8)$$

Strain in the penetrations was monitored using strain gauge rosettes with a nominal rosette angle of 60° (Figure 23). Uni-axial rosette strains were converted to orthogonal strains using the following strain transformations:

$$\varepsilon_{circ} = \frac{2}{3}\left(\varepsilon_a - \frac{1}{2}\varepsilon_b + \varepsilon_c\right)$$

$$\varepsilon_{axial} = \varepsilon_b \qquad (9)$$

$$\gamma = \frac{2}{\sqrt{3}}\left(\varepsilon_a - \varepsilon_c\right)$$

where ε_{circ} and ε_{axial} refer to the hoop and longitudinal orthogonal strains in the penetrations, respectively, γ is the membrane shear strain, and ε_a, ε_b, and ε_c are the rosette strains as indicated in Figure 23. The principal strains can be derived from the rosette strains using Equation (10).

$$\varepsilon_{1,2} = \frac{\varepsilon_a + \varepsilon_b + \varepsilon_c}{3} \pm \frac{\sqrt{2}}{3}\sqrt{\left(\varepsilon_a - \varepsilon_b\right)^2 + \left(\varepsilon_a - \varepsilon_c\right)^2 + \left(\varepsilon_b - \varepsilon_c\right)^2} \qquad (10)$$

The principal rosette stresses are calculated using Equation (7), assuming the principal strains coincided with the orthogonal strains.
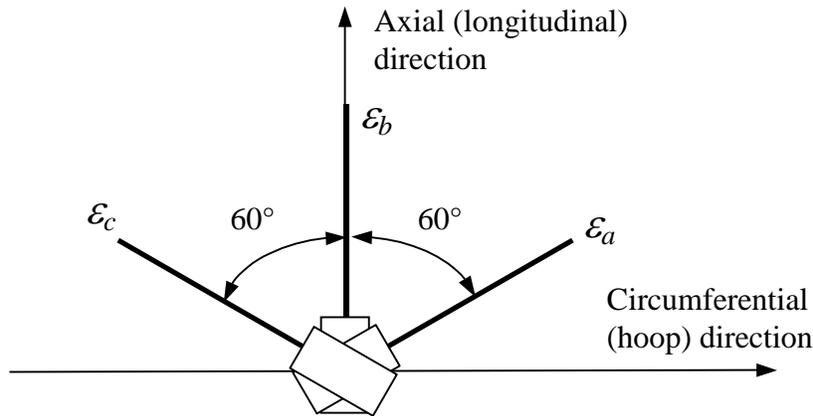
Figure 23. *Rosette strain configuration in the penetrations*

Identification of collapse shape

The shape or mode in which the structure fails can sometimes be determined using the data obtained from strain gauges (Table 19). Strictly speaking, the collapse mode is defined by displacements relative to the original geometry of the structure. The use

of displacement transducers or dial indicators in a high pressure testing tank is impractical, as the instruments would be required to operate under external pressure. In addition, mounting a sufficient number of displacement transducers to define the critical collapse mode would not be possible due to space constraints.

Table 19. Determining pressure hull collapse mode from strain data

CIRCUMFERENTIAL STRAIN CONDITION AT COLLAPSE[1]		IMPLIED COLLAPSE MODE
Stiffener flanges	*Shell at mid-bay*	
Uniform, plastic	Uniform, plastic	Global axisymmetric plastic collapse
Uniform, elastic	Uniform, plastic	Local axisymmetric plastic collapse
Uniform, elastic	Sinusoidal, elastic	Interframe elastic lobar buckling
Sinusoidal, elastic	Sinusoidal, elastic	Overall elastic lobar buckling
Uniform, elastic	(Partially) sinusoidal, plastic	Interframe elasto-plastic collapse
(Partially) sinusoidal, plastic	(Partially) sinusoidal, plastic	Overall elasto-plastic collapse

1. Compressive strains are assumed, however, strains can sometimes enter the tensile regime in the post-collapse region.

Strain gauges measure material deformation, and thus, indirectly, displacement of the structure. For example, strain gauges mounted about the pressure hull circumference, and aligned in that direction, that show uniform compressive strain at a given pressure, indicate a uniform compression of the cylinder, and thus a uniform radial contraction. Gauges that measure a sinusoidal variation in strain about the circumference indicate bending associated with the corresponding sinusoidal radial displacement of the pressure hull. Fourier analysis can be applied to the strain data, in a similar manner to which it is applied to the measurement of geometric imperfections in Section 2.3, to determine the relative contribution of each mode to the general collapse shape.

Table 19 summarizes circumferential strain conditions indicating a particular collapse mechanism and shape. This table is a general guideline and does not take into account the contribution of axial strains to collapse, the effect of structural damage, or collapse mechanisms that involve interaction between one or more of the basic modes listed in the table.

4. Experimental Results

The following sections present the experimental results, which consist of collapse pressures, strain data, and observed failure modes.

4.1 Short Cylinders

The collapse pressures of the undamaged cylinder without instrumentation (L300-No2) and the two cylinders with corrosion (L300-No3 and L300-No4) are summarized in Table 20. The average collapse pressure for the damaged cylinders was 6.86 MPa, with the instrumented cylinder (L300-No3) showing a collapse pressure 2.4% less than the corresponding specimen without gauges (L300-No4). Corrosion damage to the shell resulted in an average reduction in collapse pressure of 13% from the undamaged state.

Table 20. Experimental collapse pressures of short cylinders

CYLINDER	MEASURED MEAN SHELL THICKNESS		COLLAPSE PRESSURE (MPa)[1]
	UNDAMAGED REGION	CORRODED REGION	
L300-No2	2.496 mm	N/A	7.87
L300-No3	2.477 mm	1.870 mm	6.77
L300-No4	2.544 mm	1.904 mm	6.94

1. Collapse pressure corrected by subtracting initial pressure measurement, accurate to within ±0.04 MPa.

It was concluded, by post-test inspection, that each of the specimens failed in the predicted manner, i.e. a local failure at the shell in the central bay. The failure of the specimens was catastrophic in all cases, with the cylinders rupturing such that two main pieces remained. This can be seen in Figure 24, Figure 25, and Figure 26, which show specimens L300-No2, L300-No3, and L300-No4, respectively, after testing.

Lobar buckling was evident, especially in the central bays. Collapse was observed in an n=7 mode for the undamaged specimen, and an n=7 or n=8 mode for the specimens with corrosion. The catastrophic nature of the failures made it difficult to assess the failure modes with certainty. Rupture took place at the shell-stiffener interface in the central bays, as well as in an axial direction between buckling lobes.

The cylinders with simulated corrosion showed signs of localized buckling behaviour in the area of reduced shell thickness and the immediate surrounding shell (Figure 27). The buckle was formed by 1.5 sine waves in the circumferential direction, with a wavelength approximately equal to the width of the corrosion patch, and a half sine wave across the patch in the axial direction (Figure 28). Both cylinders with corro-

sion exhibited this local buckling of the thinned shell, which suggests that it was not an isolated random incident.

Figure 24. *Specimen L300-No2 after testing*

Figure 25. *Specimen L300-No3 after testing*

In the case of the instrumented cylinder with corrosion damage (L300-No3), the visual evidence of the failure mode was supported by the strain gauge data. Figure 29 and Figure 30 show the circumferential strain at the middle of the central bay on the outside and inside of the shell, respectively, versus the applied external pressure.

These graphs show a reduction in the stiffness of the shell around the area of the corrosion (0°), which exhibits nonlinear behaviour well before the rest of the structure.

Figure 26. *Specimen L300-No4 after testing*
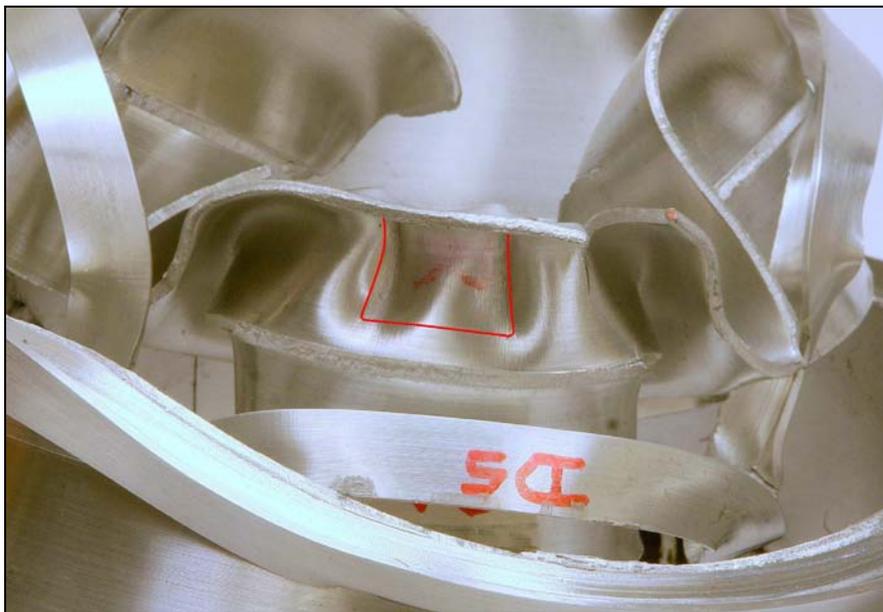
Figure 27. *Close-up of corroded region (highlighted in red) of L300-No4 after testing*

The von Mises stress has been calculated at locations where both circumferential and axial strains were available (see Section 3.4.2 for calculation of experimental stresses). The applied pressures causing the von Mises stress to initially reach the yield stress at these locations are summarized in Table 21. This data suggests that

yielding first occurred at the edges of the corrosion (10° and 350°), which is consistent with the bending caused by the reduced stiffness and eccentricity at the corrosion.
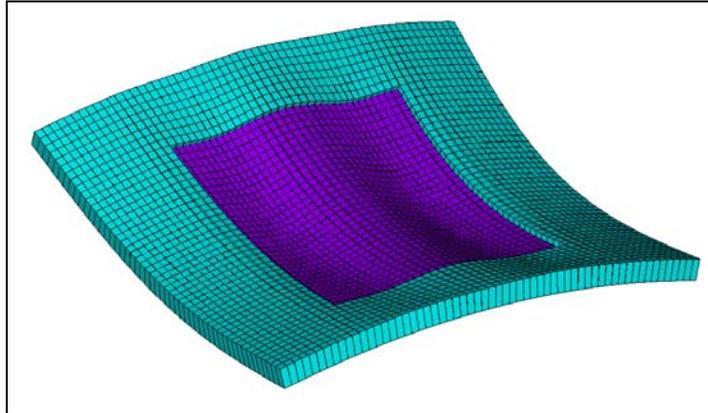
Figure 28. Schematic representation of local buckling in the corroded short cylinders

The shell at the centre of the corrosion was the next region to yield. Yielding occurred almost simultaneously on the inside and outside of the shell at an applied load of approximately 5 MPa. Figure 29 and Figure 30 show that a reversal in the direction of the circumferential strains at the corrosion takes place at an external pressure of approximately 5.5 MPa. Strain reversals at or near the corrosion were also observed in the axial strains in the middle of the central bay (Figure 41 and Figure 42 in Annex C) and the circumferential strains in the central bay adjacent to the stiffeners (Figure 45 and Figure 46 in Annex C).

Table 21. External pressure causing von Mises stress to reach yield (L300-No3)

LOCATION	YIELD PRESSURE (MPa)[1]
Outside shell, mid-bay in central bay, 0°	4.95
Outside shell, mid-bay in central bay, 90°	Did not yield
Outside shell, mid-bay in central bay, 180°	Did not yield
Outside shell, mid-bay in central bay, 270°	6.71
Inside shell, mid-bay in central bay, 0°	4.98
Inside shell, mid-bay in central bay, 10°	4.65
Inside shell, mid-bay in central bay, 45°	6.66
Inside shell, mid-bay in central bay, 350°	4.65

1. Yield pressure accurate to within ±0.04 MPa.

The corroded region was able to take an additional 0.5 MPa of external pressure after yield before these strain reversals occurred. This suggests that the strain reversals can be attributed to local buckling of the corroded region, initiated by material yielding. Ultimate collapse of the cylinder, which occurred at an external pressure of 6.77 MPa,

was immediately preceded by yielding of the shell in the undamaged regions (270° and 45°).
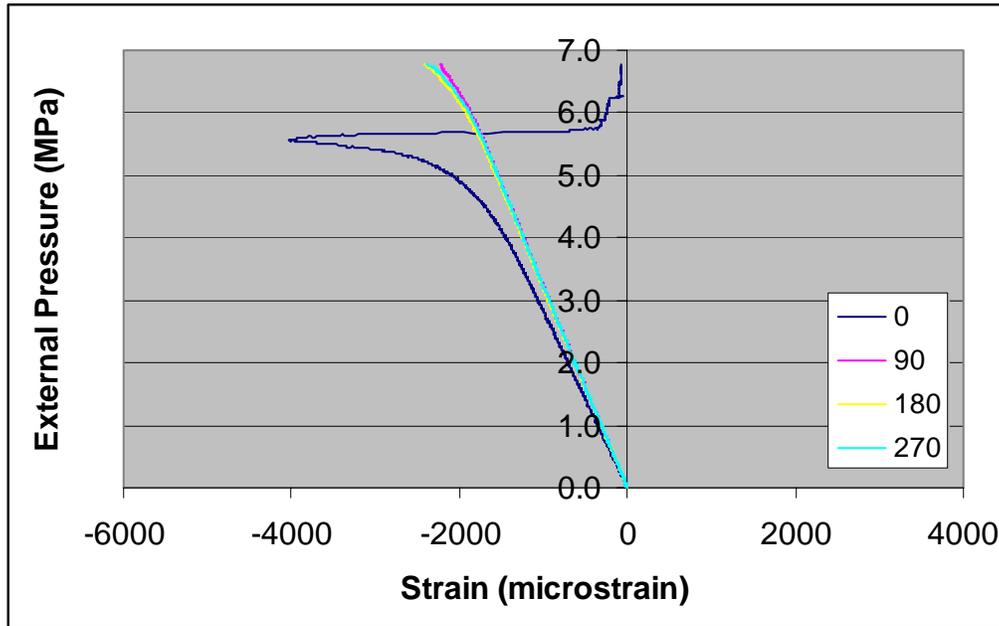
Figure 29. L300-No3 – circumferential strain on outside of shell at central bay (mid-bay)
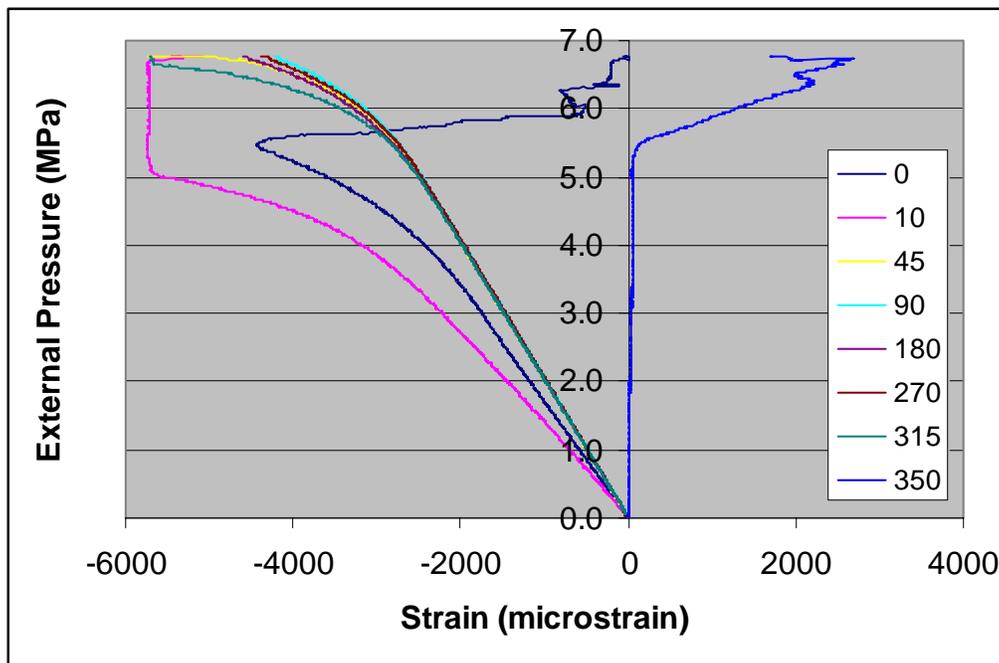
Figure 30. L300-No3 – circumferential strain on inside of shell at central bay (mid-bay)

The experimental strains and derived stresses suggest that the thin corroded region undergoes a local instability that does not immediately precipitate failure of the entire structure. Because rupture does not occur, the loss of load-carrying capacity in the buckled zone can be taken up by the surrounding shell and adjacent ring-stiffeners. This is supported by the circumferential strain data from the two central stiffeners (Figure 43 and Figure 44 on page 73 in Annex C), which show nonlinear increases in strain around an applied pressure of 5.5 MPa. After this disturbance, the strain behaviour of the ring-stiffeners becomes more-or-less linear again until immediately preceding collapse.

Load-strain curves for all strain gauges on the instrumented cylinder with corrosion damage (L300-No3) can be found in Annex C.

4.2 Long Cylinders

The collapse pressures of the undamaged cylinder with instrumentation (L510-No1) and the damaged cylinder without instrumentation (L510-No2) are summarized in Table 22. Corrosion damage to the central flanges resulted in a reduction in collapse pressure of 5% from the undamaged state.

Table 22. Experimental collapse pressures of long cylinders

CYLINDER	CORROSION	STRAIN GAUGES	COLLAPSE PRESSURE (MPa)
L510-No1	No	Yes	9.05
L510-No2	Flange 4 & 5, Dog-bone	No	8.59

1. Collapse pressure corrected by subtracting initial pressure measurement, accurate to within ±0.04 MPa.

The undamaged and instrumented cylinder (L510-No1) was tested in two stages as mentioned in Section 3.3. Figure 31 shows load-strain curves for the strain gauge located at 0° on stiffener #4, for both stages of testing. Yielding of the structure is indicated by the residual strain (approximately 100 microstrain) remaining after the aborted test. All of the strain gauges that were not damaged in the failure showed residual compressive strain ranging from 100 to 500 microstrain, indicating a significant portion of the specimen had yielded.

Load-strain curves for all strain gauges on the cylinder can be found in Annex D for the first trial (L510-No1A) and Annex E for the second trial (L510-No1B).

As with the short cylinders, the long cylinders failed catastrophically (Figure 32). Visual inspection suggested that the long cylinders failed in an overall collapse mode, however the exact mode shape was not discernable from the destroyed cylinders. Overall collapse was indicated by the deformed frames, which experienced similar displacements as the shell, and the global nature of the failure. The final deformed shape of both long cylinders can be roughly described as a half sine wave over the length of the cylinder, and apparently two waves about the circumference.
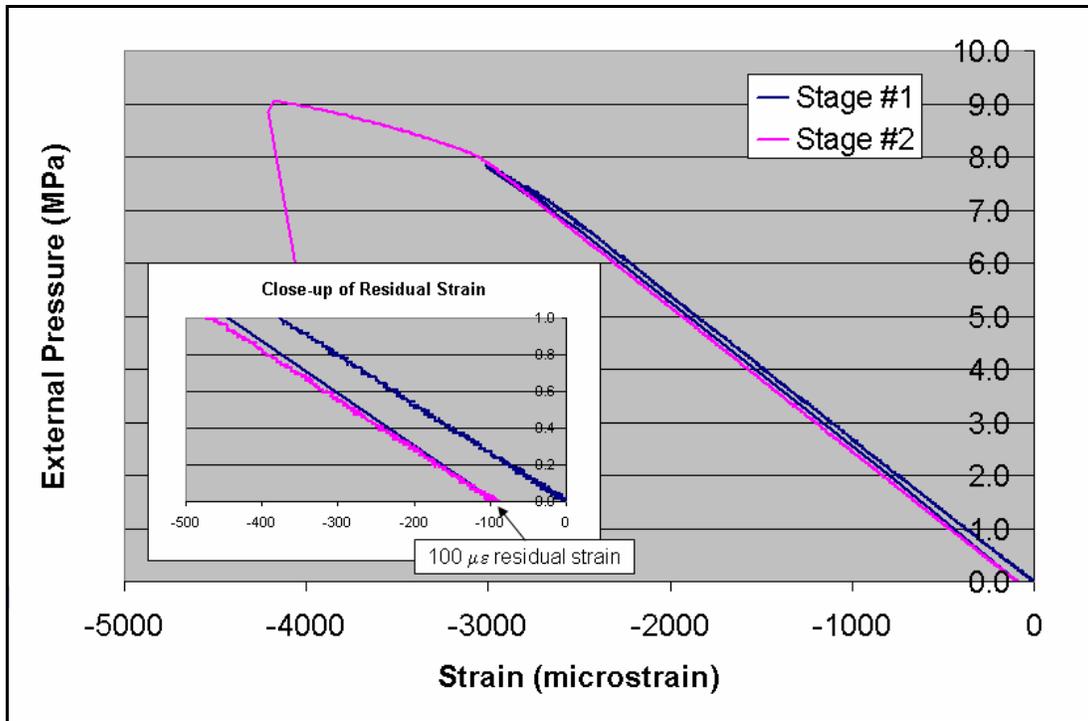
Figure 31. *L510-No1 – circumferential strain at 0° on stiffener #4*

The observed failure mode of the cylinders disagrees with the analytical design calculations, which predicted an overall collapse mode with three waves about the circumference (see Section 2.7). The analytical prediction of collapse mode is supported by the strain gauge data from the undamaged cylinder. Figure 33 shows the circumferential strain at various locations about the flange of frame #4 for selected values of applied external pressure. As the load increases, the displaced shape of the frame becomes increasingly of the form of three circumferential waves, and at the collapse pressure of 9.05 MPa the frame is distinctly in this mode. A similar mode was observed in frame #5 of this cylinder.

Figure 34 shows the circumferential strain in stiffener #4 of specimen L510-No1 at the peak load, as well as the first two data sets in the post-collapse region. It can be seen that the collapse shape is initially dominated by a three-wave mode, however, as collapse proceeds, the two-wave mode becomes increasingly significant.

The collapse shape was further quantified by undertaking Fourier analysis of the circumferential strain data for specimen L510-No1. It was necessary to linearly interpolate the strain data for circumferential angles of 90° and 150° as gauges at these points were damaged during the initial aborted test, and were not functional for the second test.

The results of the Fourier analysis of the strain data are presented in Table 23. At the collapse load, the circumferential strain in stiffener #4 is dominated by an $n=3$ mode, however, as collapse progresses the $n=2$ mode becomes more significant. Thus, the

final two-wave shape of the destroyed cylinders is likely a post-collapse development. The actual collapse shape appears to be dominated by an *n*=3 mode, which is in agreement with the analytical predictions.

Figure 32. *Specimens L510-No1 (left) and L510-No2 (right) after testing*

Although strain data is not available for the damaged long cylinder (L510-No2), the collapse shape and mechanism can be guessed at. Its final shape after testing was similar to that of the initially undamaged cylinder, which suggests that the collapse mode was also similar (i.e. *n*=3). The large inward buckle observed after testing is centred at the location of the 'dog-bone' corrosion on the stiffeners, and the stiffeners were torn at the corrosion. It seems that ultimate failure of the cylinder was initiated by yielding of the stiffener flanges at the corrosion.

The von Mises stresses calculated for the first stage of testing for the long undamaged cylinder (L510-No1A) indicate that the shell yielded at the inside of the central bay at 300°, at a pressure of 7.48 MPa. Yielding did not occur at any other strain gauge location during the first stage of testing. The specimen was nonetheless permanently deformed, as a permanent set was observed in all strain gauges. This indicates that yielding occurred at locations not monitored by strain gauges.

For a ring under axisymmetric compression, the ratio of circumferential strain on the extreme inner and outer fibres located at the shell plating and stiffener flange, respec-

tively, is equal to the ratio of outer to inner radius (1.12 for the long cylinder). Thus, a likely candidate for this yield location is the shell at the base of the stiffeners, which is under a greater axisymmetric stress than the stiffener flange in externally stiffened cylinders. This theory is supported by the analytical calculations (Section 2.7), which indicate that overall collapse will be initiated by yielding of the shell at the base of the stiffener (P_P) rather than yielding of the flange ($P_{y(n)}$).
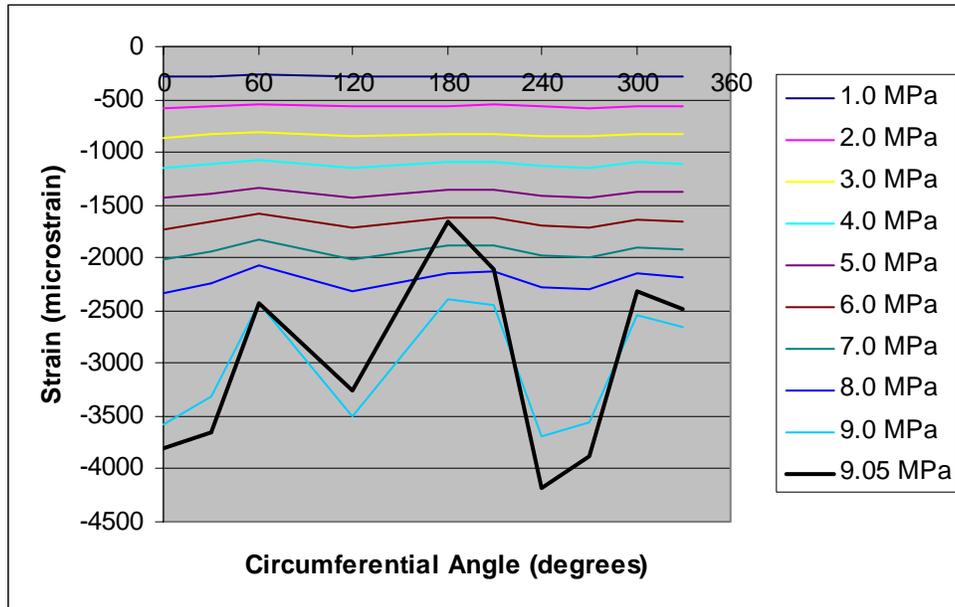
Figure 33. Circumferential strain in stiffener #4 of L510-No1 (up to collapse)
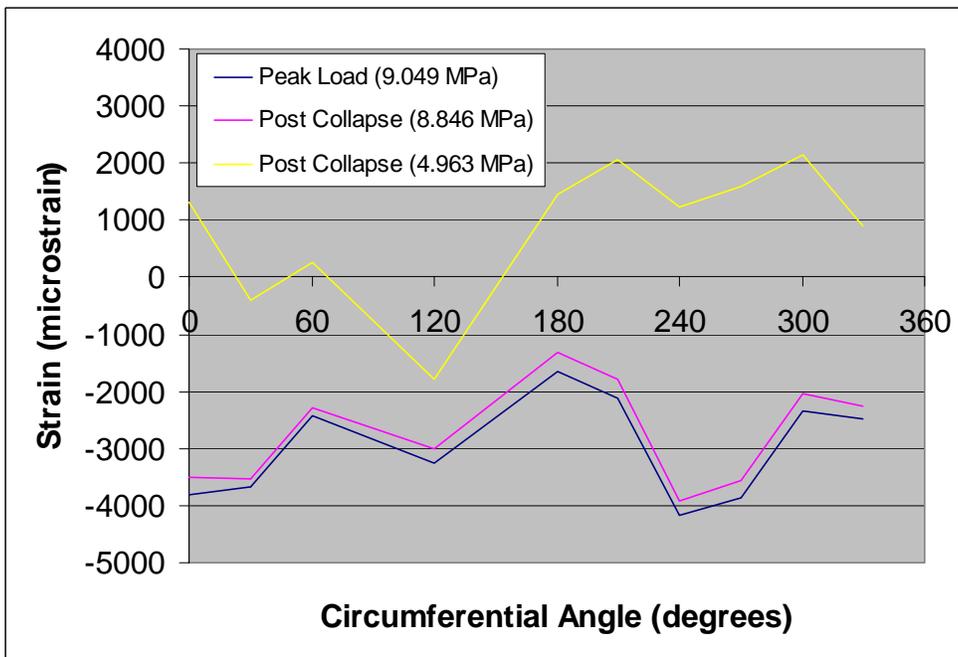
Figure 34. Circumferential strain in stiffener #4 of L510-No1 (post collapse)

Table 23. *Fourier analysis of collapse mode shape for L510-No1 (Stiffener #4)*

FOURIER COMPONENT (*n*)	FOURIER AMPLITUDE (microstrain) AT INDICATED PRESSURES[1]		
	9.05 MPa	*8.85 MPa*	*4.96 MPa*
2	428	465	473
3	906	903	552
4	123	101	245
5	120	142	423
6	35	22	233

1. The pressure values correspond with the collapse load (9.05 MPa) and the first two post-collapse pressures recorded.

The von Mises stresses at locations where both circumferential and axial strains are available have been calculated for the second stage of testing this specimen (L510-No1B). The external pressures associated with the von Mises stresses reaching yield are reported in Table 24. The shell at the central bay began to yield at an external pressure that was approximately 94% of the collapse pressure. The circumferential strains on the stiffener flanges and the axial strains in the end bays do not suggest that yield had occurred in these regions. Therefore, it is likely that overall collapse was precipitated by yielding of the shell plating, rather than yielding of the stiffener flanges. Again, this is supported by the analytical calculations.

Table 24. *External pressure causing von Mises stress to reach yield (L510-No1B)*

OUTSIDE SHELL	YIELD PRESSURE (MPa)	INSIDE SHELL	YIELD PRESSURE (MPa)[1]
Mid-bay in central bay, 0°	8.68	Mid-bay in central bay, 0°	Did not yield
Mid-bay in central bay, 60°	8.73	Mid-bay in central bay, 60°	8.75
Mid-bay in central bay, 120°	8.61	Mid-bay in central bay, 120°	8.81
Mid-bay in central bay, 180°	8.61	Mid-bay in central bay, 180°	8.61
Mid-bay in central bay, 240°	8.58	Mid-bay in central bay, 240°	N/A
Mid-bay in central bay, 300°	8.56	Mid-bay in central bay, 300°	8.66

1. Yield pressure accurate to within ±0.04 MPa.

4.3 Cylinder with Penetrations

The cylinder with penetrations underwent several loading cycles in the elastic range in the early 1990s, during a previous Canada-Netherlands collaborative project [3], but the load-strain data for these cycles are not included in this document. Imperfec-

tion measurements (OOC) from the centre stiffener taken before the initial elastic loads were applied closely resemble the measurements taken before the cylinder was tested destructively as part of the current project (Figure 35). This indicates that the initial load cycles were indeed in the elastic range.
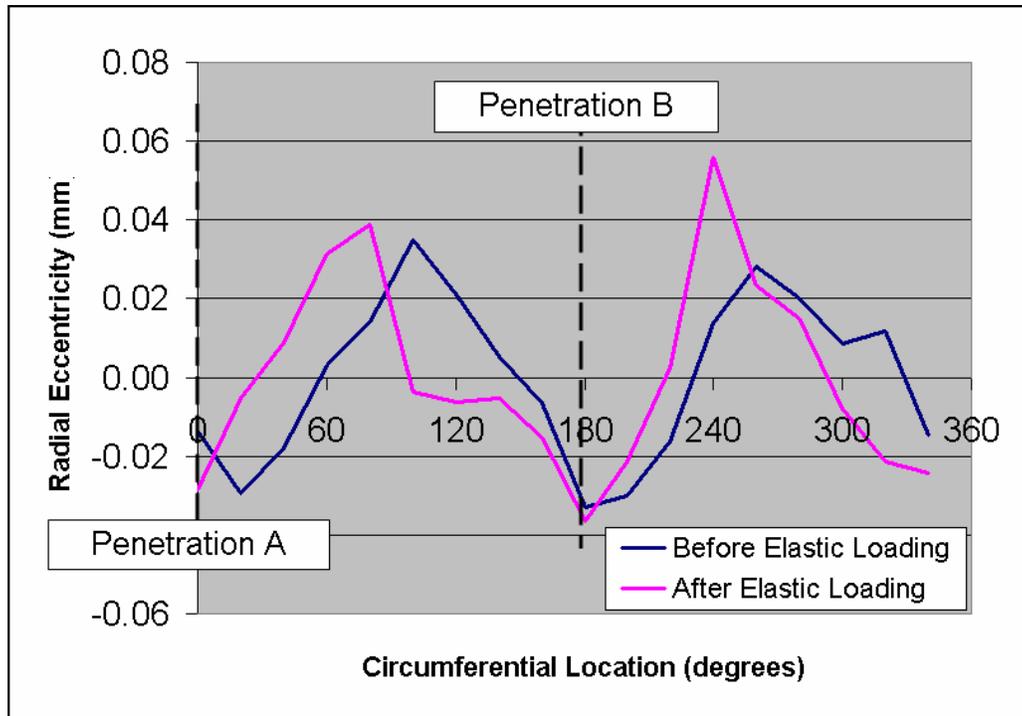
Figure 35. OOC of the cylinder with penetrations (S6) before and after elastic loading

The cylinder with penetrations withstood a maximum pressure of 9.00 MPa. Inspection of the cylinder after testing (Figure 36) initially suggested an *n*=2 overall collapse shape. However, an examination of the circumferential strains at the central stiffener strongly implied an overall *n*=3 mode shape (Figure 37). An additional inspection of the damaged specimen revealed that this was the case, as the apparent two-wave collapse mode was actually a three-wave mode with one of the waves torn away from the cylinder during rupture (the largest separate shell-stiffener section in Figure 36).

Figure 37 suggests that the *n*=3 collapse mode is oriented such that an outward lobe, corresponding to a local circumferential strain maximum, occurs at 0°, which is the location of penetration A. The circumferential location corresponding to penetration B (180°) coincides with an inward lobe. The position of the buckling lobes with respect to the penetrations was further corroborated by post-test inspection, as well as the strain data from the stiffeners immediately adjacent to the penetrations.

Figure 38 plots the circumferential strain on stiffeners immediately adjacent to the penetrations (±15° from the centre of the penetrations). The strain gauges near penetration A show strain reversal as the collapse load is approached, which is consistent with an outward buckling lobe (i.e. the strains become less compressive due to the negative bending). Conversely, the strains near penetration B show a nonlinear

growth in compressive strain as collapse approaches, suggesting an inward buckling lobe.

Figure 36. Cylinder with penetrations after testing
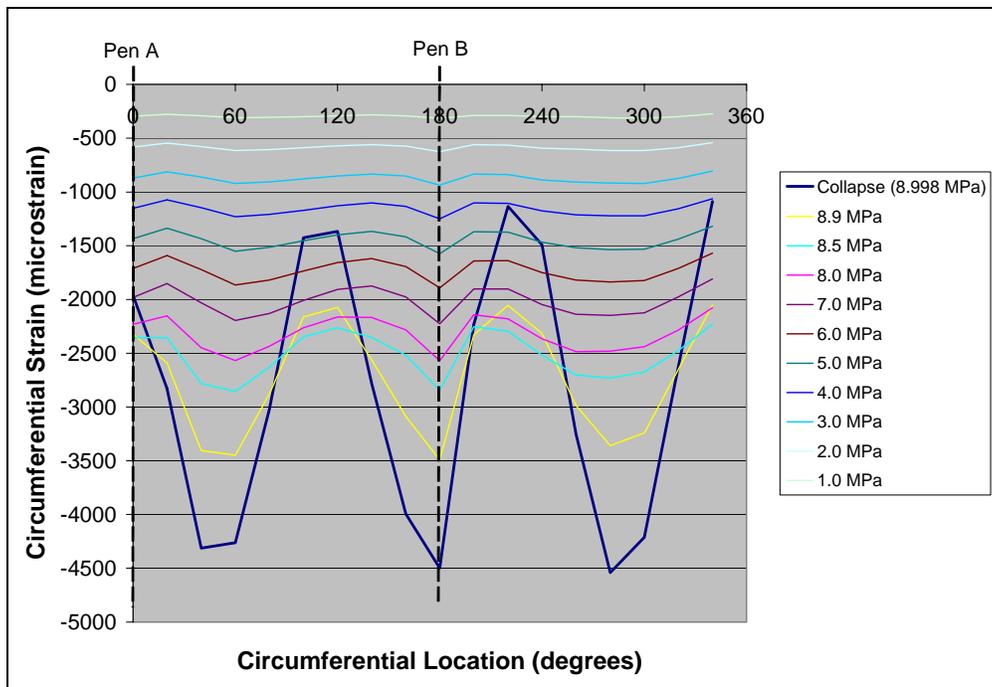
Figure 37. Cylinder with penetrations – circumferential strains at centre stiffener
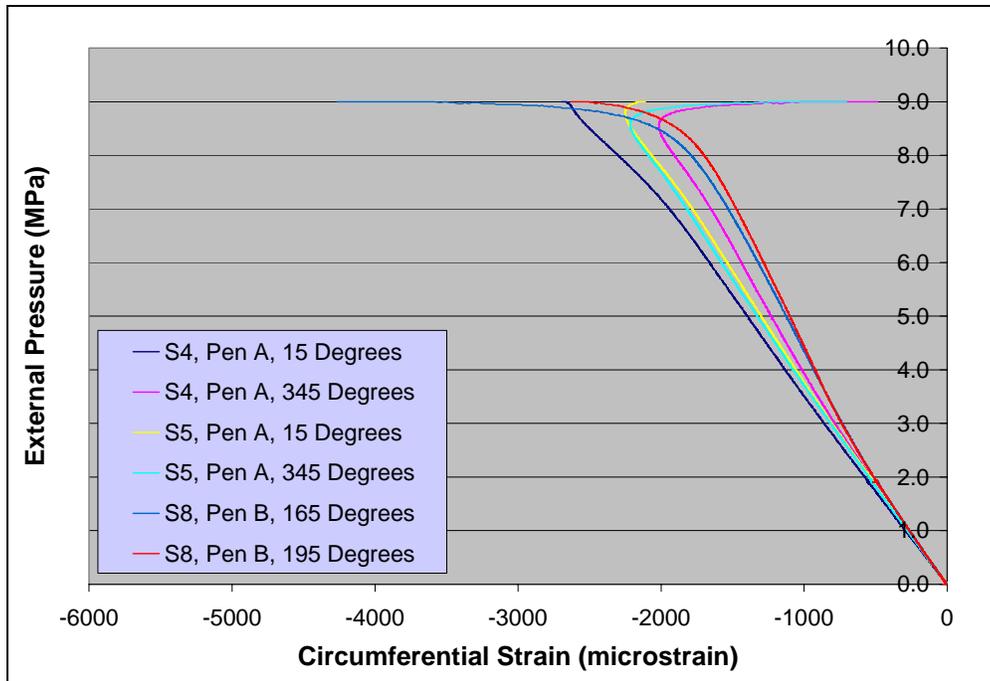
Figure 38. *Cylinder with penetrations – circumferential strain adjacent to penetrations*

Strains within the penetrations themselves were monitored using strain rosettes. The raw strain data from the rosettes were converted to orthogonal and principal strains (see Section 3.4.2 for methodology). The orthogonal strains in penetration A are plotted against the applied pressure in Figure 39.

The penetrations were subjected to compressive forces transferred from the cylinder in both the circumferential and axial directions. The circumferential (or hoop) stress of a cylinder under uniform external pressure is theoretically greater than the axial stress. This is supported by Figure 39, which shows that the hoop strains about the circumference of penetration A are compressive, and that the compressive strain is greatest at 0°, where the gauge is aligned with the circumferential force transferred from the cylinder.

Figure 39 also shows that the vertical (or axial) strains in penetration A are tensile, which is consistent with the longitudinal bending induced by the squeezing effect of the membrane forces transferred from the cylinder and the resistance of the thick base of the penetration.

Analysis of the rosette strains showed that yielding (von Mises criteria with yield stress of 250 MPa) of the penetrations occurred at pressures as low as 46% of the collapse pressure (Table 25). Yielding of the central stiffener and associated shell plating did not occur until just prior to collapse, after the *n*=3 overall collapse mode was already well formed. The yield data, in addition to the obvious alignment of the collapse mode with the penetrations, suggests that geometric eccentricity due to the

penetrations leading to yielding of the central stiffener, was primarily responsible for initiating collapse.

Additional load-strain curves for the penetration model can be found in Annex F.
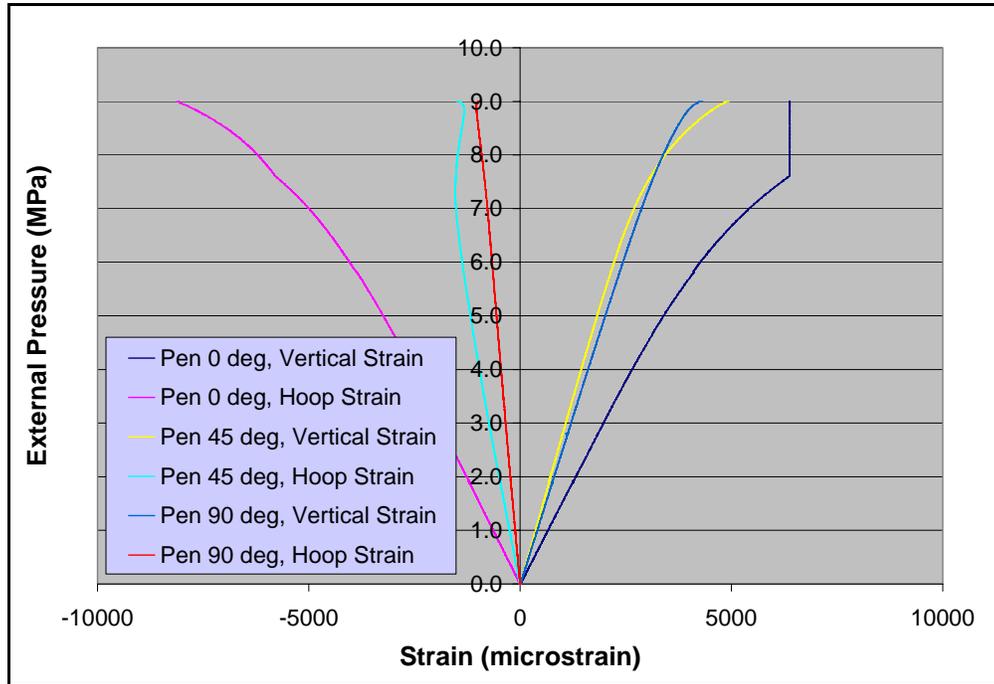
Figure 39. *Cylinder with penetrations – orthogonal strains at penetration A*

Table 25. *Yield pressure (von Mises criteria) for the cylinder with Penetrations*

LOCATION	YIELD PRESSURE (MPa)[1]
Penetration A, 0°	4.12
Penetration A, 45°	7.93
Penetration A, 90°	8.29
Penetration B, 0°	5.23
Penetration B, 45°	N/A
Penetration B, 90°	N/A

1. Yield pressure accurate to within ±0.04 MPa.

5. Discussion

5.1 Experimental Strain Error

Strain gauge information must be interpreted with care. There are several sources of possible experimental strain error, which can be due to mechanical issues, such as inadequate adhesion of the gauges to the base material, or electronic issues, such as noise in the data acquisition system.

In the present study, the data acquisition system supplied an input excitation voltage to the strain gauges based on a strain range of either ±6000 or ±5000 microstrain, depending on the specimen. These ranges limit the output voltage, and thus the recorded strain. This limitation is evident in load-strain curves that show no increase in strain with applied pressure after ±6000 or ±5000 microstrain (e.g. the gauge at $10°$ in Figure 30 on page 41).

Load-strain curves may show a relatively large degree of noise, which is typically associated with either a small strain range (e.g. Figure 47 on page 75) or incorrect amplification gain that was corrected after testing (e.g. the gauge at $300°$ in Figure 48 on page 75). Finally, strain gauge data may show unexpected or erratic behaviour (e.g. rosette strains for penetration B of the cylinder with penetrations, pages 84 to 86), which may be attributed to de-bonding of the gauges or electronic problems.

5.2 Comparison with Analytical Calculations

5.2.1 Collapse Pressure and Mode

Table 26 shows a comparison of the SDF predictions for collapse pressure and mode with those observed during the experiments. The analytical collapse prediction for each cylinder was taken to be the lower of the mean empirical interframe collapse pressure, $P_{ci(mean)}$, and the elasto-plastic overall collapse pressure, P_{co} (see Table 16 and Table 17). The mode shapes reported for interframe calculations are those associated with the elastic buckling pressure, P_{m1}.

In general, the SDF show poor correlation with the experimental collapse pressures, except for the long T-section stiffened cylinders. They were able to predict whether interframe or overall collapse would occur however, for all but one specimen (L510-No1).

The overall elasto-plastic collapse pressure predicted for L510-No1 showed the best correlation with the experimental collapse pressure.

The interframe collapse pressures of the short cylinders were consistently underestimated for two main reasons: 1) the empirical-based analytical collapse pressure is for

cylinders with up to 0.5% OOC and residual stresses due to fabrication, and 2) the analytical predictions for the short corroded cylinders pessimistically assumed a uniform shell reduction, rather than the finite region of corrosion as in the experimental specimens.

Table 26. Comparison of SDF collapse predictions with experimental results

SPECIMEN	SDF PREDICTION		EXPERIMENTAL RESULT	
	Collapse Mode	*Collapse Pressure (MPa)*	*Collapse Mode*	*Collapse Pressure (MPa)*
L300-No2	Interframe (n = 9)	6.68	Interframe (n = 7)	7.87
L300-No3	Interframe (n = 10)	4.28	Interframe (n = 7 or 8)	6.77
L300-No4	Interframe (n = 10)	4.28	Interframe (n = 7 or 8)	6.94
L510-No1	Interframe (n = 8)	8.24	Overall (n = 3)	9.05
	Overall (n = 3)	9.13		
L510-No2	Overall (n = 3)	8.32	Overall (n = 2 or 3)	8.59
Cylinder with penetrations	Overall (n = 3)	7.11	Overall (n = 3)	9.00

The overall collapse pressures predicted by the SDF were relatively accurate. The analytical predictions were within approximately ±3% of the experimental collapse pressures for the T-section stiffened cylinders. Overall collapse was under-predicted by 21% for the cylinder with penetrations, possibly because the cylinder was analyzed as if no penetrations were present. The SDF successfully predicted an n=3 collapse shape for the long T-section stiffened cylinders and the cylinder with penetrations.

5.2.2 Elastic Stresses

Both axial and circumferential strain data were available for most shell locations, and thus bi-axial stresses were calculated. The stress at the stiffeners was assumed to be uni-axial in the circumferential direction. Stress values at the mid-plane of the shell were determined by averaging the inside and outside strains and then converting to stress.

The predicted and measured stresses (see Table 15 for descriptions) for an applied external pressure of 1 MPa are summarized in Table 27. Values are reported for specimens and locations where strain gauge data were available.

The long undamaged cylinder and the cylinder with penetrations showed good correlation between the predicted and measured stresses, with the SDF predicting the appropriate stresses within ±10%. The SDF were able to predict the circumferential stress in the stiffener flange to within ±16% for all instrumented specimens.

The short corroded cylinder generally showed poor correlation between the calculated and measured stresses, with the SDF over-predicting stress by as much as 70%. This discrepancy is likely due to the local corrosion damage in the specimen, which is analyzed as if it is uniformly distributed about the circumference for the purposes of the SDF calculations. Comparison of the stresses in the undamaged region of the shell to calculations based on the design shell thickness (2.5mm) yielded slightly better correlation (45%).

Table 27. Comparison of SDF stress predictions with experimental results

SPECIMEN	SDF PREDICTION[1] (MPa)				EXPERIMENTAL RESULT[2] (MPa)			
	σ_3	σ_5	σ_6	σ_f	σ_3	σ_5	σ_6	σ_f
L300-No3 (at corrosion)	61.7	56.7	49.2	21.8	36.2	39.2	38.7	18.8
L300-No3 (undamaged areas)	44.0	40.6	35.2	20.1	30.4	N/A	N/A	17.6
L510-No1	36.4	34.8	30.1	22.3	33.8	32.6	28.6	20.3
Cylinder with penetrations	36.6	34.2	29.8	22.2	N/A	N/A	N/A	20.8

1. SDF prediction of indicated stress at an applied pressure of 1 MPa, taken as the yield stress divided by the corresponding yield pressure.

2. Experimental value of the indicated stress, calculated as described in Section 3.4.2, uses the average strain about the circumference for undamaged cylinders and regions, and the strain at the corrosion for damaged specimens.

In general, the analytical values of stress were greater than the experimental values for all but one instance for the available locations. In the long cylinder, this can be partially attributed to the location of the gauges in relation to the midpoint of the bay of shell plating. Bi-axial gauges were not used, and thus the axial and circumferential strains used to calculate the design stresses were not taken at exactly the same location. In the long cylinder, both the axial and circumferential gauges were offset from the centre of the bay, which would be expected to result in lower strains than if they were located at mid-bay.

In the short cylinder, the axial and circumferential gauges were both located at mid-bay, but were offset slightly from each other in the circumferential direction. This would be expected to have less influence on the calculated stresses, especially in the undamaged region.

The discrepancy between the design and measured stresses may also arise from incorrect material properties used in calculating these stresses. Young's modulus may be assumed to be reasonably correct, as it was measured directly from tensile coupon tests. However, an assumed value of Poisson's ratio (0.3) was used throughout the design and experimental calculations. Increasing Poisson's ratio to 0.35 improves correlation of the design and measured stresses for the long cylinder (7%), and for the short cylinder at the corrosion and in the undamaged regions (60% and 37%, respectively).

The circumferential stress in the shell at mid-bay is generally greater on the outside of the shell than at mid-plane. This is confirmed by the SDF calculations, as well as by the measured stress in the long cylinders. The short corroded cylinder, however, shows the inverse effect (i.e. the mid-plane shell stress is greater than the stress on the outside of the shell). The measured stress field suggests a slight bending of the corroded shell in the outward radial direction. This is supported by the observed local buckling pattern, which has an outward buckle in the centre of the patch (see Figure 28).

5.3   Effect of Corrosion Damage

The experimental results described in this report are the first stage of a larger program to assess the effects of corrosion, geometric imperfections, and residual stresses on the structural behaviour of pressure hulls. The small amount of data regarding the effect of corrosion damage available does not allow any definite conclusions to be drawn, but a few observations can be made.

5.3.1 Short Cylinders

A 25% reduction in shell thickness implies a corresponding 36% decrease in the inter-frame collapse pressure according to the analytical calculations (Section 2.7). However, the corroded short cylinders showed an average collapse pressure that was only 13% lower than the companion undamaged experimental specimen. The damaged experimental specimens both showed local buckling at the corrosion that, in the instrumented specimen L300-No3, occurred at a pressure approximately 30% less than the collapse load of the undamaged cylinder L300-No2. The cylinder shell was not ruptured and the load was redistributed to the undamaged regions of the specimen, which were able to resist additional applied pressure until yielding of the shell in the undamaged regions resulted in ultimate failure.

5.3.2 Long Cylinders

The long cylinder with damaged stiffener flanges was not instrumented with strain gauges, so a well-supported theory for its lower strength compared with the undamaged long cylinder cannot be postulated. Theoretical models indicate that overall collapse is initiated by yielding of the stiffener flange or the shell at the base of the web. The strain gauge data indicate that the latter case is likely to be the immediate cause of failure in the undamaged long cylinder, as the circumferential strains in the shell are greater than the corresponding flange strains. It may be reasonably assumed that the locally reduced flange width in the damaged cylinder led to increased strains in either or both the stiffener and shell, and to premature material yielding and the associated loss of stiffness resulting in collapse. This is further supported by the location of the buckling failure, which was centred on the stiffener corrosion.

As expected, the SDF predicted a greater than realized reduction in overall collapse pressure (9% for the SDF versus 5% for the experiments). The analytical calculations

modeled the reduction in flange breadth uniformly about the circumference and over the cylinder length, which likely accounts for the greater part of the discrepancy between predicted and experimental collapse pressures.

5.4   Effect of Penetrations

The collapse pressure of the cylinder with penetrations was approximately 9.0 MPa, which is significantly greater than any of its companion specimens tested as part of a previous project [3]. The previously tested specimens were nominally identical to the cylinder with penetrations, except for the absence of penetrations and the presence of either mechanically induced OOC imperfections (and thus residual stresses) or simulated decks or tank-tops (one with and one without OOC). Unfortunately, no 'plain' cylinder without OOC was tested to provide a baseline strength value to compare with the deck and penetration models.

The three cylinders with OOC and no decks failed in overall modes (n=3) at an average collapse pressure of 6.62 MPa. The specimens with simulated decks, with and without OOC, failed in overall collapse modes at pressures of 6.68 and 7.88 MPa, respectively.

The decks were found to induce buckling in a preferred circumferential mode that is in harmony with the location of the deck intersection on the cylinder shell [3]. The decks did not appear to significantly strengthen the cylinders, however, as the cylinder with OOC and a deck had a collapse pressure only marginally greater than the average value of the specimens without decks.

Penetrations were found to have a similar influence on the orientation of the buckling mode, if not the buckling shape as well. It seems, however, that penetrations are less detrimental to pressure hull strength than decks, as indicated by the greater collapse pressure for the penetration model (9.0 MPa) as compared to the cylinder with a deck and no OOC (7.9 MPa). This is likely attributable to the eccentricity-inducing effect of a stiff deck (i.e. effectively an out-of-circularity), which is uniform along the length of the cylinder, whereas the eccentricity caused by the penetrations is local rather than global.

Without a companion 'plain' cylinder for comparison, it is not possible to state whether the penetrations had a positive or negative effect on the collapse pressure. It is apparent that of all the strength-reducing factors studied for the rectangular section ring-stiffened specimens, including OOC and decks, the penetrations were the least detrimental.

5.5   Evaluation of the Experimental Apparatus

As noted, collapse occurred catastrophically for all specimens tested in Phase 1. The damage to the specimens was so severe that the collapse mode could not be determined visually with any degree of certainty (see Figure 24, Figure 32, and Figure 36).

It is desirable to limit the post-collapse displacements of the cylinder specimens in order to get a better understanding of the collapse shape.

The catastrophic failures can be attributed to the large amount of strain energy built up in the system (testing apparatus and specimen) during loading, and then released at collapse. The contribution of the various components to the stored energy, as well as possible remedies, is discussed in the following sections.

5.5.1 Strain Energy in the Experimental Apparatus

Tank pressure is created by pumping water into the test chamber. This causes the chamber to expand elastically and the testing fluid to compress elastically, resulting in an external pressure on the test specimen. The strain energy stored in the testing apparatus can be estimated by calculating the stretching of the pressure tank and the compression of the testing fluid as pressure is applied to the specimen. The strain energy of the tank structure at a specified applied pressure can be taken as

$$\int \frac{1}{2} E \varepsilon^2 dV_t \tag{11}$$

where ε is estimated as a uniform hoop strain and V_t is the volume of the tank material (axial strain energy is neglected). The strain energy of an idealized test cylinder without stiffeners can be calculated in a similar manner.

The strain energy of the testing fluid can be taken as

$$\frac{1}{2} \beta \varepsilon_f{}^2 V_f \tag{12}$$

where β is the bulk modulus of the testing fluid, ε_f is the compression of the fluid per unit original volume, and V_f is the volume of testing fluid at the pressure load under consideration.

The strain energies of the various components were calculated based on an applied pressure of 10 MPa, a pressure tank filled with 1/3 mineral oil and 2/3 water, and an aluminium test cylinder with the following dimensions: 510 mm long, 110 mm inner radius, and 4.5 mm wall thickness. The strain energy of the testing fluid (40 kJ) was found to be an order of magnitude greater than the energy stored in the pressure tank (2.4 kJ), and two orders of magnitude greater than the energy stored in the specimen (470 J).

An additional location of stored strain energy is the pressurizing pump and associated piping. This would be difficult to quantify and was ignored for the purposes of this study.

5.5.2 Improved Experimental Apparatus

The following sections describe solutions, varying in complexity, practicality and effectiveness, to the problem of excessively catastrophic specimen failures.

Modified pressure chamber

The testing fluid has been found to be the greatest contributor to the total strain energy built up during testing. Thus, the stored energy could be reduced by the use of a smaller test chamber, which would require a smaller volume of testing fluid. If the structure was sufficiently stiff, the smaller volume of fluid required would result in less stored energy to be violently released during collapse. This would, however, require the construction of new pressure chamber, which would be costly.

Solid specimen core

More feasible solutions will result from focusing on reducing or controlling the post-collapse displacements of the specimens. In previous experimental studies, the collapse shape of a specimen was preserved by inserting a hardwood core in the cylinder [3]. This allowed a specimen to collapse, but prevented the stored energy from completely destroying it. This method has some disadvantages; namely the possibility of damaging internal instrumentation and the fact that it is a passive system, i.e. it does nothing to control post-collapse displacements and velocities, but merely sets a maximum threshold for displacement.

Fluid-filled specimen with passive control

An alternative to using a solid core is to fill a specimen with fluid, which would be vented to the outside of the pressure chamber. A pressure-resistant tube or pipe would allow the internal fluid to escape from the specimen to the outside of the test chamber as the external pressure is applied causing the specimen to contract. The connection could be terminated in a Venturi valve. This type of valve has a conical restriction that allows fluid to pass at low rates of flow (i.e. low velocities), but the hydrodynamic effects are such that at high velocities the flow is significantly reduced. Internal pressure would have to be monitored, especially during the post-collapse period when the Venturi valve reduces the flow.

Fluid-filled specimen with active control

A better solution is to actively control the pressure applied to a specimen by controlling the volume of fluid inside it. This can be accomplished by venting a fluid-filled specimen, using a system of valves that controls fluid flow from the inside of a specimen. A schematic diagram of this system is shown in Figure 40.

The testing of a specimen would be undertaken in the following steps:

1. Fill the specimen with fluid and connect to the system (Figure 40).

2. Close the release valve (Valve A) and open the cross-over valve (Valve B), and pressurize the system to a load beyond the anticipated collapse value. This will result in a pressure differential between the inside and outside of the specimen of zero (i.e. a net load of zero on the specimen).

3. Close the cross-over valve and use the release valve to slowly release the fluid from the cylinder while monitoring the pressure differential and strains. The flow, and therefore the applied load, can be reduced or stopped altogether when approaching collapse, as indicated by the strain behaviour.

This method has another benefit in that the pump doesn't have to be used after step 2. This eliminates the electronic noise associated with the operation of the pump.
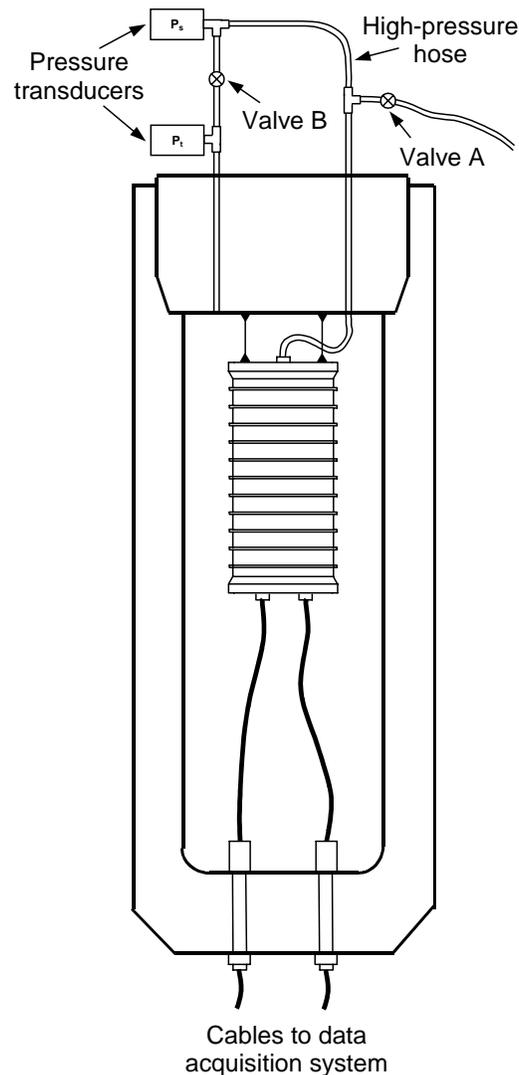
Figure 40. Schematic drawing of improved pressure testing apparatus

6.   Summary, Recommendations and Future Work

Six ring-stiffened cylinder specimens have been loaded to failure under hydrostatic pressure. Five of these pressure hull structures had simulated corrosion scarring on the shell or stiffeners, and one specimen had reinforced hull penetrations. The observed failure mode of the specimens generally agreed with the design predictions. Analytical collapse pressure predictions were poor for the short specimens and the cylinder with penetrations, but agreed well with experiment for the long cylinders.

Material loss due to simulated corrosion was found to reduce the collapse strength of pressure hulls compared to undamaged companion specimens. The strength-reducing effect has been primarily attributed to the premature onset of yield due to reduced stiffness at the corroded structure. Eccentricity due to one-sided thinning may also be a factor, especially in cases of shell corrosion.

An isolated patch of relatively severe corrosion thinning (25% of the nominal shell thickness) was found to reduce the ultimate strength of the cylinder by approximately 13%. A local instability also occurred at the corrosion at a pressure that was 30% less than the undamaged collapse pressure. This local buckling was apparently triggered by yielding of the thinned shell, which would have to be taken into account when assessing the working pressure of the cylinder. Yielding of a pressure hull during normal operations is not acceptable, as it could lead to an accumulation of permanent deformation over repeated loadings and ultimately to premature failure. Thus, the working pressure of the cylinder would be based on the 30% pressure reduction to initial instability rather than the 13% reduction in ultimate strength.

The experimental data currently available is not sufficient to propose a direct relationship between corrosion levels and structural deterioration. This will be more practical when further tests have been performed. Numerical analyses (nonlinear finite element analyses), which have been performed for Phase 1 specimens by TNO of the Netherlands [12] and will be carried out for all future cylinders, will provide validation of the analysis method. Further numerical investigation of corrosion damage to pressure hull structures not covered in this study will allow a full range of corrosion scenarios to be studied.

Phase 2 of this testing program will include the specimens that were not tested in Phase 1 (L300-No1 and L510-No3). These specimens will be instrumented with strain gauges, and therefore provide added insight into the collapse mechanism of the undamaged short cylinders and long cylinders with 'dog-bone' corrosion.

Four new cylinders with internal T-section ring-stiffeners have been fabricated for Phase 2 testing, with the goal of investigating the effects of the shell corrosion on overall collapse. One of these long cylinders is nominally perfect, and the remaining three specimens have various levels of corrosion on the outside of the shell.

All future specimens will be instrumented, as strain gauges have been found to be valuable for interpreting failure modes and comparing with analytical methods. For duplicate specimens, a minimal level of instrumentation can be used, concentrating on the region of failure, as observed in companion specimens. Bi-axial strain gauges or rosettes, rather than a pair of uni-axial gauges, should be used at locations where both axial and circumferential strains are required.

Material property tests for new specimens should be performed to measure Poisson's ratio, in addition to Young's modulus and yield stress. This will allow design and experimental stresses to be calculated with greater certainty.

The highly destructive collapse mechanisms that have been observed in the testing of Phase 1 specimens has been attributed to the release, upon failure, of the energy stored in both the specimen and the testing apparatus. It is not desirable to alter the fabricated shape of the specimens to lessen this effect, so the solution must involve an alteration to the experimental apparatus and/or procedure. A complete reconstruction of the testing equipment is not practical, and thus, several methods of altering the existing apparatus have been explored. It was decided that future pressure testing should use the active control system as described in Section 5.5.2. This solution was chosen because it is relatively simple and economical to implement, and it allows some control of the pre- and post-collapse displacements.

7. References

1. MacKay, J.R., Smith, M.J., and Pegg, N.G. (2006). *Design of pressure hulls using nonlinear finite element analysis*. Proceedings of OMAE2006. June 4-9, 2006, Hamburg, Germany.

2. Department of National Defence (1980). *Canada – Netherlands Information Exchange Project between the Department of National Defence of Canada and the Netherlands Ministry of Defence Pertaining to the Design of Surface Ships and Submarines*. 10984, Department of National Defence, Canada.

3. Pegg, N.G., Bosman, T.N., and Keuning, P.J. (1994). Summary Report of the Canada/Netherlands Project on Determination of Overall Collapse of Imperfect Pressure Hull Components. (DREA Report 94/101). Defence Research Establishment Atlantic.

4. Defence Procurement Agency (2001). *SSP 74 Design of Submarine Structures*. Sea Systems Publication No. 74, Defence Procurement Agency, Sea Technology Group, United Kingdom.

5. Kendrick, S. (1985). Ring-Stiffened Cylinders Under External Pressure. In R. Narayanan, (Ed.), *Shell Structures, Stability and Strength*, pp. 57-95. Elsevier Publishers.

6. Faulkner, D. (1977). *Effects of residual stresses on the ductile strength of plane welded grillages and of ring stiffened cylinders*. Journal of Strain Analysis. 12(2). 130-139.

7. Schmidt, H. (2000). *Stability of steel shell structures: General report*. Journal of Construction Steel Research. 55. 159-181.

8. Kendrick, S.B. (1977). *Shape imperfections in cylinders and spheres: their importance in design and methods of measurement*. Journal of Strain Analysis. 12(2). 117-122.

9. MatWeb. (Copyright 1996-2006). MatWeb – Online Material Database Aluminium 6082-T6. (Online) Automation Creations, Inc. http://www.matweb.com/ (12 Dec. 2006).

10. British Standards Institution (1980). *BS 5500 British Standard Specification for Unfired Fusion Welded Pressure Vessels, Issue 5*. British Standards Institution, United Kingdom.

11. Smith, M.J. and MacKay, J.R. (2005). *Overall elasto-plastic collapse of ring stiffened cylinders with corrosion damage*. RINA Transactions 2005 Part A1 – International Journal of Maritime Engineering.

12. The Netherlands Organisation for Applied Scientific Research TNO. (2005). Unpublished results.

Annex A: Measured Radii

Table 28. Measured radii (mm) for indicated locations (L300-No2)

θ (deg)	R1	R2	R3	R4	R5	R6 (In)	R6 (Out)	R7	R8	R9	R10	R11
0	124.947	112.465	124.451	112.431	124.439	109.969	112.431	124.440	112.417	124.432	112.421	124.900
10	124.971	112.481	124.472	112.461	124.455	109.991	112.442	124.450	112.441	124.449	112.427	124.913
20	124.994	112.511	124.496	112.488	124.478	110.015	112.461	124.470	112.461	124.467	112.444	124.932
30	125.014	112.537	124.516	112.518	124.501	110.039	112.485	124.489	112.479	124.483	112.463	124.949
40	125.016	112.550	124.530	112.533	124.519	110.059	112.509	124.506	112.490	124.496	112.481	124.964
50	125.020	112.555	124.534	112.549	124.531	110.068	112.531	124.524	112.502	124.514	112.493	124.968
60	125.013	112.547	124.539	112.554	124.534	110.072	112.544	124.538	112.517	124.539	112.501	124.970
70	125.004	112.525	124.524	112.550	124.531	110.062	112.548	124.542	112.527	124.526	112.504	124.976
80	124.995	112.508	124.517	112.531	124.527	110.046	112.543	124.539	112.530	124.532	112.512	124.987
90	124.985	112.515	124.510	112.510	124.512	110.022	112.524	124.528	112.525	124.531	112.518	125.001
100	124.979	112.513	124.499	112.489	124.500	109.997	112.503	124.512	112.514	124.529	112.519	125.017
110	124.973	112.501	124.491	112.480	124.487	109.973	112.488	124.506	112.499	124.522	112.515	125.028
120	124.973	112.489	124.482	112.478	124.482	109.951	112.477	124.488	112.489	124.512	112.515	125.038
130	124.975	112.485	124.479	112.482	124.480	109.943	112.468	124.485	112.483	124.510	112.509	125.040
140	124.976	112.487	124.481	112.481	124.487	109.941	112.471	124.491	112.489	124.506	112.510	125.042
150	124.987	112.490	124.488	112.486	124.489	109.948	112.483	124.495	112.490	124.514	112.509	125.036
160	124.998	112.511	124.502	112.493	124.503	109.965	112.504	124.513	112.505	124.520	112.513	125.019
170	125.010	112.529	124.524	112.509	124.516	109.983	112.533	124.524	112.517	124.530	112.514	125.003
180	125.021	112.544	124.538	112.534	124.536	110.004	112.545	124.542	112.521	124.532	112.517	124.979
190	125.034	112.563	124.567	112.551	124.547	110.004	112.558	124.552	112.533	124.538	112.514	124.962
200	125.042	112.569	124.560	112.562	124.558	110.031	112.565	124.560	112.538	124.540	112.513	124.953
210	125.048	112.596	124.566	112.567	124.559	110.040	112.561	124.570	112.552	124.543	112.512	124.963
220	125.047	112.580	124.566	112.566	124.557	110.041	112.558	124.553	112.545	124.543	112.512	124.985
230	125.052	112.578	124.560	112.563	124.555	110.036	112.555	124.547	112.541	124.541	112.521	125.014
240	125.036	112.563	124.547	112.549	124.537	110.037	112.541	124.541	112.523	124.536	112.523	125.039
250	125.022	112.545	124.532	112.540	124.525	110.031	112.530	124.527	112.514	124.531	112.524	125.056
260	125.006	112.521	124.514	112.520	124.513	110.029	112.518	124.516	112.506	124.529	112.522	125.061
270	124.980	112.491	124.492	112.497	124.493	110.024	112.508	124.510	112.505	124.522	112.515	125.048
280	124.959	112.460	124.470	112.476	124.475	110.016	112.496	124.503	112.501	124.517	112.501	125.024
290	124.938	112.447	124.451	112.453	124.458	110.005	112.481	124.490	112.496	124.514	112.486	124.989
300	124.918	112.434	124.438	112.438	124.450	109.989	112.466	124.472	112.481	124.494	112.471	124.963
310	124.903	112.426	124.427	112.432	124.433	109.974	112.446	124.462	112.465	124.472	112.458	124.947
320	124.896	112.421	124.418	112.427	124.424	109.958	112.431	124.449	112.446	124.448	112.444	124.933
330	124.894	112.427	124.418	112.416	124.422	109.951	112.417	124.432	112.423	124.435	112.429	124.917
340	124.906	112.431	124.423	112.413	124.422	109.950	112.415	124.427	112.407	124.421	112.417	124.898
350	124.927	112.444	124.431	112.413	124.427	109.959	112.424	124.428	112.407	124.428	112.446	124.898

Table 29. Measured radii (mm) for indicated locations (L300-No3)

θ (deg)	R1	R2	R3	R4	R5	R6 (In)	R6 (Out)	R7	R8	R9	R10	R11
0	124.953	112.491	124.475	112.467	124.477	110.000	111.869	124.467	112.443	124.456	112.450	124.911
10	124.953	112.495	124.473	112.471	124.474	110.002	112.489	124.468	112.447	124.452	112.441	124.893
20	124.961	112.496	124.475	112.479	124.468	109.997	112.477	124.469	112.459	124.451	112.438	124.890
30	124.963	112.493	124.476	112.478	124.461	109.998	112.459	124.466	112.468	124.452	112.443	124.898
40	124.962	112.492	124.471	112.468	124.455	109.991	112.444	124.458	112.463	124.457	112.452	124.912
50	124.971	112.495	124.471	112.465	124.452	109.984	112.444	124.451	112.450	124.457	112.465	124.934
60	124.970	112.495	124.474	112.463	124.449	109.986	112.441	124.442	112.429	124.457	112.465	124.951
70	124.969	112.492	124.472	112.466	124.449	109.983	112.441	124.444	112.419	124.455	112.463	124.969
80	124.965	112.483	124.471	112.471	124.453	109.985	112.447	124.450	112.431	124.460	112.466	124.980
90	124.964	112.471	124.470	112.472	124.461	109.990	112.460	124.462	112.453	124.470	112.473	124.983
100	124.957	112.468	124.464	112.471	124.468	109.994	112.481	124.476	112.477	124.481	112.486	124.978
110	124.954	112.469	124.465	112.469	124.473	109.997	112.498	124.485	112.495	124.486	112.490	124.971
120	124.949	112.474	124.466	112.465	124.473	109.998	112.497	124.486	112.495	124.485	112.486	124.959
130	124.946	112.475	124.468	112.466	124.469	109.993	112.484	124.481	112.485	124.475	112.475	124.943
140	124.945	112.474	124.470	112.467	124.464	109.985	112.462	124.468	112.463	124.460	112.460	124.926
150	124.950	112.467	124.470	112.465	124.457	109.977	112.444	124.456	112.442	124.451	112.451	124.910
160	124.961	112.466	124.475	112.463	124.455	109.972	112.435	124.443	112.422	124.441	112.450	124.906
170	124.970	112.471	124.474	112.455	124.454	109.969	112.434	124.441	112.417	124.438	112.442	124.904
180	124.988	112.482	124.481	112.457	124.457	109.973	112.443	124.443	112.419	124.437	112.435	124.914
190	124.995	112.490	124.479	112.460	124.459	109.978	112.452	124.447	112.428	124.440	112.440	124.925
200	124.996	112.494	124.482	112.463	124.464	109.983	112.460	124.455	112.438	124.448	112.449	124.941
210	124.991	112.495	124.486	112.466	124.469	109.991	112.465	124.466	112.447	124.461	112.466	124.960
220	124.984	112.493	124.486	112.471	124.472	109.993	112.469	124.475	112.457	124.471	112.482	124.976
230	124.975	112.491	124.490	112.481	124.478	109.994	112.477	124.485	112.473	124.481	112.490	124.985
240	124.958	112.478	124.487	112.485	124.477	109.993	112.478	124.488	112.483	124.489	112.489	124.990
250	124.951	112.466	124.486	112.487	124.480	109.989	112.480	124.488	112.487	124.490	112.490	124.988
260	124.946	112.460	124.480	112.487	124.481	109.986	112.478	124.485	112.479	124.494	112.493	124.984
270	124.949	112.461	124.474	112.476	124.477	109.981	112.475	124.479	112.470	124.492	112.495	124.983
280	124.949	112.462	124.469	112.463	124.473	109.979	112.470	124.476	112.462	124.489	112.485	124.982
290	124.954	112.472	124.463	112.449	124.466	109.980	112.468	124.471	112.460	124.484	112.477	124.980
300	124.953	112.479	124.463	112.441	124.460	109.979	112.462	124.474	112.464	124.484	112.479	124.980
310	124.957	112.475	124.466	112.450	124.456	109.982	112.455	124.472	112.474	124.483	112.490	124.986
320	124.958	112.468	124.472	112.469	124.458	109.979	112.445	124.467	112.474	124.484	112.492	124.987
330	124.959	112.462	124.473	112.479	124.460	109.983	112.442	124.467	112.474	124.481	112.488	124.979
340	124.956	112.468	124.476	112.481	124.470	109.986	112.459	124.466	112.465	124.472	112.480	124.964
350	124.954	112.475	124.472	112.472	124.474	109.989	112.477	124.467	112.455	124.466	112.464	124.935

Table 30. *Measured radii (mm) for indicated locations (L300-No4)*

θ (deg)	R1	R2	R3	R4	R5	R6 (In)	R6 (Out)	R7	R8	R9	R10	R11
0	124.912	112.451	124.448	112.477	124.458	109.951	111.854	124.467	112.501	124.480	112.513	124.973
10	124.918	112.468	124.451	112.468	124.461	109.960	112.476	124.467	112.491	124.471	112.507	124.954
20	124.933	112.478	124.455	112.466	124.470	109.964	112.487	124.463	112.477	124.467	112.494	124.936
30	124.955	112.492	124.475	112.471	124.471	109.970	112.492	124.468	112.471	124.458	112.482	124.926
40	124.973	112.503	124.480	112.486	124.479	109.978	112.485	124.471	112.480	124.461	112.480	124.922
50	124.996	112.521	124.500	112.507	124.484	109.980	112.484	124.479	112.498	124.463	112.490	124.933
60	125.011	112.535	124.509	112.518	124.499	109.991	112.494	124.486	112.506	124.475	112.503	124.941
70	125.029	112.551	124.529	112.537	124.514	109.994	112.523	124.496	112.507	124.482	112.516	124.956
80	125.031	112.562	124.537	112.556	124.532	110.009	112.545	124.506	112.511	124.492	112.518	124.956
90	125.031	112.563	124.549	112.569	124.542	110.016	112.562	124.517	112.518	124.498	112.512	124.958
100	125.025	112.565	124.547	112.576	124.547	110.019	112.577	124.531	112.537	124.502	112.509	124.949
110	125.017	112.555	124.544	112.573	124.548	110.018	112.580	124.538	112.562	124.514	112.521	124.950
120	125.009	112.542	124.534	112.561	124.540	110.006	112.574	124.540	112.575	124.521	112.542	124.960
130	125.002	112.535	124.522	112.539	124.530	109.989	112.557	124.528	112.570	124.525	112.560	124.976
140	124.989	112.526	124.505	112.517	124.510	109.967	112.536	124.517	112.549	124.519	112.566	124.991
150	124.983	112.519	124.495	112.501	124.494	109.941	112.514	124.497	112.525	124.506	112.548	124.999
160	124.976	112.509	124.486	112.491	124.480	109.921	112.494	124.482	112.502	124.490	112.527	125.003
170	124.977	112.513	124.490	112.488	124.476	109.911	112.482	124.476	112.485	124.477	112.511	125.004
180	124.976	112.513	124.489	112.493	124.479	109.911	112.480	124.472	112.489	124.479	112.513	125.010
190	124.981	112.520	124.493	112.498	124.484	109.914	112.485	124.483	112.497	124.484	112.525	125.012
200	124.980	112.529	124.501	112.505	124.505	109.947	112.504	124.493	112.514	124.504	112.544	125.017
210	124.990	112.536	124.509	112.527	124.517	109.975	112.532	124.517	112.534	124.517	112.554	125.010
220	124.991	112.545	124.522	112.550	124.539	110.004	112.555	124.532	112.558	124.534	112.565	125.004
230	125.005	112.567	124.537	112.573	124.552	110.024	112.573	124.556	112.585	124.545	112.580	125.001
240	125.005	112.575	124.547	112.579	124.562	110.037	112.587	124.563	112.591	124.551	112.578	124.998
250	125.013	112.575	124.550	112.585	124.559	110.039	112.591	124.565	112.593	124.546	112.570	124.995
260	125.014	112.563	124.545	112.582	124.555	110.031	112.581	124.554	112.579	124.536	112.559	124.983
270	125.017	112.551	124.543	112.570	124.543	110.015	112.557	124.536	112.554	124.522	112.543	124.979
280	125.017	112.547	124.528	112.547	124.526	109.993	112.536	124.514	112.526	124.503	112.523	124.966
290	125.013	112.544	124.519	112.527	124.512	109.977	112.517	124.492	112.502	124.487	112.508	124.962
300	125.001	112.531	124.502	112.506	124.493	109.962	112.503	124.479	112.481	124.471	112.492	124.958
310	124.982	112.521	124.482	112.490	124.480	109.953	112.495	124.469	112.477	124.465	112.489	124.956
320	124.958	112.503	124.469	112.475	124.468	109.947	112.487	124.468	112.481	124.458	112.494	124.964
330	124.939	112.481	124.455	112.473	124.462	109.948	112.479	124.465	112.491	124.467	112.502	124.971
340	124.921	112.459	124.450	112.476	124.456	109.950	112.470	124.470	112.499	124.474	112.510	124.981
350	124.913	112.447	124.447	112.483	124.455	109.948	112.465	124.470	112.504	124.479	112.514	124.983

**Table 31.** Measured radii (mm) for indicated locations (L510-No1)

θ (deg)	R1	R2	R3	R4	R5	R6	R7	R8	R9	R10 (in)
0	125.040	113.024	123.025	112.994	122.996	112.991	122.992	112.985	122.987	109.966
10	125.079	113.042	123.038	113.001	123.003	112.992	122.988	112.980	122.986	109.959
20	125.109	113.065	123.060	113.017	123.010	112.996	122.992	112.986	122.986	109.946
30	125.116	113.078	123.077	113.033	123.024	113.008	123.006	112.994	122.998	109.949
40	125.106	113.086	123.089	113.050	123.041	113.025	123.018	113.011	123.012	109.960
50	125.075	113.084	123.088	113.061	123.049	113.044	123.045	113.033	123.036	109.963
60	125.041	113.072	123.085	113.065	123.061	113.062	123.059	113.058	123.053	109.977
70	124.994	113.050	123.069	113.062	123.065	113.072	123.077	113.072	123.070	109.979
80	124.952	113.030	123.052	113.051	123.061	113.076	123.082	113.080	123.077	109.990
90	124.918	113.010	123.032	113.038	123.048	113.069	123.080	113.076	123.080	109.998
100	124.893	112.988	123.011	113.017	123.037	113.052	123.066	113.064	123.073	110.001
110	124.883	112.969	122.990	113.000	123.016	113.031	123.051	113.049	123.065	110.004
120	124.894	112.955	122.975	112.981	122.999	113.006	123.027	113.032	123.048	110.003
130	124.918	112.951	122.971	112.972	122.985	112.991	123.007	113.014	123.034	109.990
140	124.949	112.961	122.977	112.972	122.981	112.982	122.995	112.999	123.018	109.984
150	124.985	112.985	122.995	112.979	122.982	112.980	122.987	112.987	123.003	109.971
160	125.023	113.018	123.022	112.999	122.995	112.989	122.988	112.985	122.989	109.952
170	125.064	113.046	123.050	113.025	123.009	113.003	122.995	112.989	122.983	109.938
180	125.098	113.070	123.080	113.047	123.028	113.012	123.003	112.991	122.975	109.940
190	125.122	113.093	123.099	113.067	123.040	113.024	123.006	112.990	122.972	109.926
200	125.132	113.103	123.109	113.077	123.051	113.029	123.007	112.989	122.971	109.910
210	125.128	113.098	123.106	113.072	123.047	113.027	123.004	112.986	122.972	109.901
220	125.104	113.078	123.086	113.056	123.034	113.015	122.994	112.983	122.975	109.895
230	125.061	113.045	123.056	113.030	123.017	112.998	122.988	112.975	122.977	109.891
240	125.009	113.006	123.018	112.992	122.993	112.979	122.980	112.980	122.979	109.899
250	124.961	112.969	122.982	112.960	122.968	112.964	122.976	112.978	122.984	109.903
260	124.918	112.936	122.953	112.933	122.950	112.953	122.973	112.978	122.987	109.920
270	124.878	112.914	122.932	112.918	122.945	112.956	122.978	112.981	122.993	109.934
280	124.848	112.901	122.924	112.915	122.944	112.961	122.978	112.984	123.002	109.952
290	124.830	112.900	122.927	112.925	122.951	112.969	122.980	112.987	123.009	109.973
300	124.826	112.908	122.937	112.937	122.963	112.978	122.987	112.991	123.013	109.982
310	124.837	112.928	122.951	112.951	122.967	112.981	122.992	112.999	123.016	109.996
320	124.867	112.949	122.968	112.966	122.975	112.982	122.994	113.006	123.011	109.996
330	124.903	112.963	122.984	112.976	122.981	112.987	122.999	113.005	123.009	109.993
340	124.944	112.980	122.996	112.981	122.987	112.989	122.997	112.995	123.000	109.986
350	124.993	112.999	123.008	112.987	122.989	112.990	122.993	112.988	122.992	109.980

Table 31. Continued

n	R10 (Out)	R11	R12	R13	R14	R15	R16	R17	R18	R19
0	112.983	122.992	112.981	122.987	112.989	122.992	113.011	123.020	113.040	124.938
10	112.983	122.987	112.978	122.986	112.995	122.998	113.011	123.025	113.049	124.923
20	112.991	122.993	112.984	122.996	113.012	123.010	113.017	123.027	113.045	124.913
30	113.000	123.000	112.996	123.009	113.017	123.021	113.022	123.035	113.050	124.911
40	113.020	123.016	113.018	123.027	113.036	123.032	113.034	123.043	113.051	124.912
50	113.033	123.037	113.040	123.047	113.047	123.044	113.040	123.052	113.059	124.923
60	113.056	123.056	113.058	123.062	113.060	123.053	113.055	123.061	113.058	124.935
70	113.074	123.073	113.071	123.073	113.068	123.062	113.058	123.062	113.056	124.951
80	113.084	123.083	113.078	123.077	113.072	123.064	113.061	123.059	113.054	124.973
90	113.091	123.087	113.082	123.080	113.076	123.062	113.057	123.051	113.039	124.996
100	113.084	123.085	113.079	123.077	113.070	123.057	113.047	123.048	113.032	125.001
110	113.067	123.075	113.067	123.067	113.063	123.048	113.042	123.044	113.040	125.024
120	113.054	123.060	113.052	123.054	113.052	123.038	113.037	123.038	113.032	125.042
130	113.035	123.043	113.034	123.037	113.027	123.025	113.031	123.024	113.022	125.056
140	113.020	123.023	113.017	123.018	113.014	123.014	113.018	123.007	112.998	125.060
150	112.998	123.005	112.998	122.999	112.997	122.996	112.994	122.984	112.973	125.061
160	112.981	122.986	112.981	122.986	112.980	122.976	112.971	122.959	112.951	125.055
170	112.972	122.974	112.965	122.969	112.965	122.954	112.944	122.947	112.939	125.042
180	112.970	122.966	112.954	122.957	112.951	122.935	112.929	122.933	112.930	125.048
190	112.961	122.959	112.944	122.943	112.933	122.924	112.925	122.930	112.935	125.015
200	112.964	122.955	112.940	122.937	112.930	122.920	112.928	122.932	112.935	124.999
210	112.965	122.955	112.936	122.938	112.925	122.921	112.928	122.932	112.932	124.983
220	112.967	122.957	112.935	122.943	112.927	122.927	112.936	122.930	112.930	124.970
230	112.969	122.962	112.943	122.948	112.935	122.936	112.940	122.932	112.931	124.969
240	112.971	122.971	112.955	122.963	112.947	122.946	112.941	122.936	112.933	124.976
250	112.976	122.983	112.967	122.975	112.968	122.956	112.952	122.943	112.942	124.988
260	112.988	122.992	112.984	122.992	112.985	122.972	112.964	122.960	112.961	125.002
270	112.996	123.008	112.997	123.006	112.999	122.988	112.981	122.978	112.977	125.020
280	113.011	123.019	113.015	123.021	113.015	123.001	113.001	122.996	112.991	124.985
290	113.020	123.029	113.023	123.030	113.026	123.013	113.010	123.009	113.002	124.988
300	113.025	123.030	113.029	123.035	113.034	123.016	113.021	123.020	113.010	124.984
310	113.029	123.032	113.032	123.034	113.034	123.016	113.019	123.016	113.017	124.974
320	113.022	123.023	113.023	123.030	113.029	123.010	113.018	123.016	113.014	124.959
330	113.014	123.015	113.010	123.018	113.018	123.006	113.007	123.012	113.016	124.940
340	113.006	123.007	113.001	123.007	113.006	122.996	113.002	123.012	113.017	124.920
350	112.993	122.996	112.990	122.994	112.995	122.990	113.003	123.011	113.030	124.904

Table 32. *Measured radii (mm) for indicated locations (L510-No2)*

θ (deg)	R1	R2	R3	R4	R5	R6	R7	R8	R9	R10 (in)
0	125.009	113.026	123.002	113.017	122.993	113.016	122.994	113.003	122.996	110.041
10	125.059	113.035	123.003	113.006	122.980	112.992	122.974	112.975	122.971	110.016
20	125.095	113.045	123.004	112.997	122.970	112.974	122.958	112.959	122.955	110.002
30	125.110	113.051	123.008	112.994	122.965	112.968	122.954	112.951	122.949	109.983
40	125.102	113.053	123.010	112.995	122.968	112.970	122.960	112.955	122.951	109.985
50	125.074	113.051	123.013	113.005	122.981	112.987	122.973	112.969	122.961	109.981
60	125.031	113.049	123.016	113.021	123.000	113.008	122.990	112.990	122.977	110.003
70	124.985	113.046	123.019	113.038	123.015	113.028	123.007	113.007	122.993	110.016
80	124.942	113.041	123.019	113.046	123.024	113.042	123.018	113.022	123.010	110.029
90	124.908	113.029	123.011	113.044	123.024	113.046	123.025	113.035	123.022	110.038
100	124.886	113.012	122.997	113.032	123.015	113.042	123.026	113.044	123.032	110.058
110	124.879	112.993	122.979	113.014	123.000	113.032	123.023	113.047	123.038	110.073
120	124.889	112.979	122.962	112.995	122.985	113.021	123.019	113.043	123.038	110.073
130	124.912	112.974	122.954	112.983	122.978	113.017	123.015	113.036	123.040	110.078
140	124.940	112.981	122.957	112.982	122.979	113.015	123.013	113.032	123.037	110.076
150	124.960	112.992	122.970	112.994	122.987	113.018	123.015	113.031	123.034	110.065
160	124.973	113.007	122.989	113.014	122.998	113.024	123.018	113.030	123.030	110.049
170	124.985	113.024	123.011	113.031	123.011	113.031	123.023	113.032	123.025	110.051
180	124.999	113.036	123.027	113.044	123.020	113.038	123.039	113.029	123.017	110.037
190	125.014	113.051	123.040	113.049	123.026	113.039	123.020	113.020	123.006	110.044
200	125.032	113.061	123.049	113.052	123.029	113.038	123.012	113.010	122.997	110.027
210	125.044	113.064	123.059	113.054	123.023	113.034	123.002	112.997	122.986	110.022
220	125.047	113.053	123.042	113.040	123.011	113.029	122.990	112.986	122.978	110.006
230	125.045	113.036	123.024	113.027	122.996	113.000	122.979	112.979	122.969	110.000
240	125.036	113.019	123.006	113.008	122.978	112.985	122.969	112.973	122.965	109.993
250	125.028	113.003	122.987	112.988	122.960	112.975	122.964	112.971	122.965	110.001
260	125.012	112.988	122.965	112.969	122.951	112.972	122.962	112.972	122.969	110.010
270	124.988	112.972	122.950	112.961	122.949	112.976	122.970	112.980	122.980	110.024
280	124.952	112.960	122.941	112.961	122.954	112.986	122.982	112.994	122.995	110.044
290	124.910	112.954	122.941	112.970	122.966	113.003	122.997	113.011	123.014	110.065
300	124.872	112.956	122.948	112.987	122.983	113.020	123.011	113.030	123.030	110.086
310	124.851	112.967	122.961	113.007	123.000	113.033	123.025	113.046	123.044	110.088
320	124.851	112.985	122.979	113.026	123.011	113.044	123.035	113.060	123.048	110.087
330	124.868	113.001	122.992	113.037	123.015	113.049	123.037	113.061	123.046	110.078
340	124.902	113.009	123.000	113.036	123.012	113.047	123.031	113.049	123.033	110.076
350	124.950	113.015	123.001	113.027	123.004	113.037	123.015	113.030	123.014	110.055

Table 32. *Continued*

θ (deg)	R10 (Out)	R11	R12	R13	R14	R15	R16	R17	R18	R19
0	112.996	122.987	112.979	122.990	112.975	122.995	112.986	123.014	113.032	125.004
10	112.971	122.967	112.960	122.975	112.962	122.987	112.972	123.005	113.026	124.994
20	112.955	122.956	112.948	122.970	112.952	122.980	112.964	122.997	113.015	124.987
30	112.946	122.949	112.945	122.967	112.946	122.980	112.960	122.993	113.007	124.979
40	112.949	122.952	112.945	122.966	112.946	122.983	112.962	122.992	113.005	124.976
50	112.960	122.961	112.954	122.975	112.955	122.991	112.969	122.995	113.007	124.977
60	112.977	122.975	112.967	122.987	112.967	122.999	112.973	123.003	113.011	124.982
70	112.997	122.991	112.983	123.002	112.981	123.009	112.983	123.010	113.015	124.989
80	113.016	123.008	113.001	123.018	112.996	123.021	112.998	123.018	113.020	125.001
90	113.033	123.024	113.021	123.035	113.012	123.034	113.010	123.030	113.031	125.016
100	113.045	123.039	113.037	123.049	113.028	123.045	113.023	123.044	113.051	125.029
110	113.052	123.050	113.050	123.060	113.042	123.055	113.034	123.057	113.070	125.039
120	113.056	123.056	113.056	123.065	113.049	123.062	113.047	123.066	113.077	125.041
130	113.057	123.055	113.056	123.065	113.047	123.067	113.056	123.068	113.072	125.040
140	113.053	123.051	113.050	123.063	113.043	123.067	113.056	123.065	113.069	125.040
150	113.046	123.042	113.039	123.051	113.038	123.062	113.045	123.055	113.060	125.031
160	113.037	123.032	113.025	123.043	113.029	123.050	113.028	123.040	113.047	125.020
170	113.029	123.020	113.014	123.033	113.017	123.033	113.013	123.026	113.031	125.009
180	113.018	123.011	113.006	123.024	112.999	123.018	112.994	123.011	113.014	124.999
190	113.005	123.003	112.998	123.011	112.981	123.002	112.978	123.004	113.008	124.991
200	112.995	122.991	112.984	122.997	112.966	122.991	112.970	122.998	113.009	124.984
210	112.989	122.980	112.970	122.984	112.954	122.983	112.965	122.992	113.007	124.977
220	112.979	122.971	112.958	122.975	112.946	122.979	112.962	122.986	112.991	124.975
230	112.969	122.964	112.950	122.971	112.944	122.980	112.966	122.983	112.983	124.975
240	112.965	122.960	112.947	122.973	112.952	122.985	112.964	122.987	112.990	124.979
250	112.965	122.962	112.954	122.983	112.963	122.991	112.971	122.995	113.004	124.987
260	112.971	122.972	112.970	122.996	112.975	123.000	112.981	123.006	113.018	124.993
270	112.985	122.990	112.990	123.013	112.989	123.016	112.996	123.022	113.030	124.998
280	113.007	123.010	113.013	123.029	113.004	123.031	113.014	123.030	113.035	125.000
290	113.029	123.030	113.030	123.042	113.020	123.044	113.025	123.036	113.036	125.002
300	113.049	123.045	113.043	123.051	113.032	123.052	113.031	123.040	113.037	125.004
310	113.062	123.052	113.050	123.059	113.039	123.056	113.032	123.041	113.041	125.008
320	113.067	123.052	113.052	123.057	113.041	123.053	113.031	123.042	113.042	125.011
330	113.057	123.040	113.043	123.045	113.032	123.043	113.024	123.037	113.045	125.014
340	113.045	123.026	113.024	123.029	113.017	123.029	113.020	123.032	113.041	125.014
350	113.024	123.006	113.002	123.011	112.994	123.012	113.012	123.024	113.038	125.010

Table 33. *Measured OOC amplitude (mm) for the cylinder with penetrations*

θ (deg)	E1	S1	S2	S3	S4[1]	S5[1]	S6	S7	S8[1]	S9	S10	S11	E2
0	-0.055	-0.097	-0.087	-0.055	-0.017	-0.025	-0.071	-0.101	-0.145	-0.142	-0.171	-0.181	-0.204
20	-0.004	0.017	0.015	0.015	0.034	0.039	-0.020	-0.050	-0.094	-0.116	-0.145	-0.181	-0.204
40	0.123	0.119	0.116	0.091	0.034	0.039	0.018	0.026	-0.018	-0.028	-0.069	-0.130	-0.153
60	0.224	0.119	0.129	0.135	0.110	0.077	0.069	0.064	0.059	0.049	0.007	-0.003	-0.026
80	0.199	0.119	0.129	0.135	0.123	0.102	0.095	0.077	0.084	0.099	0.058	0.124	0.152
100	0.148	0.119	0.129	0.123	0.097	0.077	0.069	0.102	0.109	0.150	0.185	0.213	0.228
120	0.021	0.055	0.040	0.047	0.034	0.064	0.069	0.102	0.109	0.176	0.210	0.200	0.228
140	-0.055	-0.047	-0.061	-0.042	-0.017	0.013	0.069	0.090	0.109	0.150	0.185	0.200	0.202
160	-0.207	-0.161	-0.125	-0.093	-0.068	-0.012	0.044	0.077	0.097	0.125	0.134	0.124	0.152
180	-0.233	-0.180	-0.138	-0.093	-0.055	-0.025	0.006	0.039	0.084	0.023	0.058	0.048	0.050
200	-0.182	-0.091	-0.087	-0.055	-0.042	-0.012	-0.007	0.001	0.071	-0.053	-0.006	-0.016	-0.026
220	-0.030	0.017	0.015	0.008	0.008	0.001	-0.007	-0.025	-0.043	-0.028	-0.044	-0.054	-0.052
240	0.123	0.119	0.091	0.047	0.034	0.013	0.018	-0.037	-0.068	-0.078	-0.056	-0.041	-0.039
260	0.199	0.119	0.116	0.059	0.034	0.001	-0.032	-0.050	-0.056	-0.053	-0.044	-0.028	-0.013
280	0.123	0.119	0.040	-0.004	-0.030	-0.050	-0.058	-0.050	-0.043	-0.028	-0.018	-0.016	-0.001
300	-0.080	-0.047	-0.061	-0.080	-0.093	-0.101	-0.083	-0.075	-0.043	-0.028	-0.044	-0.041	-0.052
320	-0.182	-0.135	-0.125	-0.131	-0.119	-0.114	-0.096	-0.088	-0.094	-0.078	-0.095	-0.079	-0.077
340	-0.131	-0.161	-0.138	-0.106	-0.068	-0.088	-0.083	-0.101	-0.119	-0.142	-0.145	-0.143	-0.166

1. The penetrations prevented measurements from being taken at certain locations (0° at S4 and S5, and 160° and 180° at S8). Eccentricity data for these points was linearly interpolated from the adjacent measurements.

Annex B: Measured Shell Thicknesses

Table 34. *Measured shell thickness in central bay (mm)*

ANGLE (degrees)	SPECIMEN						
	L300-No1	*L300-No2*	*L300-No3*	*L300-No4*	*L510-No1*	*L510-No2*	*L510-No3*
0	2.472	2.462	1.870	1.904	3.017	2.955	2.976
10	2.466	2.450	2.488	2.516	3.024	2.955	3.001
20	2.465	2.446	2.479	2.523	3.045	2.953	3.017
30	2.469	2.446	2.461	2.522	3.051	2.963	3.037
40	2.480	2.450	2.453	2.507	3.060	2.964	3.042
50	2.490	2.463	2.460	2.504	3.070	2.979	3.055
60	2.488	2.472	2.456	2.503	3.079	2.974	3.041
70	2.488	2.486	2.458	2.529	3.095	2.981	3.023
80	2.486	2.497	2.462	2.536	3.094	2.987	3.020
90	2.483	2.502	2.470	2.546	3.093	2.995	3.000
100	2.481	2.506	2.487	2.558	3.083	2.987	2.968
110	2.481	2.515	2.501	2.562	3.063	2.979	2.956
120	2.485	2.526	2.500	2.568	3.051	2.983	2.949
130	2.482	2.525	2.491	2.567	3.045	2.979	2.948
140	2.474	2.530	2.478	2.569	3.036	2.977	2.952
150	2.460	2.535	2.467	2.573	3.027	2.981	2.971
160	2.439	2.539	2.462	2.573	3.029	2.988	2.984
170	2.421	2.550	2.465	2.572	3.034	2.978	2.995
180	2.416	2.541	2.470	2.570	3.030	2.981	3.008
190	2.423	2.554	2.474	2.571	3.035	2.961	3.012
200	2.430	2.534	2.477	2.557	3.054	2.968	3.024
210	2.435	2.521	2.474	2.557	3.064	2.967	3.016
220	2.437	2.517	2.476	2.550	3.072	2.973	3.014
230	2.448	2.520	2.484	2.549	3.078	2.969	3.025
240	2.445	2.504	2.485	2.550	3.072	2.972	3.010
250	2.438	2.500	2.492	2.551	3.073	2.964	3.008
260	2.438	2.489	2.492	2.551	3.068	2.961	2.980
270	2.443	2.483	2.494	2.543	3.062	2.961	2.968
280	2.447	2.480	2.491	2.542	3.059	2.963	2.958
290	2.441	2.477	2.489	2.540	3.047	2.964	2.944
300	2.439	2.477	2.484	2.542	3.043	2.963	2.934
310	2.447	2.473	2.474	2.542	3.033	2.974	2.929
320	2.455	2.473	2.466	2.540	3.026	2.980	2.936
330	2.459	2.466	2.460	2.530	3.021	2.979	2.932
340	2.464	2.464	2.473	2.520	3.020	2.969	2.938
350	2.470	2.465	2.487	2.517	3.013	2.969	2.961

Annex C: Strain Data (L300-No3)
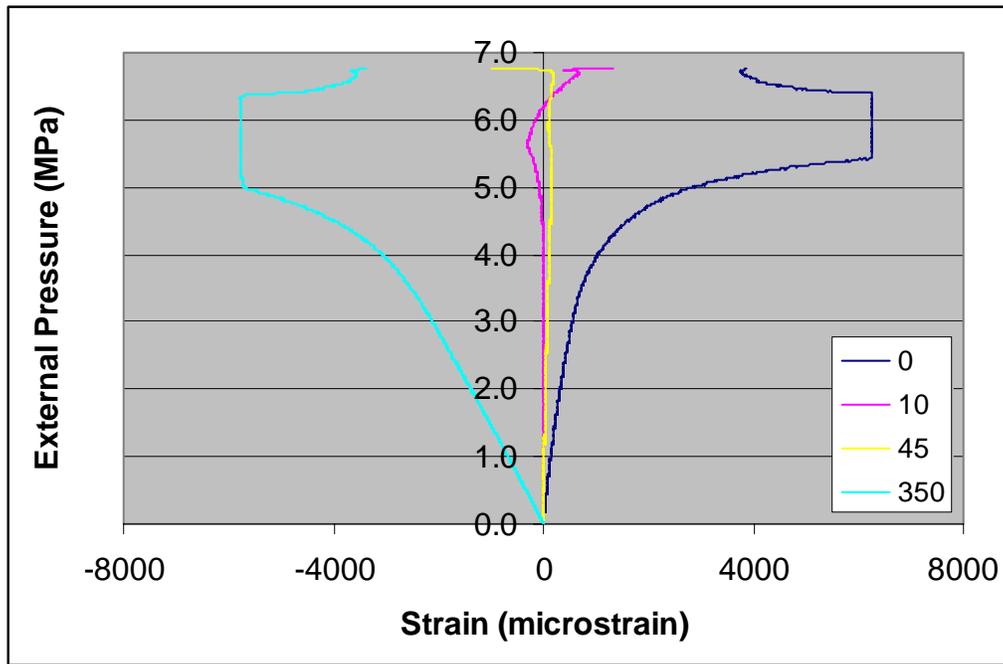
Figure 41. *L300-No3 – axial strain on inside of shell at central bay (mid-bay)*
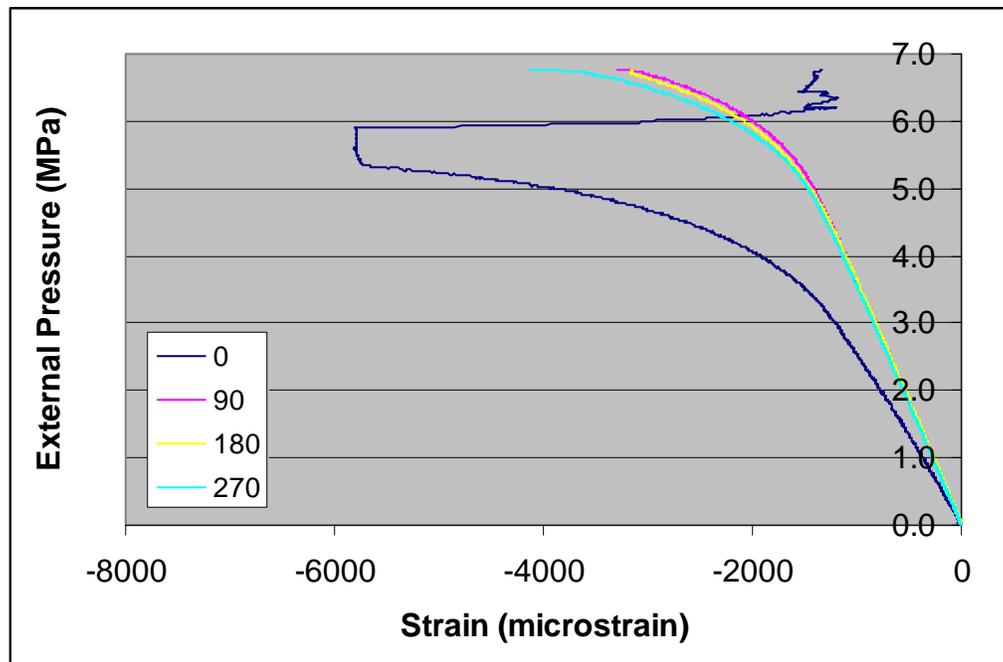
Figure 42. *L300-No3 – axial strain on outside of shell at central bay (mid-bay)*
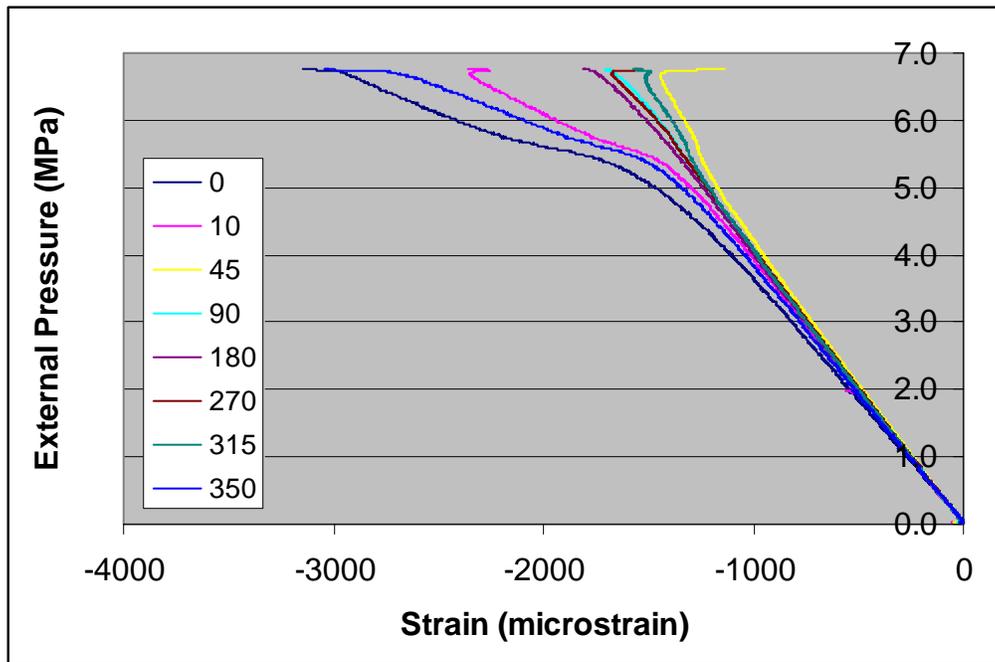
Figure 43. *L300-No3 – circumferential strain in the flange of frame #2*
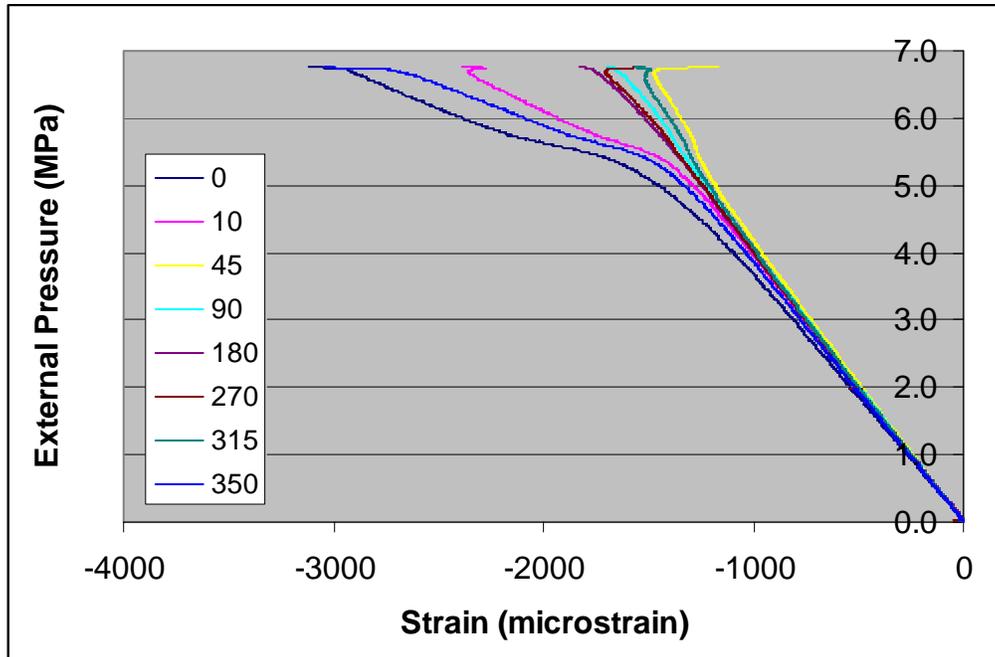
Figure 44. *L300-No3 – circumferential strain in the flange of frame #3*
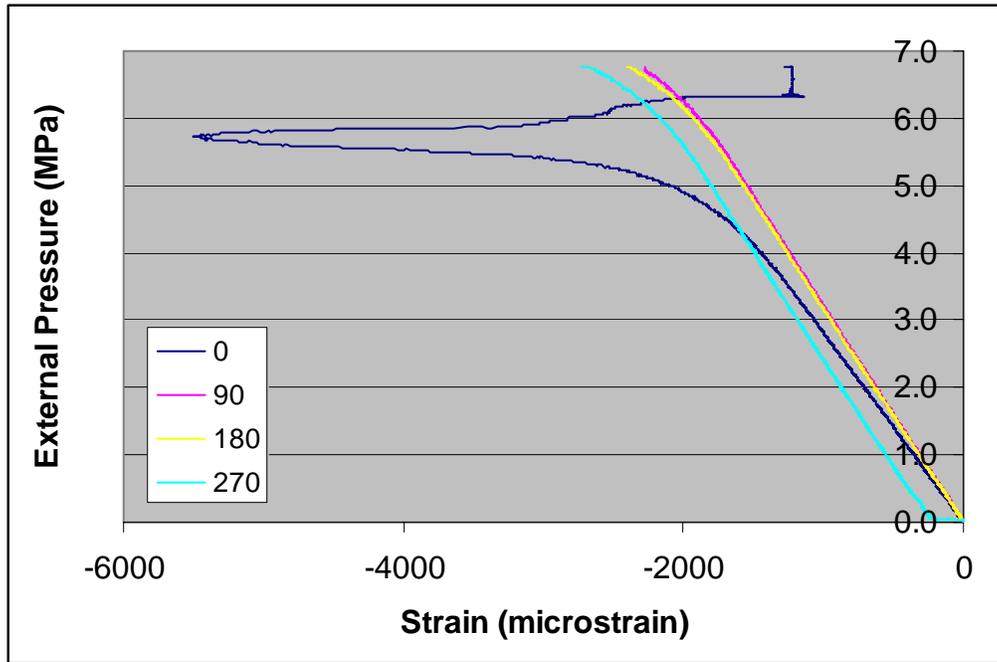
***Figure 45.*** *L300-No3 – circ. Strain on the outside of the shell adjacent to frame #2*
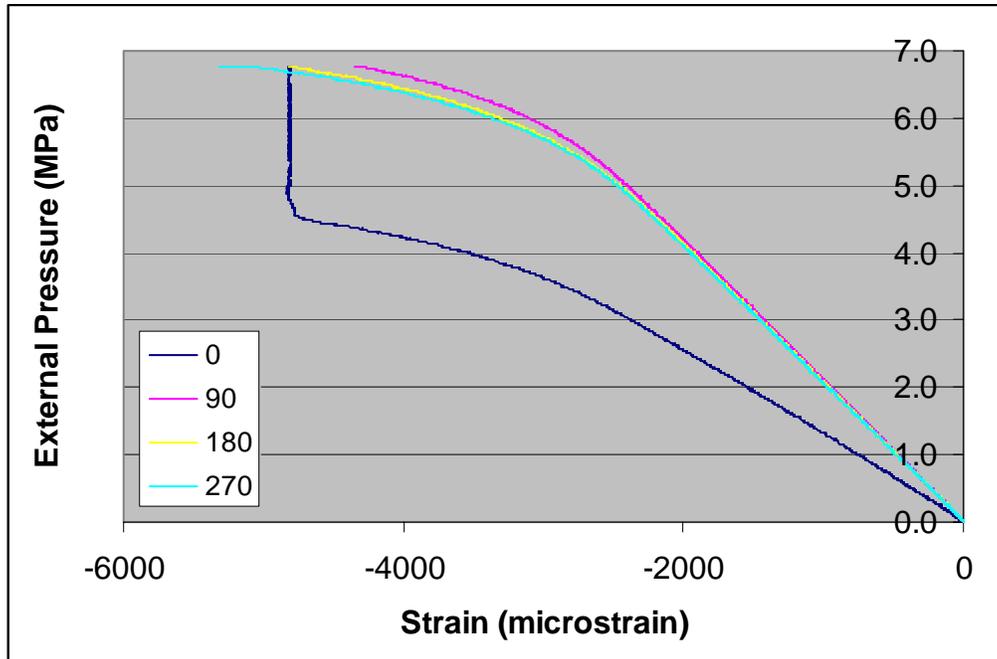
Figure 46. *L300-No3 – circ. Strain on the outside of the shell adjacent to frame #3*

Annex D: Strain Data (L510-No1A)
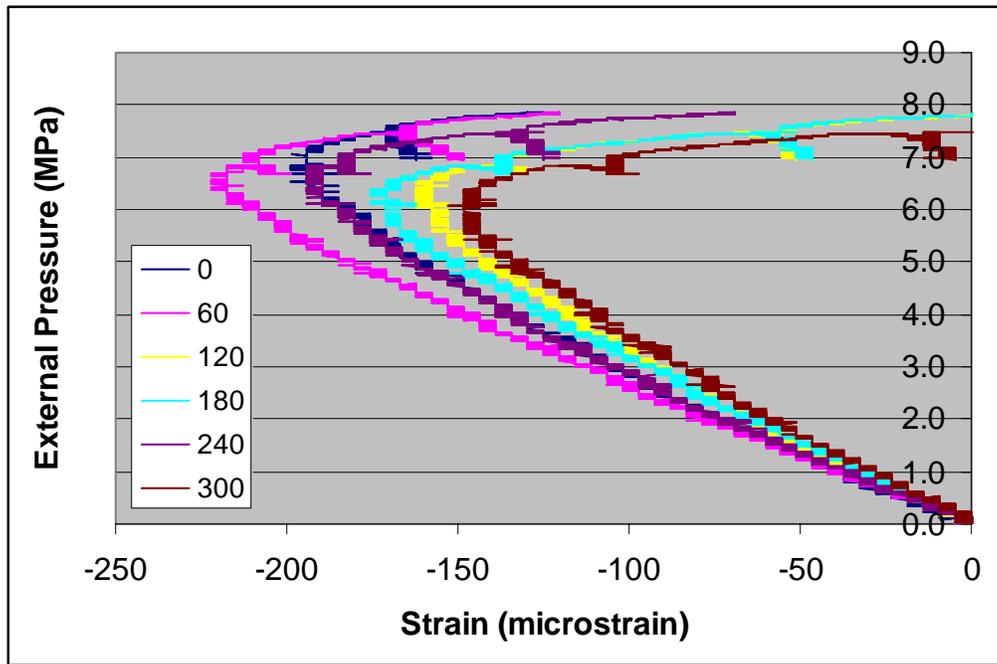
**Figure 47.** *L510-No1A – axial strain on inside of shell at central bay (mid-bay)*
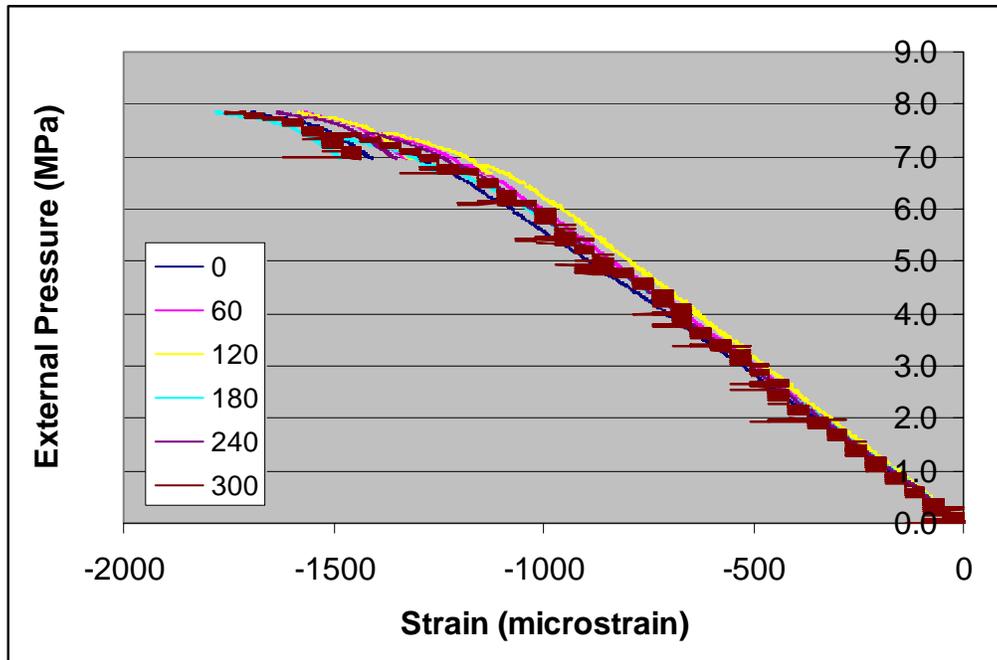
**Figure 48.** *L510-No1A – axial strain on outside of shell at central bay (mid-bay)*
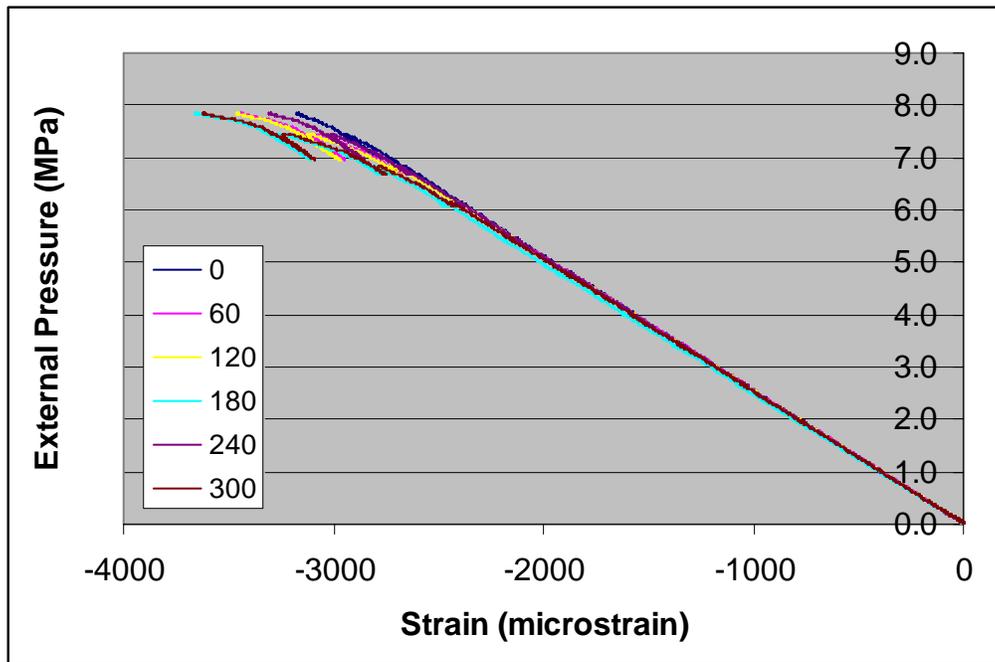
*Figure 49.* L510-No1A – circumferential strain inside shell at central bay (mid-bay)
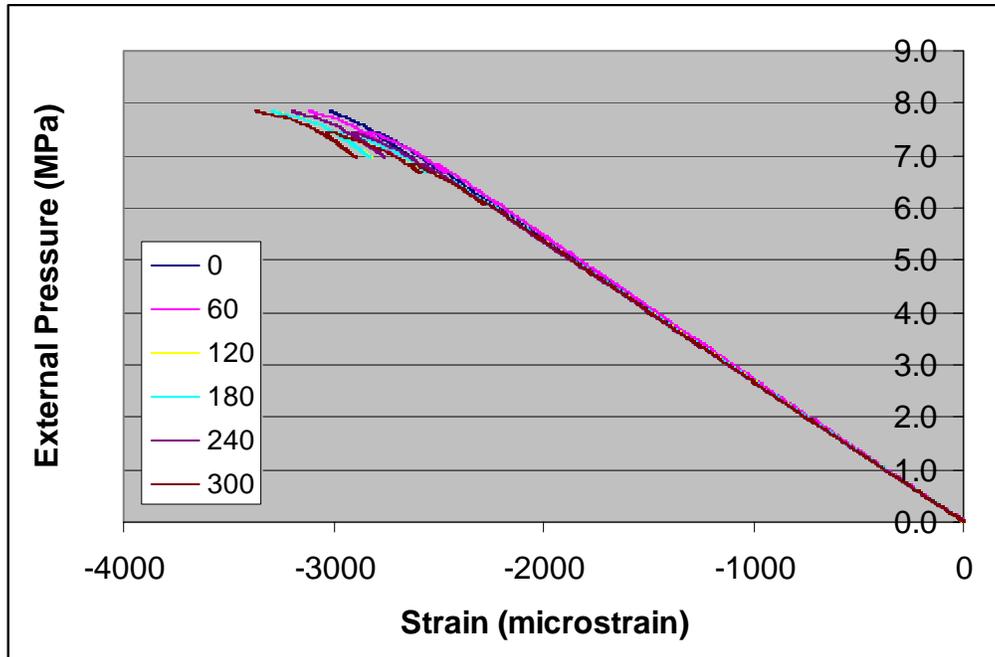
*Figure 50.* L510-No1A – circumferential strain outside shell at central bay (mid-bay)
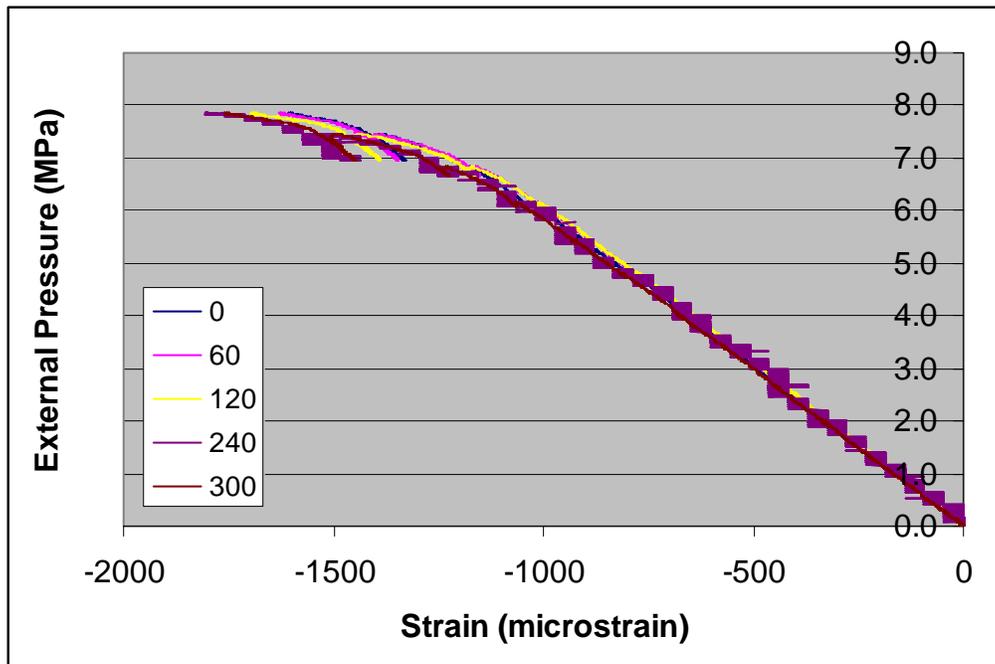
**Figure 51.** *L510-No1A – axial strain on outside of shell at end –bay (Fr#1-Fr#2)*
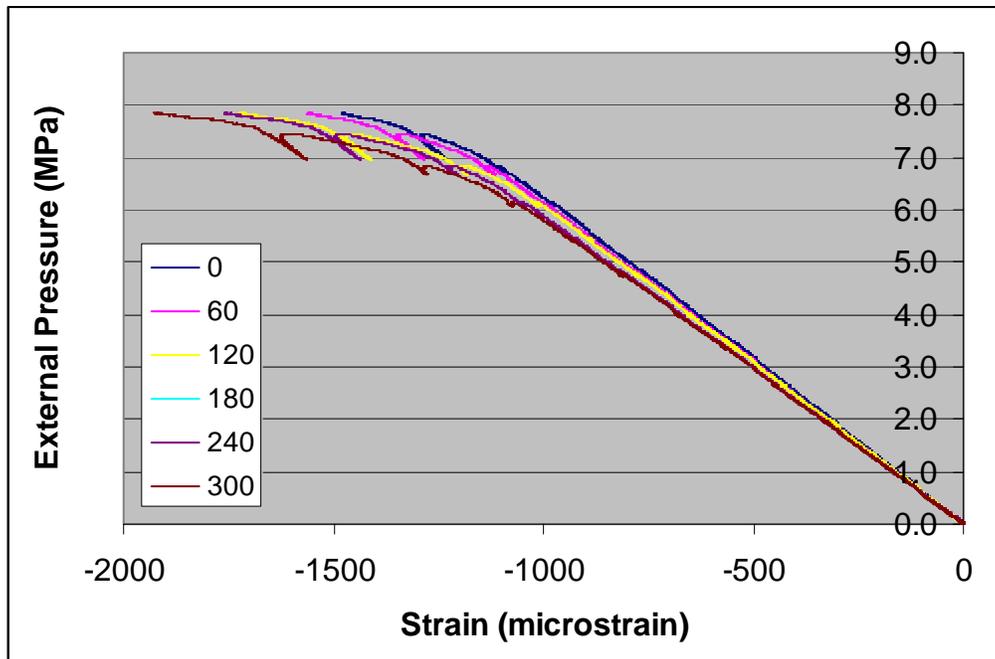
Figure 52. *L510-No1A – axial strain on outside of shell at end –bay (Fr#71-Fr#8)*
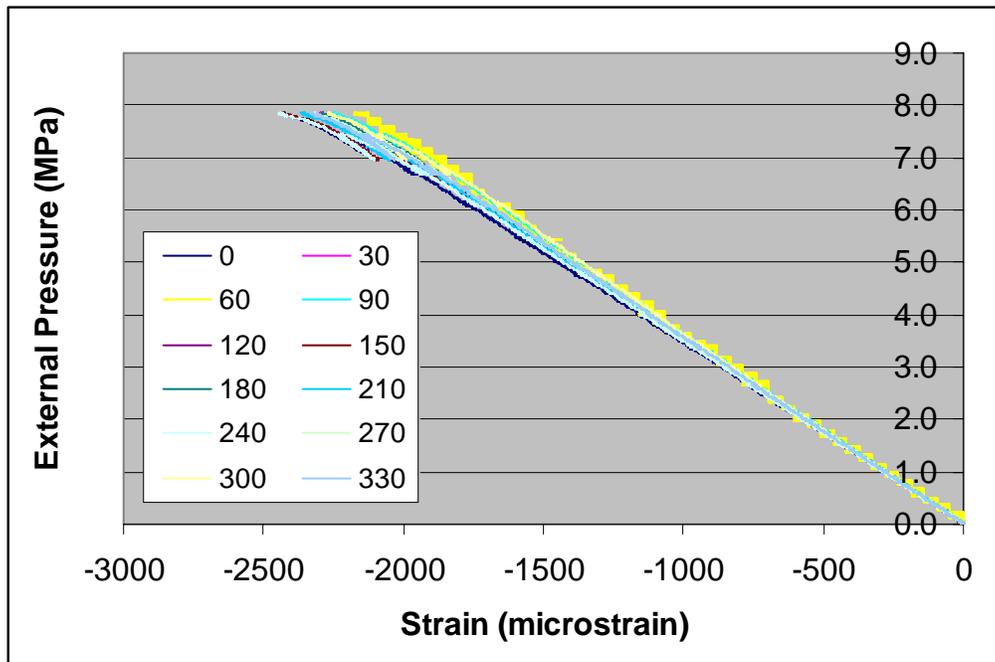
Figure 53. *L510-No1A – circumferential strain in the flange of frame #4*
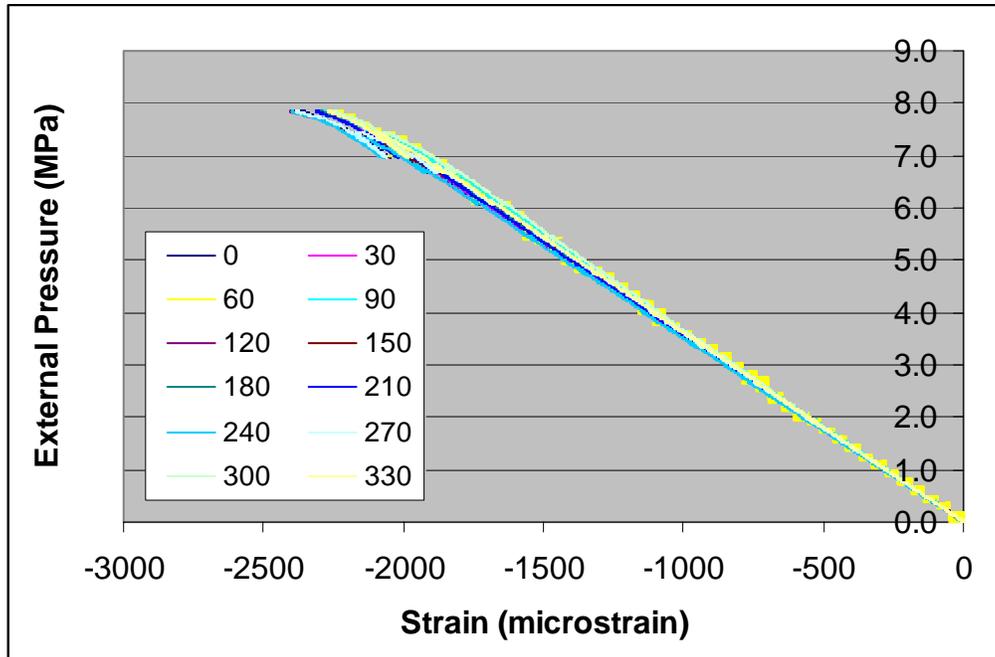
Figure 54. *L510-No1A – circumferential strain in the flange of frame #5*

Annex E: Strain Data (L510-No1B)
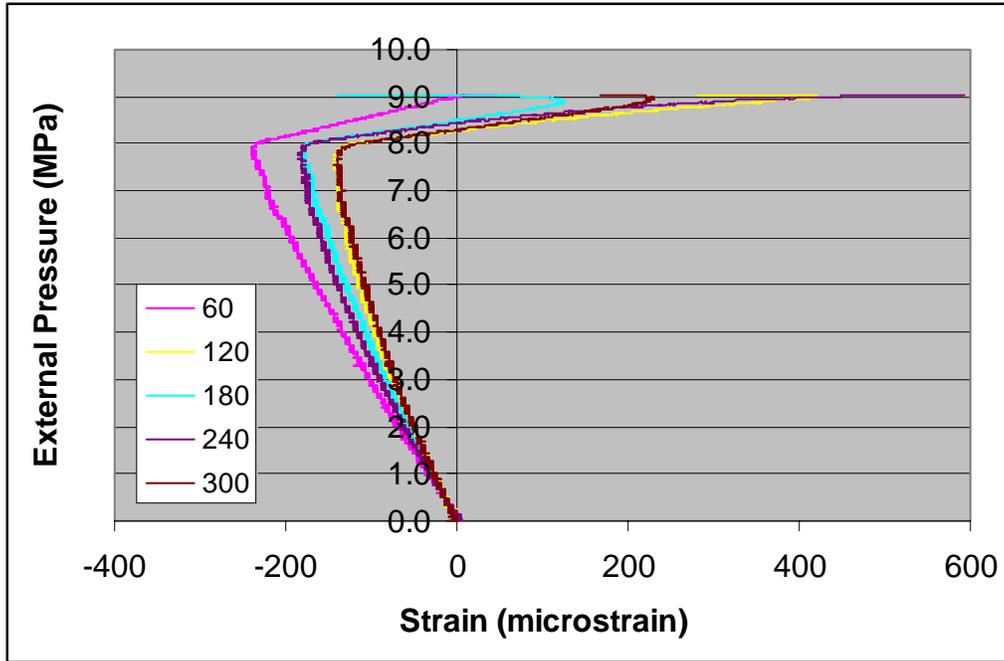
Figure 55. L510-No1B – axial strain on inside of shell at central bay (mid-bay)
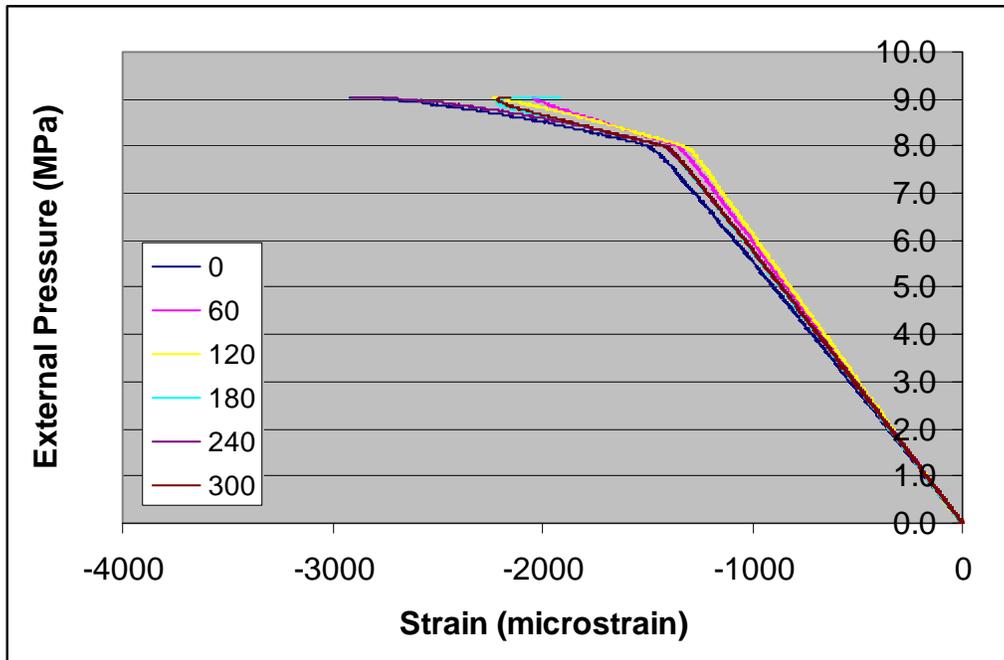
Figure 56. L510-No1B – axial strain on outside of shell at central bay (mid-bay)
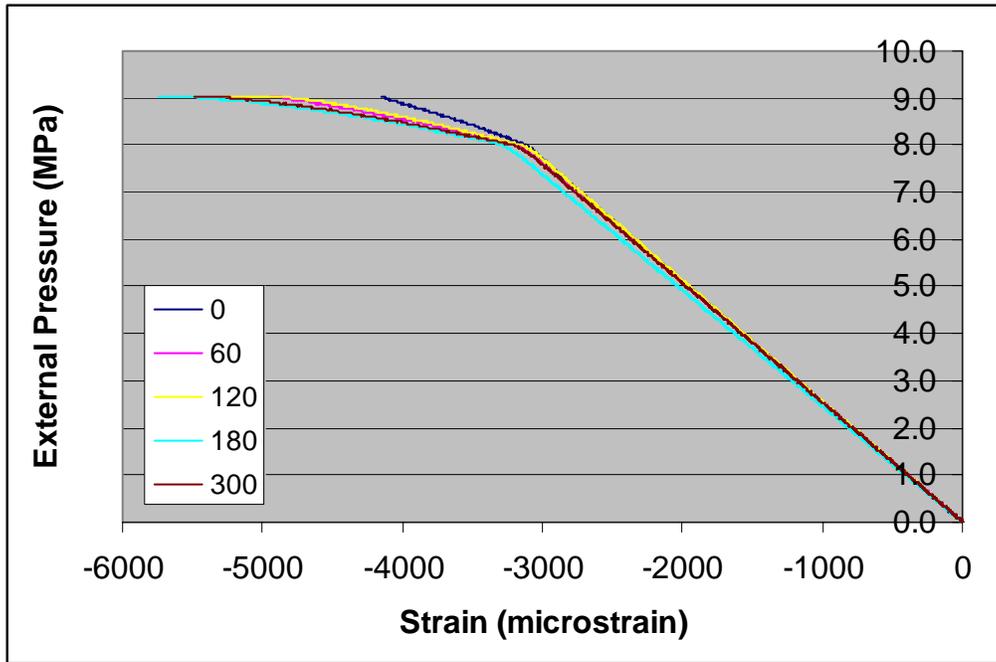
Figure 57. L510-No1B – circumferential strain on inside of shell at central bay (mid-bay)
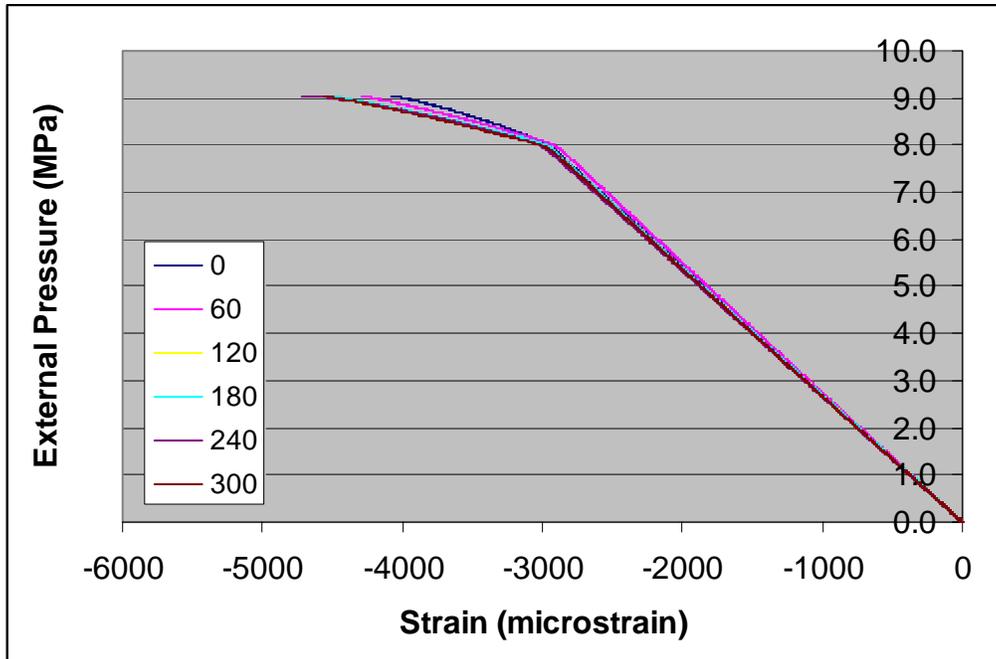
Figure 58. L510-No1B – circumferential strain on outside of shell at central bay (mid-bay)
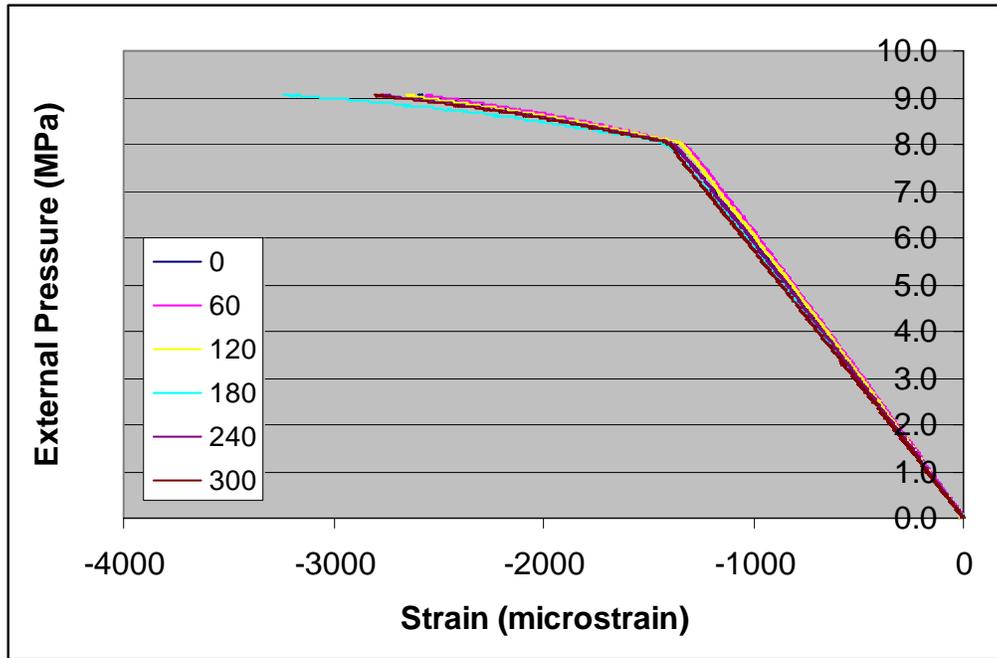
Figure 59. *L510-No1B – axial strain on outside of shell at end –bay (Fr#1-Fr#2)*
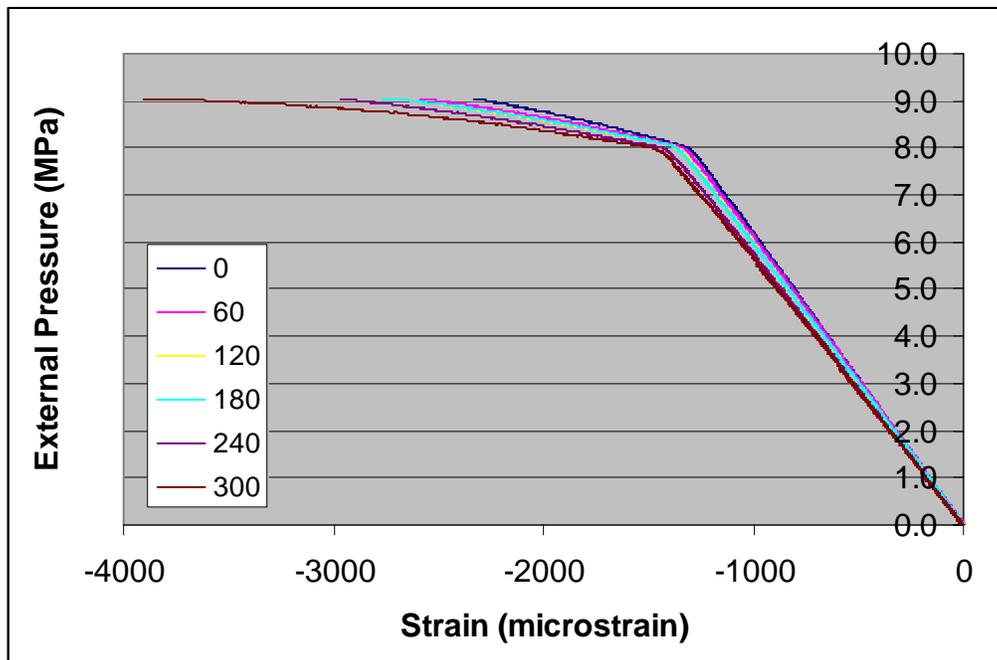
***Figure 60.*** *L510-No1B – axial strain on outside of shell at end –bay (Fr#71-Fr#8)*
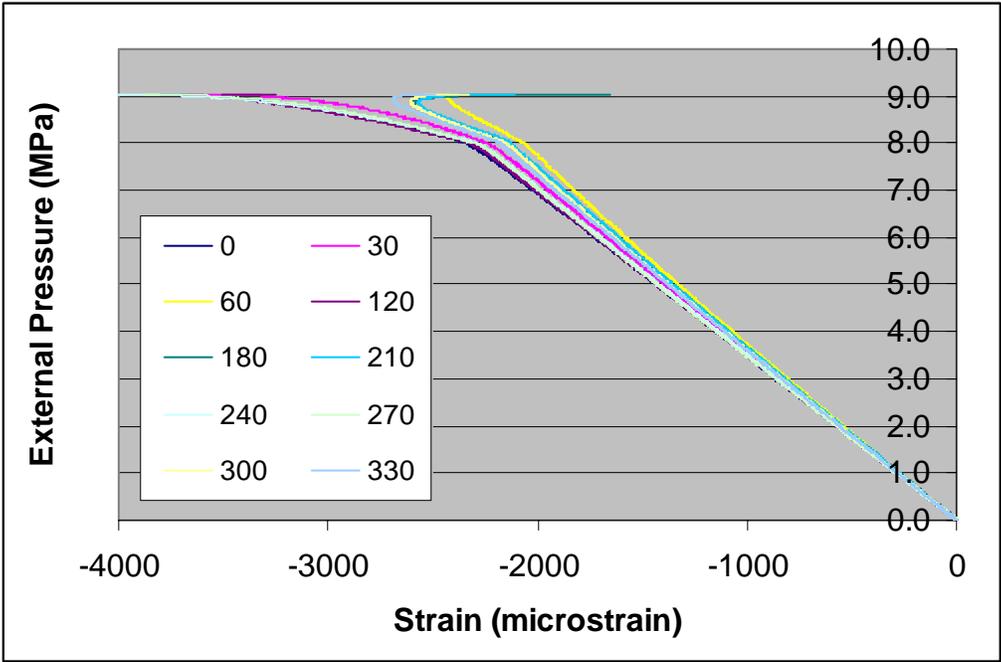
**Figure 61.** *L510-No1B – circumferential strain in the flange of frame #4*
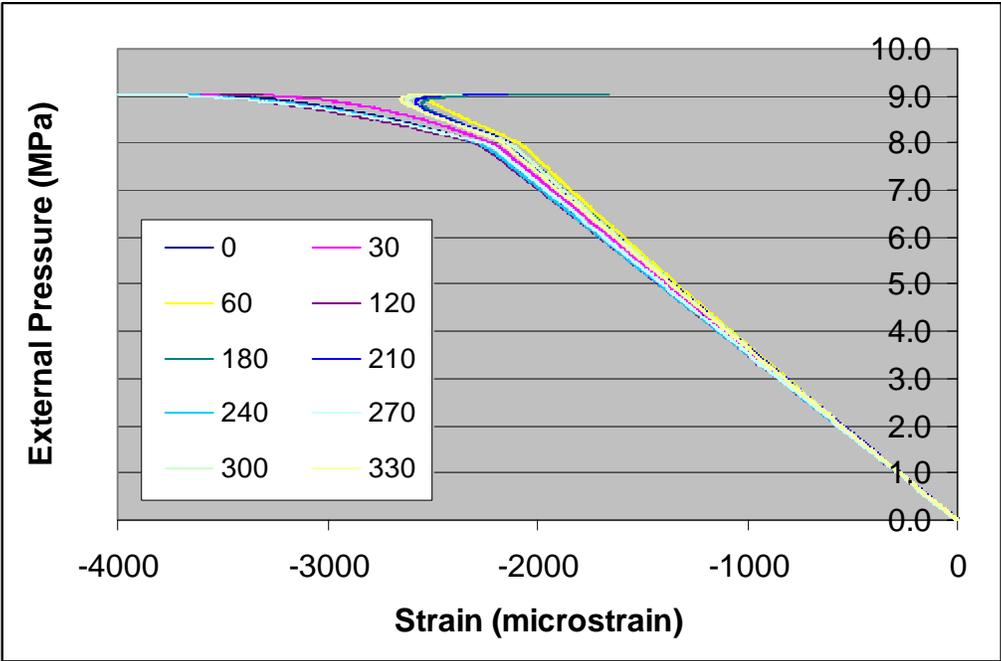
Figure 62. *L510-No1B – circumferential strain in the flange of frame #5*

# Annex F: Strain Data (Cylinder with Penetrations)
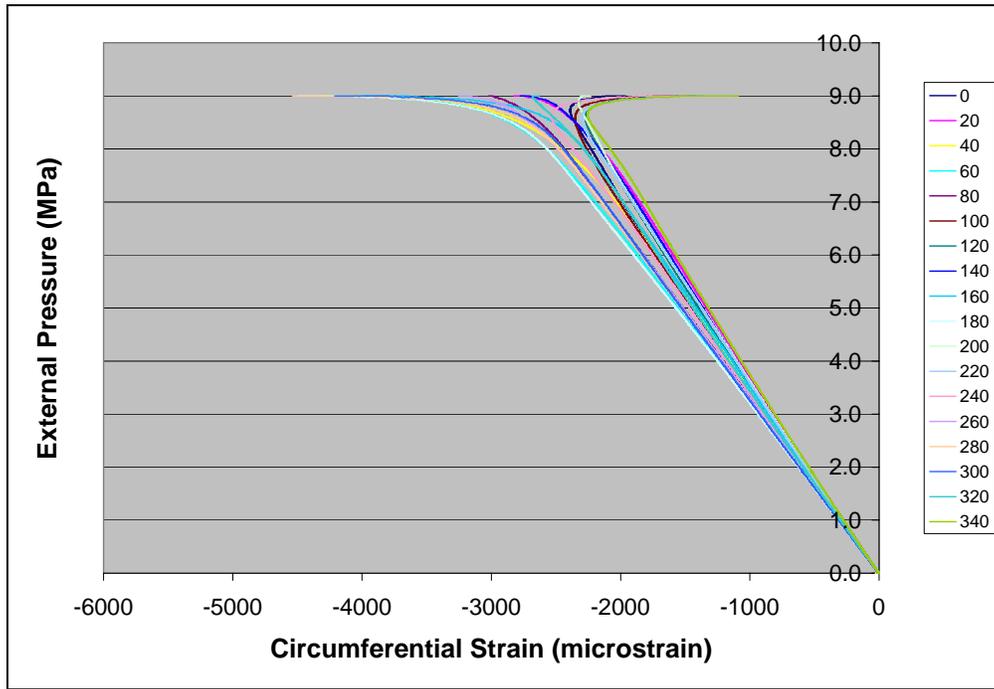
**Figure 63.** *Cylinder with penetrations – circumferential strain on central stiffener (S6)*
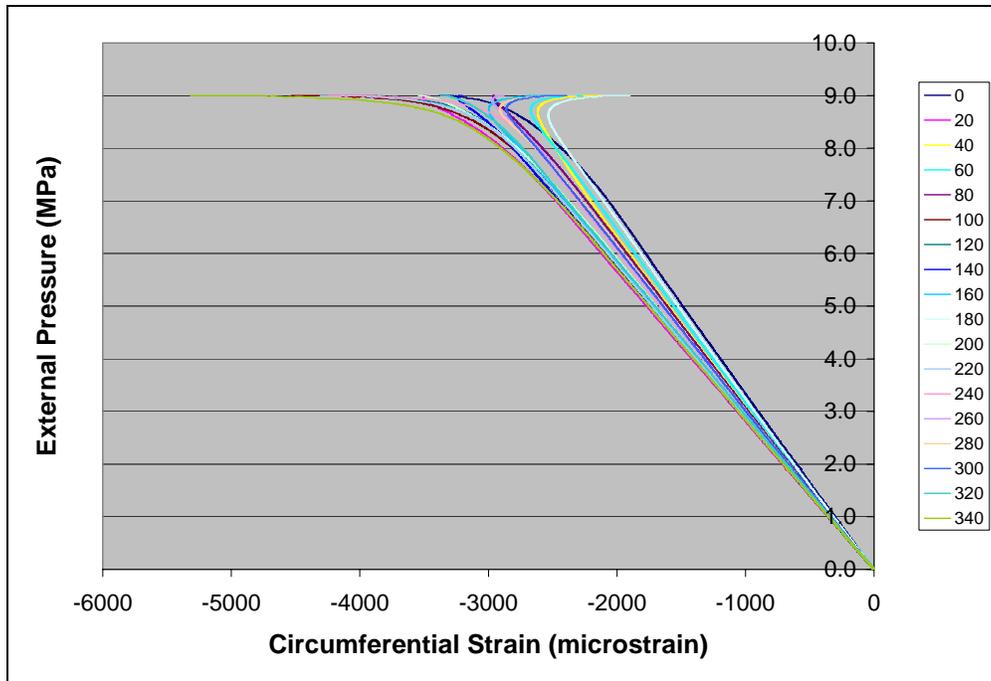
Figure 64. *Cylinder with penetrations – circ. Strain inside shell opposite stiffener S6*
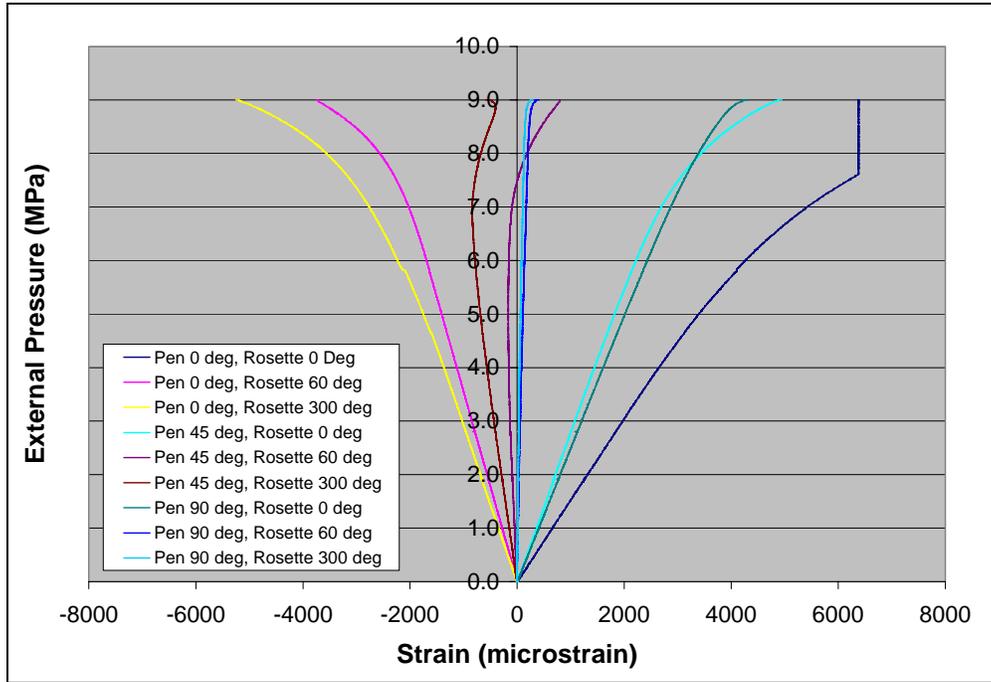
***Figure 65.*** *Cylinder with penetrations – rosette strains at penetration A*
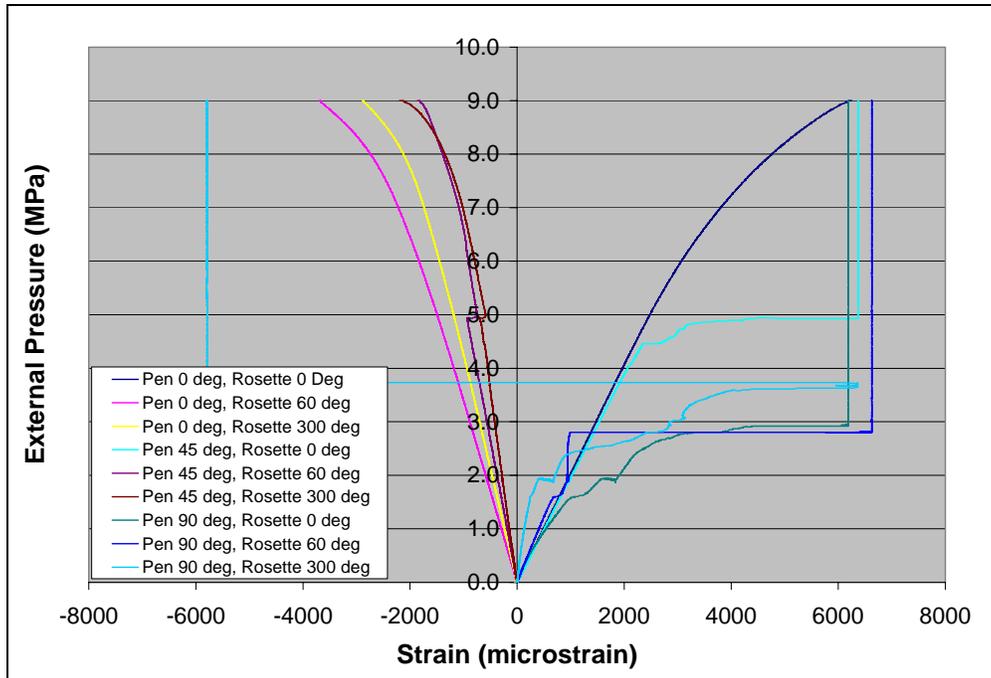
***Figure 66.*** *Cylinder with penetrations – rosette strains at penetration B*
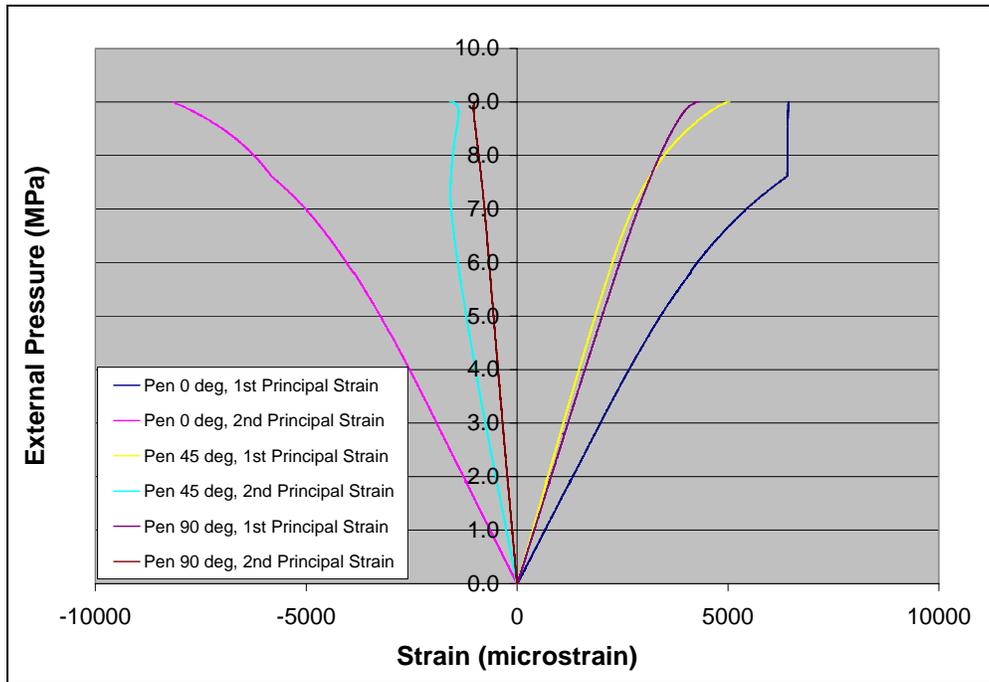
Figure 67. *Cylinder with penetrations – principal strains at penetration A*
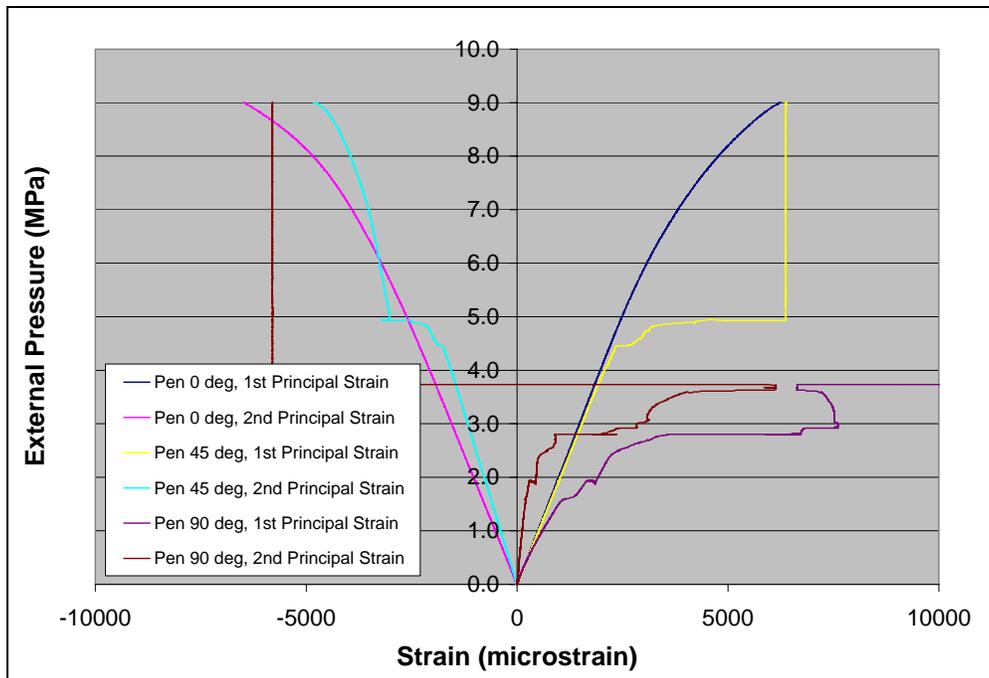

***Figure 68.*** *Cylinder with penetrations – principal strains at penetration B*
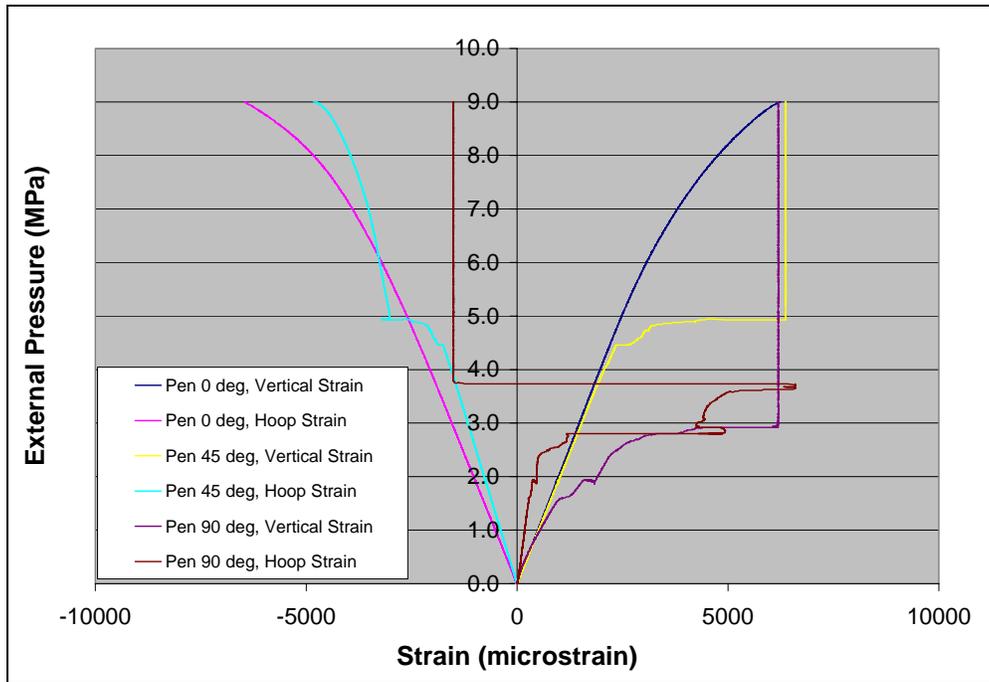
***Figure 69.*** *Cylinder with penetrations – orthogonal strains at penetration B*
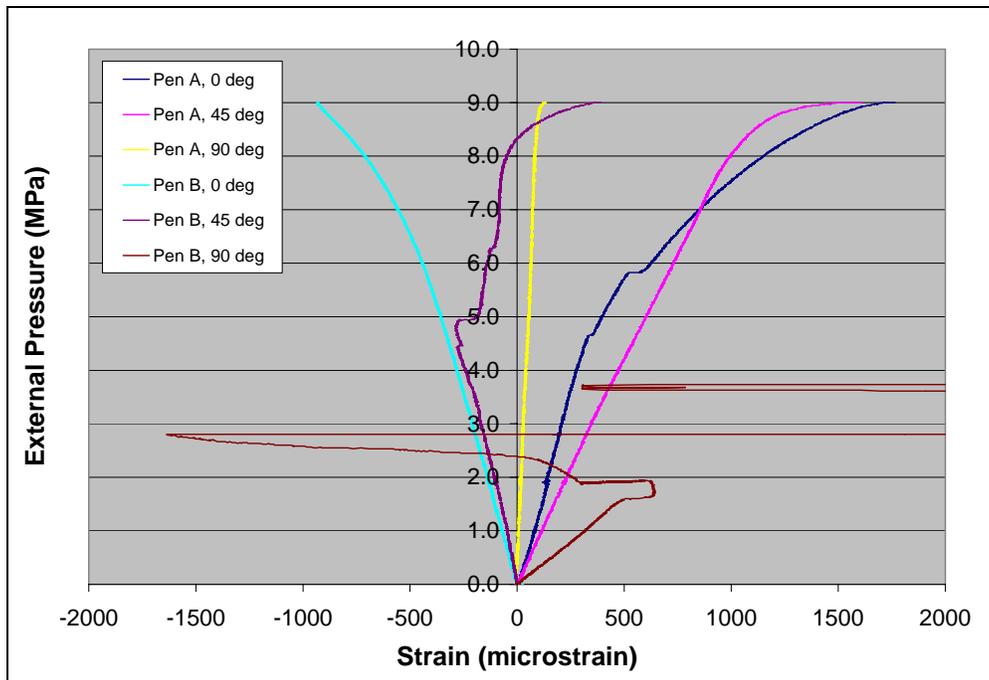
Figure 70. *Cylinder with penetrations – shear strains at penetrations*

List of Symbols, Acronyms and Initialisms

Symbols

a_1	offset of Fourier series data, associated with the sine term
b_1	offset of Fourier series data, associated with the cosine term
b_0	average radius from Fourier series analysis
A_n	Fourier amplitude for wave number, n
a_n	Fourier coefficient for wave number, n, associated with the sine term
b_n	Fourier coefficient for wave number, n, associated with the cosine term
E	Young's modulus
G	amplification gain for strain gauge data acquisition
i	Fourier mode index
k_g	strain gauge factor
n	buckling mode or out-of-circularity circumferential wave number
N	number of data points for Fourier series analysis
P	applied external pressure
P_c	collapse pressure of ring-stiffened cylinder
P_{c3}	external pressure at which the circumferential stress at the outside of the plating midway between frames, σ_3, equals yield
P_{c5}	external pressure at which the mean circumferential stress in the plating midway between frames, σ_5, equals yield
P_{c6}	external pressure at which the mean stress in the plating reaches the Von Mises yield criterion

P_{c7}	external pressure at which the longitudinal stress on the inside of the plating, adjacent to the frame, σ_7, equals yield
$P_{ci(lower)}$	interframe collapse pressure as determined from the BS5500 lower bound empirical curve
$P_{ci(mean)}$	interframe collapse pressure as determined from the SSP 74 mean empirical curve
P_{co}	external pressure causing overall elasto-plastic collapse of a ring-stiffened cylinder
P_{fy}	external pressure causing yield in the frame flange of an ideal circular ring-stiffened cylinder
P_{m1}	von Mises interframe elastic buckling pressure; iterated Kendrick solution
P_N	Bryant overall buckling pressure
P_P	external pressure causing overall collapse of a ring-stiffened cylinder, precipitated by shell yielding
$P_{y(n)}$	external pressure causing overall collapse of a ring-stiffened cylinder, precipitated by frame yielding
R_θ	radius at circumferential angle, θ
V_f	volume of pressure tank testing fluid
V_{in}	strain gauge input excitation voltage
V_{out}	strain gauge output voltage
V_t	volume of the pressure tank material
β	bulk modulus of the testing fluid
ε	strain
$\varepsilon_1, \varepsilon_2$	first and second principal strains, respectively
$\varepsilon_a, \varepsilon_b, \varepsilon_c$	rosette strains
ε_{axial}	strain in the axial (longitudinal) direction
ε_{circ}	strain in the circumferential (hoop) direction

γ	membrane shear strain
ν	Poison's ratio
θ	circumferential angle
σ_1, σ_2	first and second principal stresses, respectively
σ_{axial}	stress in the axial (longitudinal) direction
σ_{circ}	stress in the circumferential (hoop) direction
σ_{eqv}	von Mises equivalent stress (also called σ_6)
σ_3	circumferential stress at the outside of the plating midway between frames of a ring-stiffened cylinder
σ_5	mean circumferential stress in the plating midway between frames of a ring-stiffened cylinder
σ_6	von Mises equivalent stress (also called σ_{eqv})
σ_7	longitudinal stress on the inside of the plating, adjacent to the frame of a ring-stiffened cylinder

Acronyms and Initialisms

BS5500	British Standard Specification for Unfired Fusion Welded Pressure Vessels (Ref. [10])
DND	Department of National Defence
DRDC	Defence Research and Development Canada
Hz	Hertz, measure of frequency in cycles per second
OOC	out-of-circularity
min.	minute
MOU	memorandum of understanding
mm	millimetre
MPa	megapascal
SDF	submarine design formulae

SSP 74   Sea Systems Publication No. 74, Design of Submarine Structures (Ref. [4])

DOCUMENT CONTROL DATA

(Security classification of title, body of abstract and indexing annotation must be entered when the overall document is classified)

1. ORIGINATOR (the name and address of the organization preparing the document. Organizations for whom the document was prepared, e.g. Establishment sponsoring a contractor's report, or tasking agency, are entered in section 8.) Defence R&D Canada – Atlantic PO Box 1012 Dartmouth, NS, Canada B2Y 3Z7	2. SECURITY CLASSIFICATION (overall security classification of the document including special warning terms if applicable). UNCLASSIFIED

3. TITLE (the complete document title as indicated on the title page. Its classification should be indicated by the appropriate abbreviation (S,C,R or U) in parentheses after the title). Experimental investigation of the strength of damaged pressure hulls – Phase 1

4. AUTHORS (Last name, first name, middle initial. If military, show rank, e.g. Doe, Maj. John E.) MacKay, J. R.

5. DATE OF PUBLICATION (month and year of publication of document) February 2007	6a. NO. OF PAGES (total containing information Include Annexes, Appendices, etc). 90 (approx.)	6b. NO. OF REFS (total cited in document) 12

7. DESCRIPTIVE NOTES (the category of the document, e.g. technical report, technical note or memorandum. If appropriate, enter the type of report, e.g. interim, progress, summary, annual or final. Give the inclusive dates when a specific reporting period is covered). Technical Memorandum

8. SPONSORING ACTIVITY (the name of the department project office or laboratory sponsoring the research and development. Include address).

9a. PROJECT OR GRANT NO. (if appropriate, the applicable research and development project or grant number under which the document was written. Please specify whether project or grant). 11gp04	9b. CONTRACT NO. (if appropriate, the applicable number under which the document was written).

10a ORIGINATOR'S DOCUMENT NUMBER (the official document number by which the document is identified by the originating activity. This number must be unique to this document.) DRDC Atlantic TM 2006-304	10b OTHER DOCUMENT NOs. (Any other numbers which may be assigned this document either by the originator or by the sponsor.)

11. DOCUMENT AVAILABILITY (any limitations on further dissemination of the document, other than those imposed by security classification)

(X) Unlimited distribution
(   ) Defence departments and defence contractors; further distribution only as approved
(   ) Defence departments and Canadian defence contractors; further distribution only as approved
(   ) Government departments and agencies; further distribution only as approved
(   ) Defence departments; further distribution only as approved
(   ) Other (please specify):

12. DOCUMENT ANNOUNCEMENT (any limitation to the bibliographic announcement of this document. This will normally correspond to the Document Availability (11). However, where further distribution (beyond the audience specified in (11) is possible, a wider announcement audience may be selected).

13. ABSTRACT (a brief and factual summary of the document. It may also appear elsewhere in the body of the document itself. It is highly desirable that the abstract of classified documents be unclassified. Each paragraph of the abstract shall begin with an indication of the security classification of the information in the paragraph (unless the document itself is unclassified) represented as (S), (C), (R), or (U). It is not necessary to include here abstracts in both official languages unless the text is bilingual).

This document presents the results of Phase 1 of an experimental program to determine the collapse pressures of small-scale pressure hulls (ring-stiffened cylinders) with various amounts and patterns of simulated material loss due to corrosion. Six ring-stiffened aluminium cylinders have been tested as part of Phase 1: two undamaged specimens, three specimens with simulated localized corrosion, and one specimen with reinforced hull penetrations. Material loss was found to decrease the collapse pressure of each of the corroded specimens relative to similar undamaged cylinders. This loss of strength was attributed to reduced structural stiffness in the corroded regions, and was typically associated with an early onset of material yield. In two cases, yielding occurred at the corrosion well before the ultimate collapse load, and would thus further decrease the allowable working load. The results of the entire experimental program, which will include upwards of 40 cylinders, will be used to develop guidelines for corrosion tolerance, and to validate analytical and numerical methods.

14. KEYWORDS, DESCRIPTORS or IDENTIFIERS (technically meaningful terms or short phrases that characterize a document and could be helpful in cataloguing the document. They should be selected so that no security classification is required. Identifiers, such as equipment model designation, trade name, military project code name, geographic location may also be included. If possible keywords should be selected from a published thesaurus. e.g. Thesaurus of Engineering and Scientific Terms (TEST) and that thesaurus-identified. If it not possible to select indexing terms which are Unclassified, the classification of each should be indicated as with the title).

pressure hull
ring-stiffened cylinder
submarine
collapse pressure
corrosion
structural analysis

This page intentionally left blank.

Defence R&D Canada

Canada's leader in defence
and National Security
Science and Technology

R & D pour la défense Canada

Chef de file au Canada en matière
de science et de technologie pour
la défense et la sécurité nationale

DEFENCE R&D DÉFENSE